The Role of Piccolo in Cerebellar Network Organisation and the Aetiology of Pontocerebellar Hypoplasia Type 3

Inaugural-Dissertation

to obtain the academic degree

Doctor rerum naturalium (Dr. rer. nat.)

submitted to the Department of Biology, Chemistry and Pharmacy

of Freie Universität Berlin

by

JOANNE ELIZABETH FALCK

from Derby, United Kingdom

2020

The work was conducted from May 2016 to February 2020 under the supervision of Professor Dr. Craig C. Garner at the German Centre for Neurodegenerative Diseases (DZNE) in the Helmholtz Association.

I hereby confirm that I have written the thesis independently using only the literature and aids mentioned and without illicit assistance from third parties.

1st Reviewer:

Prof. Dr. Craig C. Garner

2nd Reviewer:

Prof. Dr. Peter Robin Hiesinger

Thesis defence on: 17.06.2020

Table of Contents

1. Summary

Piccolo, a presynaptic active zone protein, is known for its role in the regulated assembly and function of vertebrate synapses. Genetic studies suggest a link to several psychiatric disorders as well as Pontocerebellar Hypoplasia Type 3 (PCH3). A Piccolo knockout rat model was recently generated by means of transposon mutagenesis (*Pclo*$^{gt/gt}$) [116]. During my doctoral studies, I sought to characterise this rat model. In doing so, I took an exploratory approach by beginning to examine overall changes in brain anatomy, narrowing the focus to the level of the network, synapse and the ultrastructure of the presynaptic terminal in the hope of elucidating some of the mechanisms involved in PCH3.

I found that the loss of Piccolo leads to a dramatic reduction in brain size compared to wildtype (*Pclo*$^{wt/wt}$) animals, attributed to a decrease in the size of the cerebral cortical, cerebellar and pontine regions. Moreover, the maturation of mossy fibre (MF) afferents, expression of the α6 $GABA_A$ receptor subunit at mossy fibre-granule cell synapses and the innervation of Purkinje cells by cerebellar climbing fibres are all perturbed in *Pclo*$^{gt/gt}$ cerebella. Ultrastructural and functional studies revealed a reduced size and complexity of MF boutons, with fewer synaptic vesicles and changes in synaptic transmission. These data imply that Piccolo is required for the normal development, maturation and function of neuronal networks formed between the brainstem and cerebellum. Consistently, behavioural studies demonstrated that adult *Pclo*$^{gt/gt}$ rats display impaired motor coordination, despite adequate performance in tasks that reflect muscle strength and locomotion. Together these data suggest that loss of Piccolo function in patients with PCH3 could be involved in many of the observed anatomical and behavioural symptoms, and that the further analysis of these animals could provide fundamental mechanistic insights into this devastating disorder.

2. Zusammenfassung

Piccolo, ein Protein der präsynaptischen aktiven Zone, ist bekannt für seine Rolle im regulierten Aufbau und in der Funktion von Wirbeltier-Synapsen. Genetische Studien deuten auf eine Verbindung zu verschiedenen psychiatrischen Störungen, sowie zur Pontocerebellären Hypoplasie Typ 3 (PCH3) hin. Ein Piccolo-Knockout-Rattenmodell wurde vor Kurzem mittels Transposon-Mutagenese ($Pclo^{gt/gt}$) generiert [116]. Während meiner Doktorarbeit habe ich versucht, dieses Rattenmodell zu charakterisieren. Dabei verfolgte ich einen explorativen Ansatz, indem ich begann, die allgemeinen Veränderungen in der Anatomie des Gehirns zu untersuchen. Hierbei legte ich den Schwerpunkt auf die Ebene des Netzwerks, der Synapse und der Ultrastruktur des präsynaptischen Nervenendes, in der Hoffnung, einige der an PCH3 beteiligten Mechanismen aufzuklären.

Fand ich heraus, dass der Verlust von Piccolo zu einer dramatischen Verringerung der Hirngröße im Vergleich zu Wildtyp-Tieren ($Pclo^{wt/wt}$) führt, was auf eine Abnahme der Größe der Hirnrinde, des Kleinhirns und des Pons zurückzuführen ist. Darüber hinaus sind die Reifung der Moosfaser-Afferenzen, die Expression der α6 $GABA_A$-Rezeptor-Untereinheit an den Synapsen zwischen Moosfasern und Körnerzellen und die Innervation der Purkinjezellen durch cerebellare Kletterfasern in $Pclo^{gt/gt}$ Cerebella gestört. Ultrastrukturelle und funktionelle Studien ergaben eine reduzierte Größe und Komplexität der Moosfaser-Synapsen, mit weniger synaptischen Vesikeln und Veränderungen in der synaptischen Übertragung. Diese Daten implizieren, dass Piccolo für die normale Entwicklung, Reifung und Funktion der neuronalen Netzwerke, die zwischen Hirnstamm und Kleinhirn gebildet werden, erforderlich ist. Übereinstimmend haben Verhaltensstudien gezeigt, dass erwachsene $Pclo^{gt/gt}$ Ratten, trotz adäquater Leistung bei Aufgaben, die Muskelkraft und Fortbewegung widerspiegeln, eine beeinträchtigte motorische Koordination aufweisen. Zusammenfassend deuten diese Ergebnisse darauf hin, dass der Verlust der Funktion von Piccolo bei Patienten mit PCH3 an vielen der beobachteten anatomischen und verhaltensbezogenen Symptome beteiligt sein könnte und dass die weitere Analyse dieser Tiere grundlegende mechanistische Erkenntnisse über diese verheerende Erkrankung liefern könnte.

3. Introduction

A mutation in the presynaptic scaffolding protein Piccolo has been implicated in the disease pathology of Pontocerebellar Hypoplasia Type 3 [5]. Little is known about the aetiology of this rare but devastating developmental disorder; however, the recent generation of a Piccolo knockout rat [116] has allowed us to speculate the role of Piccolo in this disease and to consider additional roles for this presynaptic protein in the development of the cerebellum and in the organisation of cerebellar microcircuitry.

3.1 Pontocerebellar Hypoplasia

The term Pontocerebellar Hypoplasia (PCH) was coined over a century ago referring to a patient who displayed a dwarfed growth of the cerebellum and developmental abnormalities [127]. Since then, this heterogeneous group of disorders has been classified into 12 distinct types [8, 176]. Though PCH patients share a similar pathology - namely hypoplasia or atrophy of the pons, cerebellum and supratentorial structures manifesting in motor and cognitive impairments [147, 176] - the genetic origin of these diseases varies from those responsible for neuronal migration to mitochondrial fission/fusion and RNA processing [176]. Identification of genes and mechanisms involved in the aetiology of PCH is crucial to further our understanding of this disease and to develop therapeutic avenues.

Thanks to next-generation sequencing techniques, classification of PCH into further types and subtypes has increased and researchers have been able to distinguish the vastly different genetic mechanisms which manifest as clinically similar phenotypes in patients; which is fundamental to finding a treatment for these devastating disorders. A table of clinical symptoms and the identified genetic mutations can be observed in Table 1.

PCH subtype	Clinical symptoms/distinguishing features	Gene(s)	Gene function
PCH1	SMA-like, degeneration of motor neurones, muscle weakness, hypertonia, respiratory insufficiency, congenital contractures	1A: *VRK1* 1B: *EXOSC3* 1C: *EXOSC8* 1D: *SLC25A46*	Golgi assembly, neuronal migration RNA processing and degradation RNA processing and degradation Mitochondrial fission and fusion
PCH2	Generalised clonus, impaired swallowing, dystonia, chorea, spasticity, progressive microcephaly	2A: *TSEN54* 2B: *TSEN2* 2C: *TSEN34* 2D: *SEPSECS*	tRNA splicing tRNA splicing tRNA splicing Selenocysteine

		2E: *VPS53* 2F: *TSEN15*	synthesis, tRNA formation Vesicle trafficking in late Golgi tRNA splicing
PCH3	Dysmorphic facial features, optic atrophy, thin corpus callosum, cerebellar atrophy, seizures	*PCLO*	Synapse formation, SV regulation and cycling
PCH4	Severe form of PCH2A, with congenital contractures, polyhydramnios, primary hypoventilation, severe generalised clonus and neonatal death	*TSEN54*	tRNA splicing
PCH5	Identical to PHC4	*TSEN54*	tRNA splicing
PCH6	Variable hyperlactatemia, seizures, hypertonia, respiratory chain dysfunction, progressive supratentorial atrophy	*RARS2*	Mitochondrial arginyl-tRNA synthetase
PCH7	DSD, thin corpus callosum, enlarged ventricles, diminished white matter	*TOE1*	RNA processing, cell growth
PCH8	Abnormal muscle tone dystonia, ataxia, non-progressive, non-degenerative	*CHMP1A*	Protein sorting into lysosomes, degradation
PCH9	Abnormal muscle tone, dysmorphic facial features, impaired swallowing, “figure 8” configuration of brainstem, corpus callosum agenesis	*AMPD2*	Converting AMP to IMP, energy metabolism
PCH10	Abnormal muscle tone, seizures, mild cerebellar hypoplasia/atrophy, motor neurone degeneration,	*CLP1*	Multifunctional kinase, tRNA splicing
PCH11	Non-progressive, non-degenerative, dysmorphic facial features	*TBC1D23*	Intracellular vesicle transport
PCH12	Severe prenatal symptoms, micrognathia, arthrogryposis	*COASY*	Synthetic and degradative pathways

Table 1: Classification of PCH Types
Table summarising the main clinical features and associated genes for PCH types. SMA = spinal muscular dystrophy; SV = synaptic vesicle; DSD = disorder of sexual development; AMP = adenosine monophosphate; IMP = inosine monophosphate. Adapted from Appelhof [8] and van Dijk et al. [176].

3.1.1 Pontocerebellar Hypoplasia Type 3

Whilst there are many PCH types yet to elucidate, the focus of this thesis will be on the enigma of PCH3 and the link between its pathology and the Piccolo protein. In more detail, patients with PCH3 (also known as Cerebellar Atrophy with Progressive Microcephaly (CLAM)) suffer from the aforementioned motor and cognitive impairments as well as absence seizures (brief lapses in consciousness), hypertonia (high level of muscle tone or tension), hyperreflexia (oversensitive or overactive reflexes) and optic atrophy (degeneration of the optic nerve). Anatomically, PCH3 manifests in progressive microcephaly (undersized head), brachycephaly (shorter skull), craniofacial dimorphisms and short stature [127, 137, 147]. As demonstrated by MRI studies, the brains of PCH3 patients display hypoplasia of the pons and cerebellum, as well as supratentorial white matter loss and thinning of the corpus callosum, as can be observed in Figure 1B, summarised in Table 1 [5, 8].

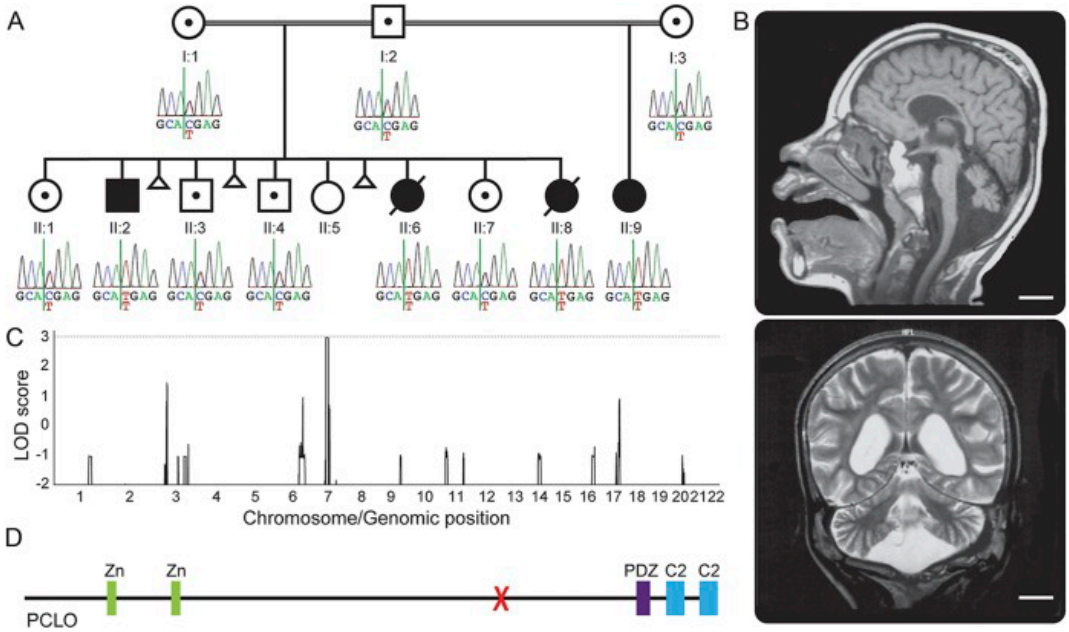

Figure 1: Pontocerebellar Hypoplasia Type 3 is associated with a mutation in the *PCLO* gene
A) Hereditary tree of a family carrying a PCH3 mutation. Those homozygous for the C to T change are affected. B) (top panel) Sagittal T1 weighted MRI scan image of a PCH3 patient aged 11 years. Note the loss in cerebellar and pontine volume and thin corpus callosum; (bottom panel) coronal T2-weighted MRI scan image reveals loss of cerebral white matter and cerebellar hemisphere volume. Scale bars = 2 cm. C) Genome-wide linkage analysis reveals a common SNP located on chromasome 7. D) Schematic of *PCLO* gene with the site of the mutation indicated by a red cross. Zn = zinc finger domain, PDZ = PDZ domain, C2 = C2 domain. Adapted from Ahmed et al. [5].

Previous studies mapped the PCH3 phenotype to chromosome 7q11-21 [137]. However, more recently, a single nucleotide polymorphism (SNP) in the human *PCLO* gene - indeed, located on chromosome 7 at position 21.11 - has been found in patients with PCH3, which is predicted to eliminate the PDZ and C2 domains of the C-terminus of the protein (Figure 1 C) [5] and perhaps destabilise the protein. This observation has led to the hypothesis that loss of function (LOF) of the

encoded protein Piccolo is critically responsible for the phenotypes seen in this neurodevelopmental/neurodegenerative disorder. At present, two children from the Sultanate of Oman have been discovered harbouring the *PCLO* mutation (Figure 1A), a homozygous C to T change [5].

The identification of genetic mutations in patients with PCH3 has huge implications for this field. However, many questions still remain unanswered. Is the loss of functional Piccolo a causal factor for the changes in brain and behaviour observed in patients with PHC3? How might the networks of synapses within the cerebellum and pons be affected in individuals with PCH3? And how could Piccolo and its interaction partners play a role in the development of the affected brain regions?

As discussed, the most severely affected brain regions in PCH3 are the cerebellum and the pons, connected via the pontocerebellar tract. A deeper understanding of PCH3 can be gleaned when the anatomy, cell populations and synaptic networks of the cerebellum and the pons are considered.

3.2 The cerebellum: cell types and microcircuitry

The cerebellum is primarily responsible for the coordination and fine-tuning of movement, integrating commands from the cerebral cortex as well as sensory information from the periphery [35, 112]. The cerebellum also plays a role in higher brain functions such as emotional and cognitive processing [155, 166] and has been associated with a range of psychiatric conditions such as Schizophrenia, major depressive disorder and bipolar disorder [100]. There are nine main cell types within the cerebellum: Purkinje, granule, Golgi, basket, stellate, unipolar brush, lugaro, candelabrum cells and Bergmann glia.

3.2.1 Cerebellar cell types

As the only efferent cells of the cerebellum, Purkinje cells (PCs) send myelinated GABAergic fibres to inhibit cells of the deep cerebellar nuclei. Their large somas constitute the Purkinje cell layer (PCL) and their striking tree-like spiny dendritic arbours fill the molecular layer (ML) (Figures 2A and 3), receiving excitatory signals from the inferior olive in the form of climbing fibres (CFs) (Figures 3 and 5A-C) and parallel fibres (PFs) (Figures 2B and D, 3, 5A-C) arising from granule cells (GCs) (Figures 2C and 3). Basket and stellate interneurones (Figures 2F-G and 3) are situated in the ML, inhibiting PCs and therefore spatially refining excitatory signals deriving from GCs [17]. The size and complexity of their dendritic tree allows for PCs to receive up to 170,000 PF inputs [85] from millions of GCs, whilst they project relatively few axons to the deep cerebellar nuclei, allowing for massive computational power of the cerebellum and refinement of signal [67].

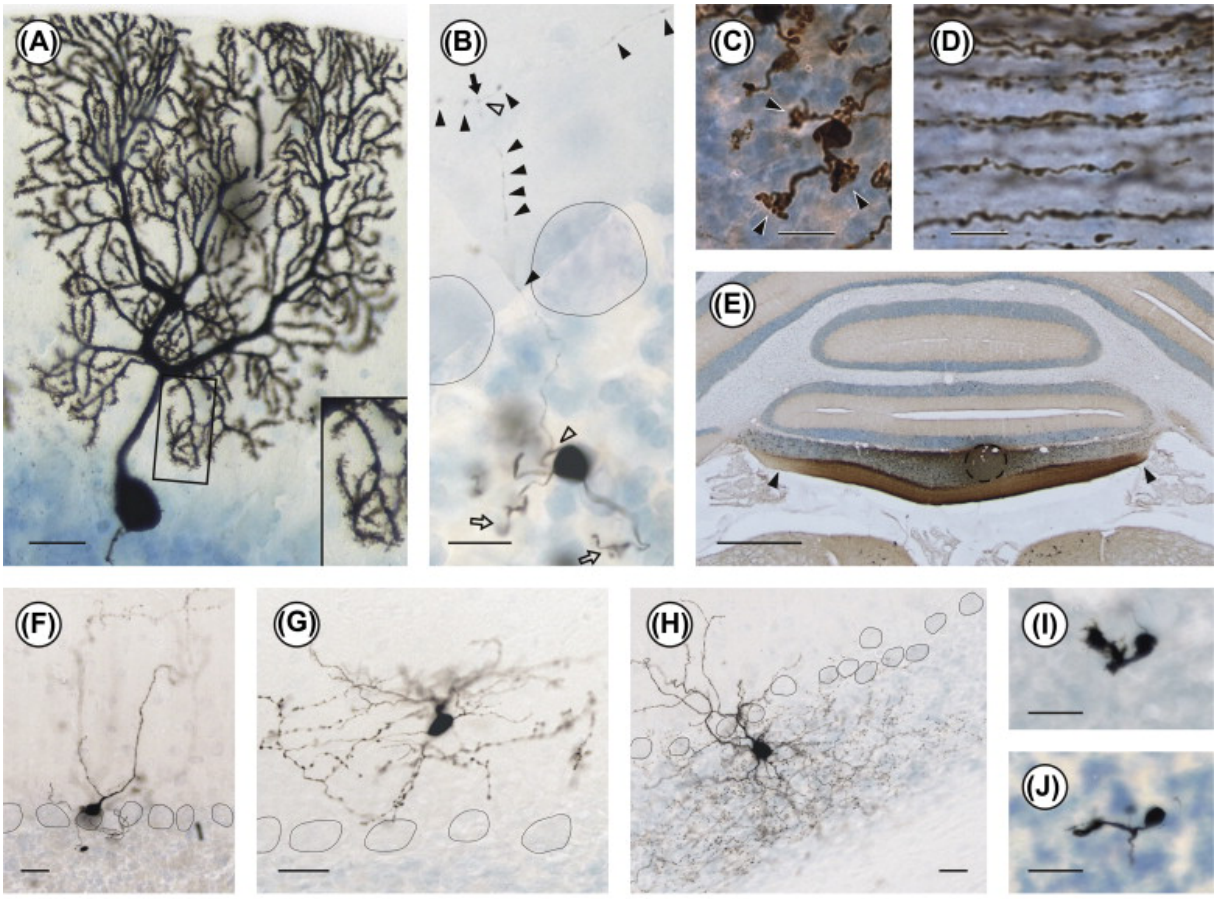

Figure 2: Cell types in the cerebellum
A) Golgi-stained Purkinje cell. Insert = zoom of dendritic tree, demonstrating spines B) Granule cell stained by juxtacellular labelling technique. Axon depicted by arrowhead. C) Granule cells labelled with biotinylated dextran amine (BDA). Arrowheads depict short dendrites with claw-like endings. D) Parallel fibres in the molecular layer visualised by BDA injection. Varicosities demonstrate synaptic boutons. E) Low magnification image of a coronal cerebellar section. Cholera toxin b-subunit (CTb) was iontophoretically injected into lobule X, labelling parallel fibre bundles (arrowheads). F) Basket cell. G) Stellate cell. H) Golgi cell. I, J) Unipolar brush cells. Cells in F-J were labelled juxtacellularly. Scale bars = 25 µm in A, F, G, H, I, J; 10 µm in B, C, D. Open circles in B, F, G, H = PC somata. Adapted from Ruigrok et al. [148].

The most abundant cell type in the brain, the cerebellar GC, is the major excitatory cell in the cerebellum. Each GC has on average four short dendrites that end in claw-like structures protruding into the mossy fibre (MF) bouton (Figures 2C, 3 and 5D-F) [90]. Because of its short size, the cerebellar GC is electrically compact, allowing it to integrate MF inputs quickly and with high precision [37]. The MF bouton transmits at frequencies of up to 700 Hz *in vivo* with extremely high fidelity [138]. Each GC can receive inputs from up to four MF boutons and send unmyelinated PF axons to several hundred PCs [14, 85], initiating simple spikes in PCs that transmit information in their frequency [9]. The MF rosette is regulated by Golgi internuerones (Figure 2H and 3), which have their cell bodies in the GCL. They release GABA onto GC dendrites, but also extend their own dendrites into the ML and are excited by PFs, thus providing regulatory feedback to this circuit and limiting activity of the PFs [44].

Other internerones in the cerebellum include unipolar brush cells, which are one of the few excitatory interneurones in the brain. They are highly concentrated in lobes IX and X; they reside in the GCL and receive MFs from the vestibular system onto their singular, brush-like dendrite and they project locally into the GCL via their own MF synapse (Figure 2I-J) [148]. They are modulated by Golgi cells and hypothesised to function to boost signals from the vestibular system and regulate body, head and eye position [123, 148]. Also residing in the GCL, lugaro cells are selectively excited by serotonin and extend long partially myelinated axons to the ML, where they run parallel to PFs, and to the GCL where they inhibit Golgi cells via the release of both glycine and GABA [40]. Lugaro cells could act to enhance activity, by inhibiting the GABAergic Golgi or Purkinje cells [159]. Finally, candelabrum cells have their cell bodies in the PCL and their dendrites extend into both the ML and the GCL. Their axons protrude into the ML and are both glycinergic and GABAergic, although their exact role in cerebellar network remains to be fully elucidated [148].

Bergmann glia are the supporting cells of the cerebellum. During development, they provide structural support to the granule cells during their migration from the external GCL (EGL) to the internal GCL (IGL) [196] and may play a role in synaptic pruning of CFs [128]. Bergmann glia also support neurones by regulating glutamate and potassium concentrations [184].

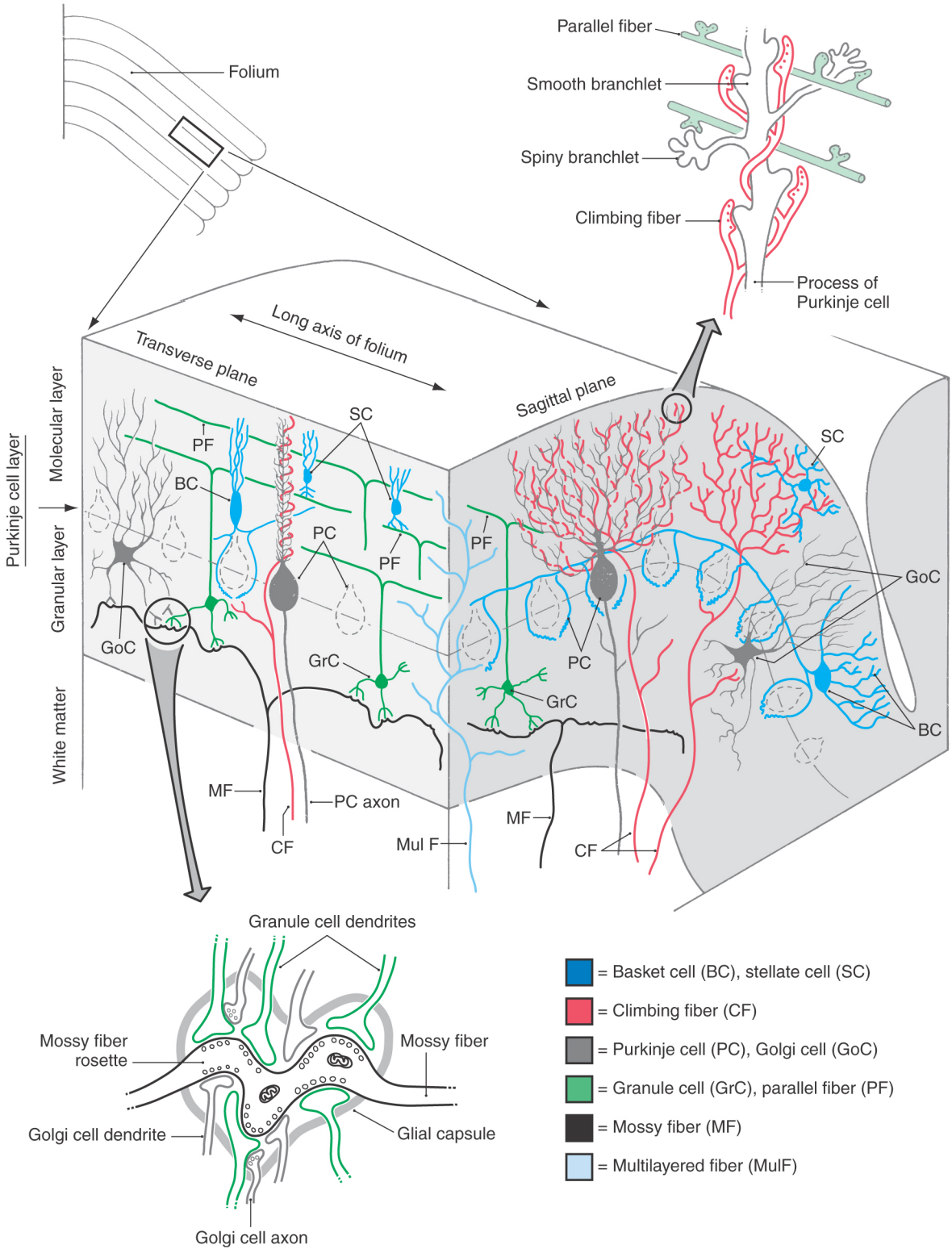

Figure 3: Cerebellar microcircuitry

Schematic demonstrating cell types and their interactions in the cerebellar cortex in transverse and sagittal planes. Enlargements: focus on structural differences between synaptic connections of cerebellar afferents: MF axon varicosities contact GC dendrites, regulated by Golgi cell axons, making up the mossy fibre rosette (lower left); parallel fibre and climbing fibres innervation of Purkinje cell dendrites (upper right). Adapted from Haines [60].

3.2.2 Cerebellar afferents and efferents

The main afferent systems contributing to the cerebellar cortex are MFs, CFs and morphologically distinct fibres arising from brain regions such as the locus coeruleus and the raphe nucleus [164]. MFs originate from a number of brainstem and spinal cord regions and terminate onto granule cell dendrites in three zones: the vestibulo-cerebellum, the spino-cerebellum and the cerebro-cerebellum, as well as sending collaterals directly to the deep cerebellar nuclei [178].

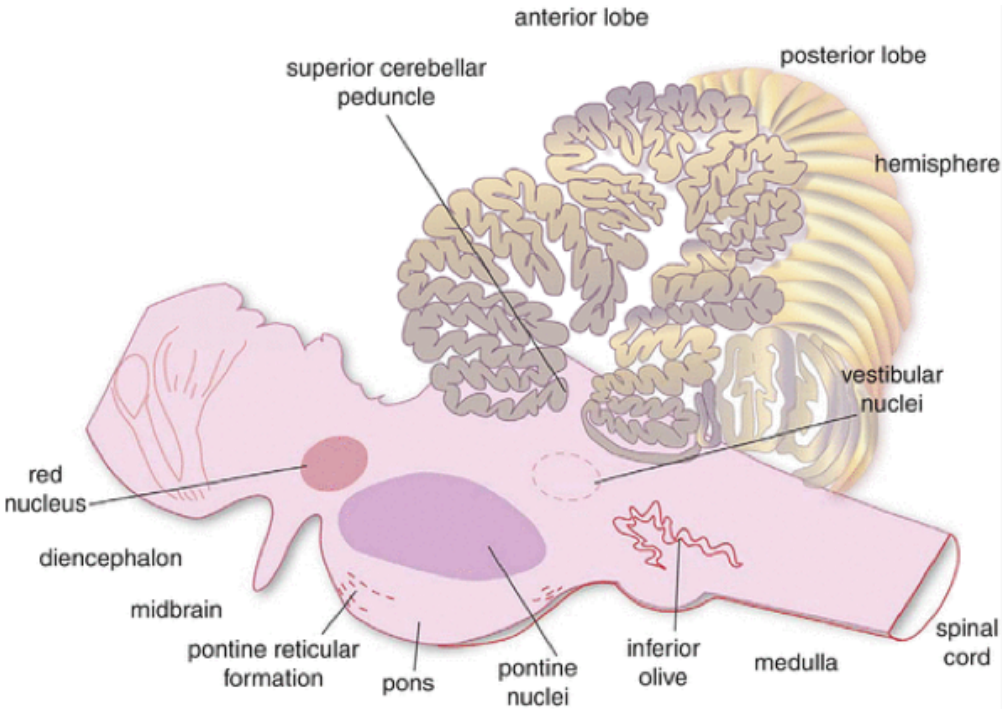

Figure 4: Cerebellar afferents and their sources
Schematic of a parasagittal plane through the human brainstem and cerebellum demonstrating sources of afferent and efferent connections discussed above. Adapted from Miall [120].

The vestibulo-cerebellum, comprised of the flocculonodular lobe (lobe X), is responsible for balance, eye movements and other vestibular reflexes. It receives sensory signals from the inner hair cells of the semicircular canals, either directly or via the medial and inferior nuclei. Information on balance and orientation projects to the flocculonodular lobe via the inferior cerebellar peduncle. Efferents from the flocculonodular lobe send signals back to the vestibular nuclei in the brain stem through the fastigial nucleus [107, 120].

The spino-cerebellum is located at the anterior lobe in the vermis (lobes I-V at the midline) and the immediate hemispheres. As the name suggests, it receives proprioceptive and somatosensory information from the spinal cord and is involved in muscle and eye movements. The spino-cerebellum projects afferents via the fastigial and interposed nucleus to cortical and brainstem areas responsible for movement and muscle control [143].

Receiving efferents from the pons, the cerebro-cerebellum is the most recent addition to the cerebellum in terms of evolution. So-called because inputs and outputs of this region almost entirely involve the cerebral cortex, this region is comprised of the hemispheres and posterior lobes (lobes VI-IX) at the vermis. The cerebro-cerebellum receives signals sent by, amongst others, layer 5 pyramidal cells by way of the pons and projects its efferent fibres via the dentate nucleus to premotor, prefrontal and motor regions of the cortex [120, 148]. The cerebro-cerebellum is involved in planning, executing and coordination of voluntary movements. There is also some evidence that the cerebellar hemispheres could be involved in schizophrenia and autism [100].

In contrast, CF afferents arise from one source, the inferior olive located within the medulla oblongata of the brainstem. The inferior olive receives somatosensory and noxious information from a number of areas, such as vestibular, spinal and descending cortical areas and projects CFs into defined parasagittal bands within the cerebellar cortex [177]. CFs are pruned during development to establish a one CF to one PC ratio [11]; these fibres synapse directly onto the proximal branches of the PC dendritic arbour, giving rise to the strongest depolarisation observed in any neurone, initiating the so-called “complex spike” [43] in the PC, modulating the dynamic firing properties of Purkinje cells and motor learning [70, 95]. CFs also send collaterals to the deep cerebellar nuclei and cerebellar interneurones [126].

The cerebellum also receives serotonergic, noradrenergic, dopaminergic and cholinergic afferents, which serve to modulate cerebellar microciruitry in learning and control of movement [148, 159].

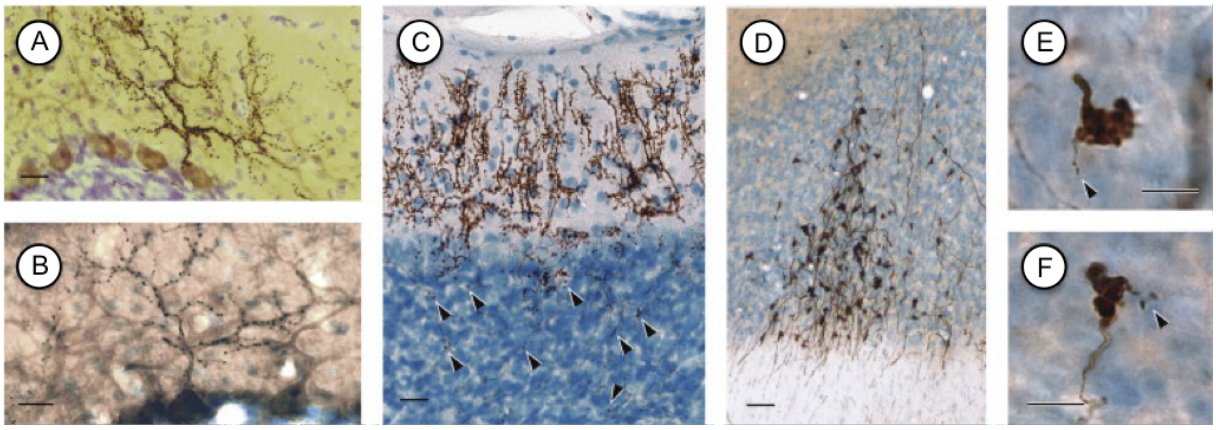

Figure 5: Cerebellar afferent synapses
A, B) Sagittal cerebellar section. Climbing fibres labelled by BDA injection and Purkinje cells labelled with Zebrin II. C) Transverse cerebellar section. Climbing fibres labelled by CTb. Arrowheads depict labelled varicosities in the granule cell layer. D) Cluster of mossy fibres labelled with BDA. E, F) zoom of D) arrowheads depict small tendrils emitting from the MF glomerulus. Scale bars = 25 µm in A, B, C, D; 10 µm in E, F. Adapted from Ruigrok et al.[148].

The largest of the precerebellar nuclei, the pontine nuclei are regarded as the first integrators of information from the cerebral cortex, receiving an "efference copy", a representation of efferent motor signals, from the motor cortex and processing these signals for use of the cerebellum. Here, discrepancies between the efference copy and sensory feedback are modulated by error signals from the inferior olive in order to fine-tune movement [86, 102]. The heterogeneity of these projection neurones could contribute to their ability to integrate the complex connectivity between the cortex and the cerebellum [102], also sending collaterals to the deep cerebellar nuclei [178]. Pontine neurones originate from the posterior rhombic lip and tangentially migrate to their destination in the ventral pons, tightly regulated by a balance of attractive and repulsive cues [163].

3.2.3 Target-derived signalling in cerebellar mossy fibre afferents

Upon arrival in the cerebellum, pontine (and other precerebellar) afferents path-find their way to the inner GCL. Ground breaking work by Patricia Salinas' laboratory [4, 63, 108] revealed a mechanism by which MF glomeruli mature and differentiate upon proximity to cerebellar GCs.

Wnt signalling proteins activate a number of signalling cascades which play an important role in embryonic development as well as neuronal differentiation, axonal and dendritic growth and guidance, synaptic maturation, as well as function and plasticity [145]. Binding of Wnt to the Frizzled receptor activates at least three divergent pathways that are brought together by the scaffolding protein Dishevelled (Dvl): the canonical Wnt/β-catenin, the planar cell polarity (PCP) and the Wnt/Ca^{2+} pathways. In the canonical pathway, activation of Dvl disassembles a complex containing β-catenin and glycogen synthase kinase 3β (GSK3β), inhibiting the "destruction complex" (under non-Wnt activated conditions, GSK3β causes the degradation of β-catenin) and leading to an accumulation of β-catenin, which then translocates to the nucleus and activates gene transcription. In the PCP pathway, Dvl activates Rho-GTPases and JNK signalling pathway in order to remodel the Actin cytoskeleton. In the Ca^{2+} pathway, Wnt leads to an increase in intracellular Ca^{2+} which activates protein kinase C (PKC) and Ca^{2+}/Calmodulin-dependent protein kinase II (CamKII), Ca^{2+}-sensitive kinases, leading to gene transcription [26, 31, 56, 145, 150].

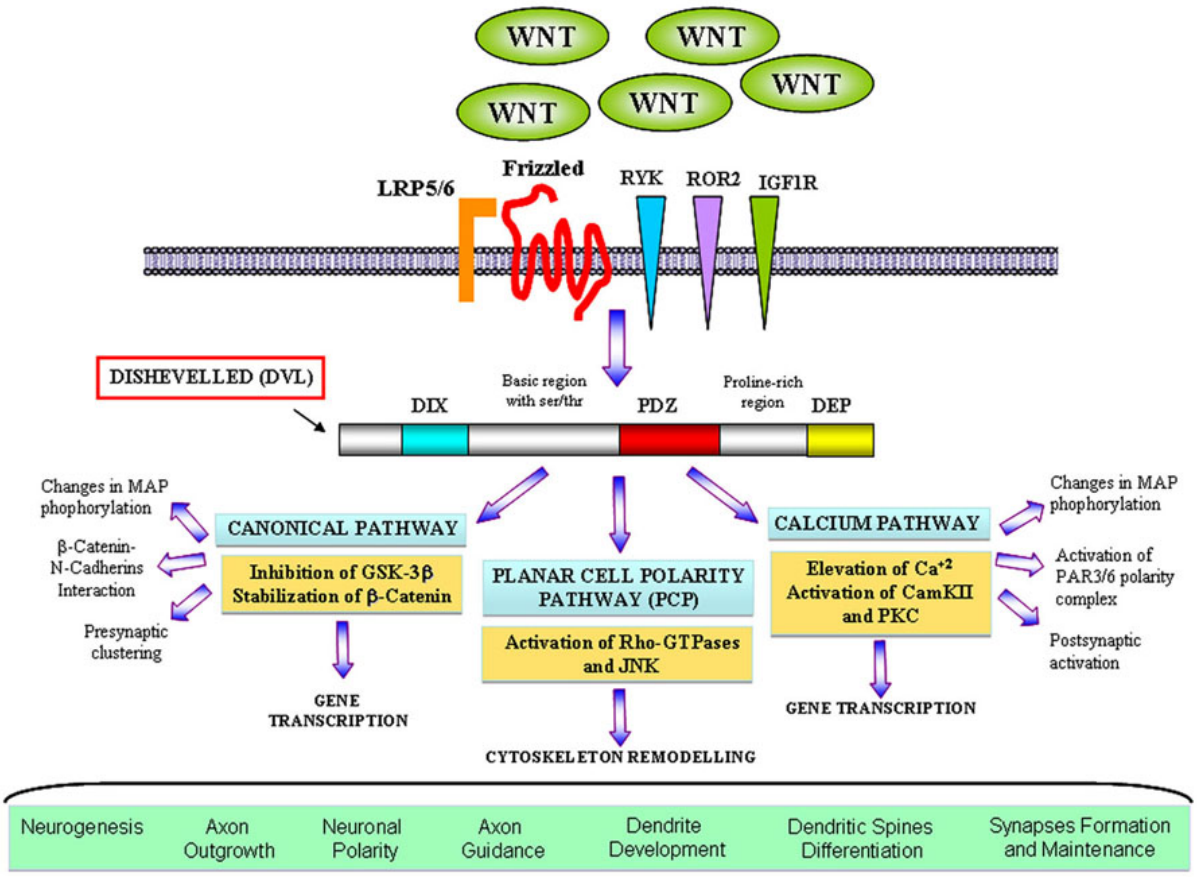

Figure 6: Wnt signalling pathways

Wnt proteins bind to Frizzled receptors and activate Dvl. Canonical pathway: β-catenin accumulates and translocates to the soma, where it activates gene transcription (under non-Wnt activated conditions, GSK3β activity leads to β-catenin ubiquitination and degradation). PCP pathway: Dvl signals small Rho-GTPases via interaction with Daam1, inducing gene transcription and Actin cytoskeleton remodelling. Wnt/Ca^2 pathway: Dvl induces increase in intracellular Ca^{2+}, leading to PKC and CamKII activation, modulating spine morphology, cell polarity and synapses. Adapted from Garcia et al. [55].

Wnts are secreted by postsynaptic GCs during their migration from the EGL to the IGL as MF afferents enter the cerebellum from the pons and other precerebellar areas. When MFs come into contact with GCs, their morphology changes and they transition from a pathfinding phase to a maturation phase. By remodelling their cytoskeleton, growth cones increase in size and complexity as they spread and become interdigitated with GC dendrites [66]. Hall et al. [63] elegantly demonstrated that this phenomenon is dependent on Wnt-7a mediated microtubule reorganisation by initiating growth cone remodelling in pontine explants with Wnt-7a treatment, which can be mimicked by lithium (inhibits GSK-3β) and inhibited by blocking Frizzled. Furthermore, Wnt-7a knockout (KO) mutants have much smaller MF presynaptic areas in the GCL *in vivo* at P8-12 (P = postnatal day), which restore to wildtype (WT) size by P15. This points to a lag in maturation and therefore size of MF rosettes during development. An even more severe attenuation in MF size, which was still maintained at P15, can be observed when both Wnt-7a and Dvl were knocked out - indicating that

perhaps other Wnts such as Wnt-7b could compensate for the loss of Wnt-7a and rescue the phenotype [4].

Other target-derived factors such as Cadherin-7, BMP4, the brain-specific RasGEF very-KIND and FGF-22 have also been shown to regulate the formation and maturation of MF synapses [74, 94, 103, 175]. Interestingly, inhibition of FGF-22, which is expressed by GCs during postnatal cerebellar development, also leads to perturbed MF differentiation in the form of reduced MF glomerular size. The FGF-22 phenotype, however, appears more severe than Wnt-7a and/or Dvl KOs as MFs in this model are also reduced in the number of MFs per GC [175], hinting that FGF-22 may be upstream or an earlier process than Wnt-7a-mediated maturation in the numerous hierarchical array of organisers of synapse formation, differentiation and maturation [152].

Due to its repetitive and relatively simple circuit, the cerebellum has been extensively studied and modelled; the reliability of its network lies in the diversity and functionality of the synapses involved. Pontocerebellar Hypoplasia patients clearly suffer from dysfunctional circuitry as well as cell loss, as evidenced by impaired motor control and brain anatomy. Synaptic transmission is fundamental to this circuitry. It is thus proposed that, due to its presynaptic localisation, loss of the active zone (AZ) protein Piccolo - or its role in supporting protein-protein interactions with AZ binding partners (see below) - could contribute to the cerebellar network perturbation seen in these patients.

3.3 Synaptic transmission

Efficient and reliant communication between neurones is mediated by highly specialised structures coined ‘synapses’ by Sherrington in 1987. Inspired by the work of Ramón y Cajal, Sherrington wrote that, “as far as our present knowledge goes, we are led to think that the tip of a twig of the [axonal] arborescence is not continuous with but merely in contact with the substance of the dendrite or cell body on which it impinges. Such a special connection of one nerve cell with another might be called ‘*synapsis*’.” [161].

In order to process information, the trillions of neurones in the human brain need to communicate with one another in a highly spatially and temporally controlled manner. This control is mediated by an ensemble of pre- and postsynaptic proteins, as well as trans synaptic cell-cell adhesion and signalling molecules that contribute to synaptogenesis and the precise alignment of pre and post specialisations. One form of such communication occurs when chemical neurotransmitters, released into the synaptic cleft in response to an electrical action potential (AP), bind to postsynaptic receptors, transforming the signal back into electrical information that either promotes the depolarisation or hyperpolarisation of the postsynaptic plasma membranes [167].

Structurally, synapses consist of a presynaptic bouton filled with synaptic vesicles (SVs) organised into pools: the readily releasable pool (RRP) contains SVs which are docked to the AZ, primed and ready for release upon the influx of Ca^{2+}; the recycling pool provides additional SVs required for sustained release; and the reserve pool, which constitutes the majority of vesicles (~80 – 90 % in most terminals) in the presynaptic bouton and is only released in response to supraphysiological stimulation in the event of depletion of both the RRP and the recycling pool [73, 135, 142]. The presynaptic bouton and the AZ, the site of SV docking and fusion, are situated juxtaposed to the postsynaptic density (PSD). Within this latter structure are a large number of postsynaptic receptors primed to receive the presynaptically released chemical signals. These two membranes are separated by the synaptic cleft, a ~20 nm gap (at central synapses) between the AZ and PSD [53].

3.3.1 The synaptic vesicle cycle

Historical work by Heuser and Reese [76] described the cycling nature of SVs; demonstrated by the area of plasma membrane (PM) briefly increasing after SVs fuse and release their neurotransmitter via exocytosis, adding their membrane to the presynaptic terminal. This area then decreases again as PM is retrieved and endocytosed into the terminal to replenish SVs and to keep the size of the presynaptic PM in balance [76, 101]. This process has been studied extensively since and the mechanisms underlying membrane retrieval and the SV cycle are beginning to be elucidated.

As an AP arrives at the presynapse, it triggers the opening of voltage-gated calcium channels (VGCCs), elevating the level of Ca^{2+} in the presynaptic bouton which binds to Synaptotagmin and triggers exocytosis of neurotransmitter (NT) from SVs [75, 168] (Figure 7B). This process is reliant upon SNARE (soluble NSF (N-ethylmaleimide-sensitive factor) attachment protein (SNAP) receptor) and SM (Sec1/Munc18-like) proteins. SNARE proteins force the PM and the SV membrane together by forming an α-helical containing trans-SNARE complex, supported by SM proteins, triggering fusion between the two membranes thereby releasing NTs into the synaptic cleft (Figure 7B). The remarkable speed at which SVs are able to exocytose is unique to neuronal synapses and is in part due to the docked and primed state of vesicles in the RRP at the AZ, which allows for rapid NT release and therefore signal transduction required by the arrival of APs at up to 700 Hz [138, 144, 168, 194]. This rapid rate of exocytosis, however, requires a compensatory endocytosis in order to maintain PM integrity and to replenish SVs at the local level.

Endocytosis of SV proteins can be achieved by a number of different mechanisms: 1) kiss-and-run membrane retrieval, 2) Clathrin-mediated endocytosis (CME), 3) ultrafast endocytosis and 4) bulk endocytosis [101]. Briefly, kiss-and-run endocytosis involves a transient fusion of the SV with the PM, releasing NTs into the synaptic cleft, before the SV is retrieved intracellularly and refilled with NT within the terminal [1, 189]. During CME (Figure 7D), the fused SV proteins move from the

AZ to the peri-active zone to be retrieved by Clathrin and other endocytic factors. Together they form a Clathrin coat which forces the membrane into a deeply invaginated pit, eventually forming a spherical shape with a residual "neck" attaching it to the PM. This neck is then severed by a dynamin ring, constricting the membrane until the vesicle is freed. The vesicle sheds its Clathrin coat and can be refilled with NT, or fuses with endosomal membranes to enter the endosome cycle [1]. Ultrafast endocytosis is Clathrin-independent and rather depends on Actin polymerisation. It involves rapid retrieval of membrane in 50-100 ms (200-fold faster than CME) in order to maintain PM surface area [191]. Bulk endocytosis occurs mostly at supraphysiological levels of stimulation, rapidly retrieving excess membrane from the PM surface to be later sorted through endosome and/or degraded by the endolysosomal pathway. Initial steps in this pathway are also Clathrin-independent and serve to maintain PM integrity under high frequency stimulation [32, 190]. At the cerebellar MF, release stimulated by a single AP evokes ultrafast endocytosis whilst sustained, faster transmission requires a slower form of endocytosis dependent on Clathrin, Dynamin and Actin [22, 38].

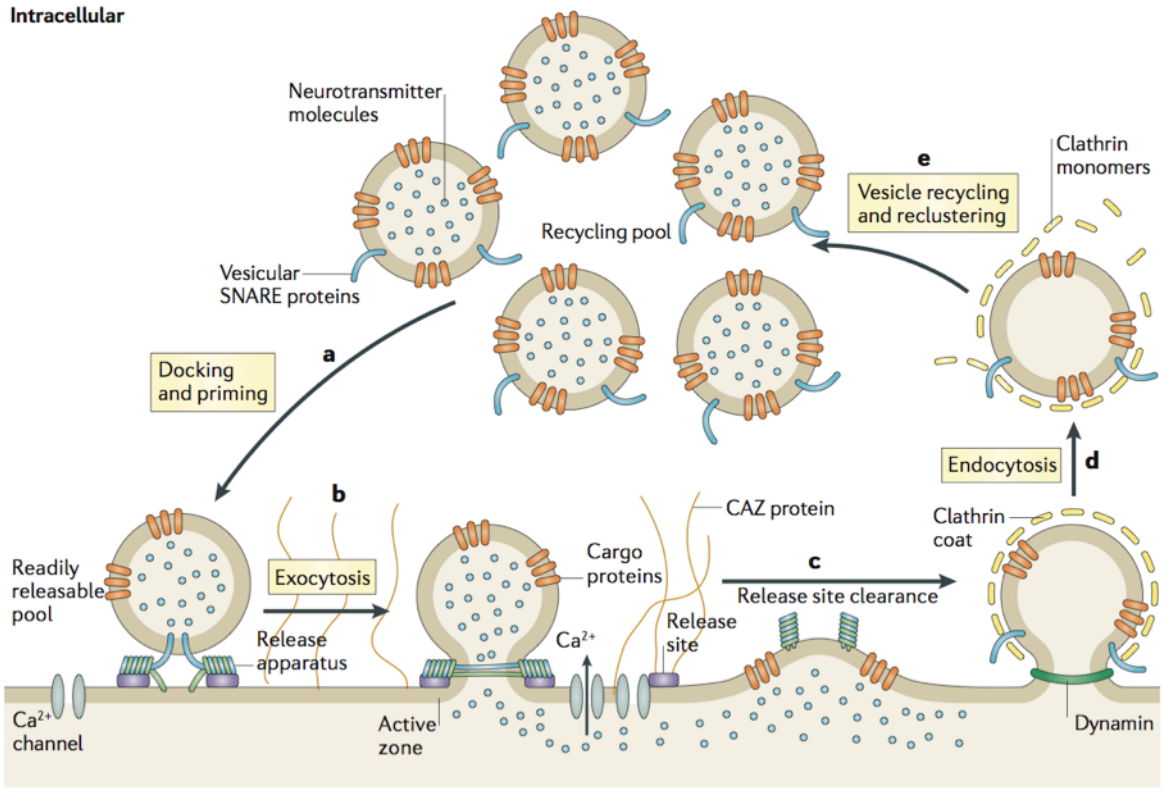

Figure 7: The synaptic vesicle cycle

Schematic of Clathrin-mediated endocytosis in the SV cycle. The readily releasable pool consists of SVs in their docked and primed state (A) until an increase in intracellular Ca^{2+} triggers exocytosis at the active zone (B), releasing NT into the synaptic cleft. Subsequently, the release machinery is cleared (C) and endocytosis of SV membrane occurs at the peri-active zone, primarily via Clathrin-mediated endocytosis (D). Adapted from Haucke et al. [73].

3.3.2 The active zone

The cytoskeletal matrix assembled at active zones (CAZ) is characterised by an electron-dense matrix of presynaptic proteins that engage SVs that are docked to the PM, ready for fusion and the release of neurotransmitters. The CAZ is defined by a number of multidomain scaffold proteins including Rab3-interacting molecules (RIMs), Munc13, RIM-binding proteins (RIM-BPs), α-Liprins, ELKS2/CAST/ERC as well as Piccolo and Bassoon (Figure 8). Together these molecules support the maturation of SVs, their translocation to the AZ, the creation of the readily releasable pool of SVs that are docked and primed at the AZ, and also position voltage-gated Ca^{2+} channels [3, 58, 167]. The CAZ is uniquely specialised and most components highly conserved across evolution. The two largest proteins at the CAZ, Bassoon and Piccolo, were initially thought to be vertebrate-specific, however, orthologs have been found in invertebrate systems such as *Drosophila melanogaster* in the form of Bruchpilot and Fife, respectively [18, 180]. Fife is a Piccolo-RIM hybrid homologue and consists of a RIM protein with the zinc finger (ZF), PDZ, C2A and C2B domains of Piccolo. Loss of Fife in *Drosophila* leads to a reduction in SV number as well as deficits in SV clustering, leading to a reduction in evoked synaptic transmission at the neuromuscular junction [3, 18]. In contrast, the loss of Bruchpilot, which appears to be a hybrid of Bassoon and ERC, impairs the formation of presynaptic AZs at the *Drosophila* neuromuscular junction [97, 180].

The CAZ proteins are highly specialised and precisely organised, working in concert to orchestrate the tightly regulated release of SVs. To investigate the role of Piccolo in PCH3, we must consider what is known about this enigmatic instrument.

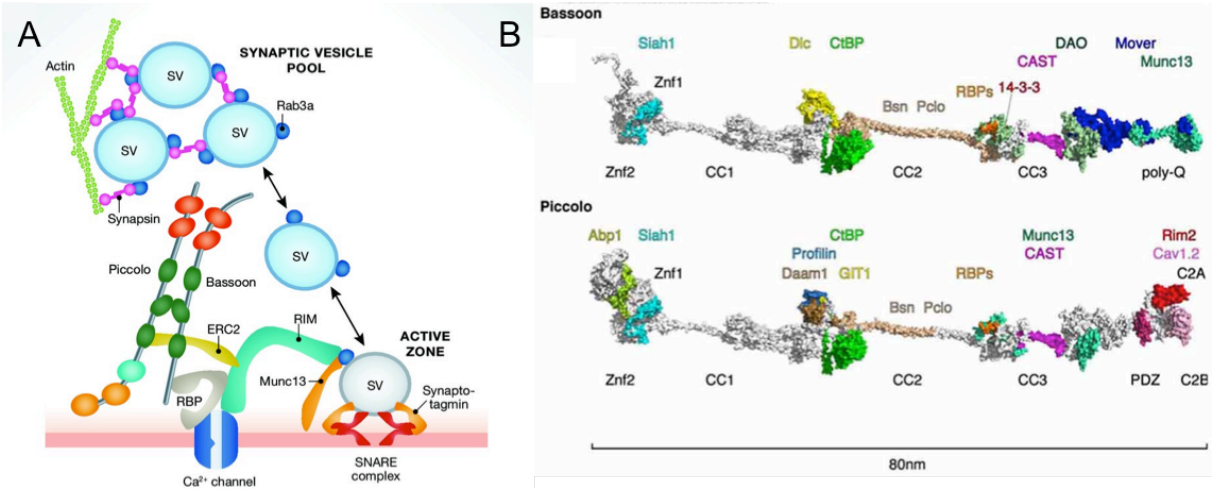

Figure 8: Proteins of the CAZ: focus on Piccolo and Bassoon

A) Schematic of CAZ proteins orchestrating the release of SVs from the presynaptic terminal. Synapsin and Actin cluster SVs in the recycling pool; docking and priming is mediated by proteins of the SNARE complex and RIM, Munc13 and Rab13 respectively; Synaptotagmin controls fusion of SVs; the scaffolds Piccolo and Bassoon create a platform for interaction with RIM-BP (RBP), RIM, ELKS and voltage-gated Ca^{2+} channels. Adapted from Ackermann et al. [3, 58]. B) *In silico* modelling of Piccolo and Bassoon structures demonstrating

putative binding partners. Colours in the structure correspond to given protein names. Adapted from Gundelfinger et al. [58].

3.4 Piccolo, the CAZ protein

Piccolo, also known as Aczonin, is a large 560 kDa multidomain scaffold protein localised to the presynaptic active zones of vertebrate synapses [23, 47, 186, 200] and structurally related to Bassoon [47, 58] (Figure 8). Piccolo consists of 10 Piccolo/Bassoon homology domains (PBH), two N-terminal zinc finger (ZF) domains, three coiled-coil (CC) domains, a single PDZ domain and two C-terminal C2 domains (C2A/C2B) [47, 48]. Piccolo uses its multidomain structure to interact with a number of presynaptic proteins involved in the dynamic assembly of presynaptic filamentous-actin (F-Actin) and the regulated release of neurotransmitter substances [3, 179]. It is one of the first proteins recruited to nascent synapses [200], where it stably becomes integrated into the CAZ [47] of glutamateric, GABAergic, cholinergic, glycinergic, dopaminergic synapses among others [3, 58].

Loss of function studies have demonstrated that Piccolo and its smaller isoform Piccolino are critically important in the formation of ribbons assembled at the AZ of ribbon synapses in the vertebrate retina [125, 139]. It has also been found to be important for the dynamic functionality of hippocampal presynaptic boutons [104, 182] as well as their structural integrity [183]. Piccolo loss of function is also linked to dopamine transporter dysfunction [24] and major depressive disorders [29, 169].

3.4.1 Piccolo and Actin

The highly specific presynaptic localisation of Piccolo within the CAZ [23] and its binding to SV-associated proteins such as Pra1 and Abp1 [47, 49] imply a role for Piccolo in the recycling and turnover of SVs. Indeed, Piccolo has been found to regulate the dynamic association of SVs with presynaptic Actin via its activity dependent recruitment of CaMKII and Actin into presyanptic boutons and the subsequent phosphorylation of Synapsin by CaMKII, which in turn negatively regulates SV exocytosis [104]. Synapsin is responsible for tethering SVs in the reserve pool to the Actin cytoskeleton and its Ca^{2+}- triggered phosphorylation by CaMKII reduces affinity for both Actin and SVs, thereby mobilising SVs into the readily releasable pool [41]. Piccolo also appears to modulate the dynamic assembly of presynaptic F-Actin; a cytoskeletal filament that operates in concert with Synapsin [135]. A more recent study found that the observed increase in Synapsin dispersion and subsequent SV exocytosis in Piccolo knockdown neurones can be blocked by stabilising F-Actin with Jasplakinolide and phenocopied by knocking down Profilin2, another Actin binding protein involved in the dynamic assembly of Actin filaments [182]. Mechanistically, Piccolo appears to regulate the dynamic assembly of F-Actin through its direct interactions with Profilin and Daam1 [179, 186], which also respond to signals from the Wnt/Dvl pathway. In cultured hippocampal neurones, Daam1, Profilin and Piccolo all colocalise within presynaptic boutons [179, 182]. Both Daam1 and Profilin

interact with the central domain of Piccolo, which forms a platform onto which Actin filaments are assembled [179], providing further evidence for Piccolo's involvement in Actin dynamics and thereby regulation of synaptic transmission.

3.4.2 The role of Piccolo in endocytosis: loss of function studies

Endocytosis is a crucial step in the SV cycle, playing a fundamental role in the retrieval of SV proteins and membranes from the presynaptic PM. This process of SV protein retrieval and sorting is also essential for the removal of mis-folded proteins, the rejuvenation of SVs and the integrity of the presynaptic boutons [105].

A recent study of hippocampal synapses has implicated Piccolo in this step of the SV cycle. Specifically, Ackermann et al. (2019) could show that Piccolo is crucial for the formation and subsequent maturation of early endosomes. Of note, loss of Piccolo function was found to attenuate the recycling of SVs. Mechanistically, it was shown that, in the absence of Piccolo, its interacting partner Pra1 [47] was not recruited to presynaptic boutons, preventing the subsequent activation of Rab5 and thus the formation of early endosomes [2]. The consequences of this defect were quite profound. Namely, in the absence of Piccolo, the authors observed a dramatic reduction of SVs within hippocampal synaptic boutons. This was paired with an increase in numbers of early endosome-like structures, pointing to a block in the SV cycle. Surprisingly, the loss of Piccolo didn't have a profound effect on the kinetics of SV docking and fusion, as parameters such as excitatory postsynaptic current (EPSC) amplitude, release probability, readily releasable pool and paired pulse ratio were not changed. However, sustained synaptic transmission was impaired when a 10 Hz stimulation was given over 5 seconds, perhaps due to fewer SVs per terminal. Consistently, FM1-43 destaining kinetics revealed a much slower rate of destaining at 10 Hz over 9 seconds, indicative of a slower retrieval of SV membranes in the boutons of Piccolo knockout rats ($Pclo^{gt/gt}$) [2].

At a different synapse type, the endbulb of Held in the cochlear nucleus of the auditory system, targeted deletion of Piccolo's exon 14 in mice ($Pclo^{ex14/ex14}$) allowed the analysis of synapses lacking some of the larger Piccolo isoforms [21]. Similar to that observed in the $Pclo^{gt/gt}$ rat model [2], Butola and colleagues [21] found there to be fewer SVs per terminal. In the case of the endbulb of Held, there was a heightened loss of SVs within 40 nm of the AZ, which is regarded to comprise SVs in the readily releasable pool. Here, evoked EPSC amplitude was reduced, while spontaneous events remained unchanged between $Pclo^{ex14/ex14}$ and WT. Synapses of the endbulb are specialised in their ability to fire at much higher frequencies than hippocampal pyramidal neurones, up to 450 Hz [195], allowing for the detection of subtle differences in membrane and SV recycling. Butola et al. [21] found that Piccolo-deficient endbulb of Held synapses recover from short-term depression (STD) induced by a train of 50 APs at 100 Hz at a three-fold slower rate than WT, again suggesting a possible impairment in replenishment of SVs, or in the numbers of SVs at the RRP.

The Calyx of Held is another large synapse of the auditory system capable of high frequency transmission [50]. Similar to other Piccolo LOF studies, frequency and amplitude of spontaneous events were not affected in the *Pclo*$^{ex14/ex14}$ mouse, nor the amplitude or kinetics of evoked EPSCs. The loss of Piccolo, however, did affect SV pool dynamics and replenishment at Calyx synapses, displaying less organised release of SVs from distinct pools [132]. This should reserve slow-releasing SVs as a backup for sustained periods of NT release, thereby preventing failure of transmission under stimulation for extended periods of time. This mechanism could be particularly important for synapses such as the Calyx, which can reach frequencies of up to 300 Hz [132, 149].

Taken together, these studies suggest a role for Piccolo in vesicle replenishment and organisation of SVs at the presynapse. Depending on the neuronal subtype, Piccolo appears to play slightly different roles, perhaps more prominently in those subtypes that demand a high turnover of SVs.

3.4.3 Bassoon, a homolog of Piccolo

Despite the large size and numerous binding sites of the Piccolo protein, the phenotypes discussed are not as dramatic as one could expect, especially in terms of synaptic transmission. One possible explanation is the high degree of structure homology shared between Piccolo and Bassoon, a second large multidomain AZ scaffolding protein (Figure 8). Similar to Piccolo, Bassoon has been found to play critical roles in the assembly and function of ribbon synapses of the retina and the auditory system [39, 52, 96, 141, 173]. Within the auditory system, Bassoon was also found to be upregulated at the endbulb of Held upon deletion of exon 14 of the *Pclo* gene [21], pointing to a compensatory upregulation of this protein. However, in the case of the Calyx of Held, there was no difference in Bassoon expression between *Pclo*$^{ex14/ex14}$ and WT [132]. Furthermore, Ackermann et al. [2] report no significant change in Bassoon expression in Piccolo knockout (*Pclo*$^{gt/gt}$) brain lysates. Despite conflicting evidence for the compensatory overexpression of Bassoon, it can still be said that, since Bassoon is still present in Piccolo LOF models, and considering the shared homology between the two proteins, the presence of Bassoon could serve a number of compensatory functions in the absence of Piccolo.

Bassoon has also been implicated in the SV cycle at the endbulb of Held. Schulz and colleagues [158] noted a stronger increase in release probability and a larger quantal size in Bassoon-lacking (*Bsn*$^{-/-}$) endbulb synapses despite a reduced number of readily releasable SVs and slower vesicle replenishment. The latter is evidenced by enhanced short-term depression, a reduction in postsynaptic response after repeated stimulation [75], and a slower recovery from such depression in Bassoon mutant synapses compared to WT. Authors also observed an increase in PSD length of *Bsn*$^{-/-}$ postsynaptic bushy cells which, together with their increased excitability, is most likely a homeostatic scaling in response to impaired excitatory transmission at these central synapses [158].

Of particular interest to this thesis, the MF-GC synapse was investigated in Bassoon knockout mice. The MF-GC synapse is another high-frequency transmitting synapse that requires fast SV turnover [22]. Similar to Piccolo LOF and the aforementioned studies, inactivating Bassoon had no effect on baseline transmission, but, when the system was required to sustain NT release, $Bsn^{-/-}$ MF synapses showed enhanced synaptic depression, a slower recovery from said depression and Bassoon was again found to be involved in fast reloading of SVs to the readily releasable pool [64].

Importantly the roles of Bassoon and Piccolo at active zones are not limited to synaptic transmission. This is best illustrated in boutons lacking both proteins. Here, synaptic integrity and recovery from sustained synaptic transmission are further impaired. At both the endbulb and the Calyx of Held, partial disruption of Bassoon on top of Piccolo inactivation exacerbated the deterioration in the fast component of recovery from STD, highlighting the role of these proteins in vesicle replenishment [21, 132]. Furthermore, the integrity of the presynapse is reliant on the presence and cooperation of these two proteins, as double knockdown triggers the disintegration of synapses as well as ubiquitination and degradation of a number of synaptic proteins [183]. Thus, the loss of one or both can have broad reaching effects on the integrity and functions of a variety of synapses.

3.4.4 Developmental expression of Piccolo and Bassoon

Piccolo and Bassoon are among the first proteins to arrive at nascent synapses [200]. Cellular studies have shown that they are transported together with other components of the active zone on Golgi derived Piccolo-Bassoon transport vesicles (PTVs) [200]. Here, they are delivered to nascent synapses in a quantal manner requiring the insertion of only 2-3 PTVs to create a functional AZ [160] in as little as 20 minutes post initial axo-dendritic contact [58, 109]. These data support a role for both scaffolding proteins in the nascent assembly of active zones. Consistent with this idea, PTVs containing Piccolo and/or Bassoon are found to accumulate in axonal growth cones and to deposit at dendritic contact sites [23, 110, 199]. Although not well understood, Piccolo puncta are situated along Actin filaments within growth cones [199, 200], which may relate to its dual role in the regulation of F-Actin assembly [179].

Within the Cerebellum, Piccolo expression peaks at P15 and strong immunoreactivity can be seen in the molecular layer and granule cell layers of the Cerebellum [23, 186, 200]. In dissociated hippocampal neurones, Piccolo is expressed in the growth cone and distal part of the axon at 3-4 days *in vitro* (DIV) [200]. In mature brains, Piccolo is expressed at every synapse type [23, 200]. However, particularly strong immunostaining for Piccolo can be seen in the molecular layer of the cerebellum (Figure 9) [23, 200], where immunoperoxidase labelling beautifully demonstrates the presence of Piccolo in the ML (Figure 9A and C), as well as at synapses between PFs and PC spines (Figure 9D, asterisks) and the multiple active zones of MF terminals in the granule cell layer (Figure 9E and F).

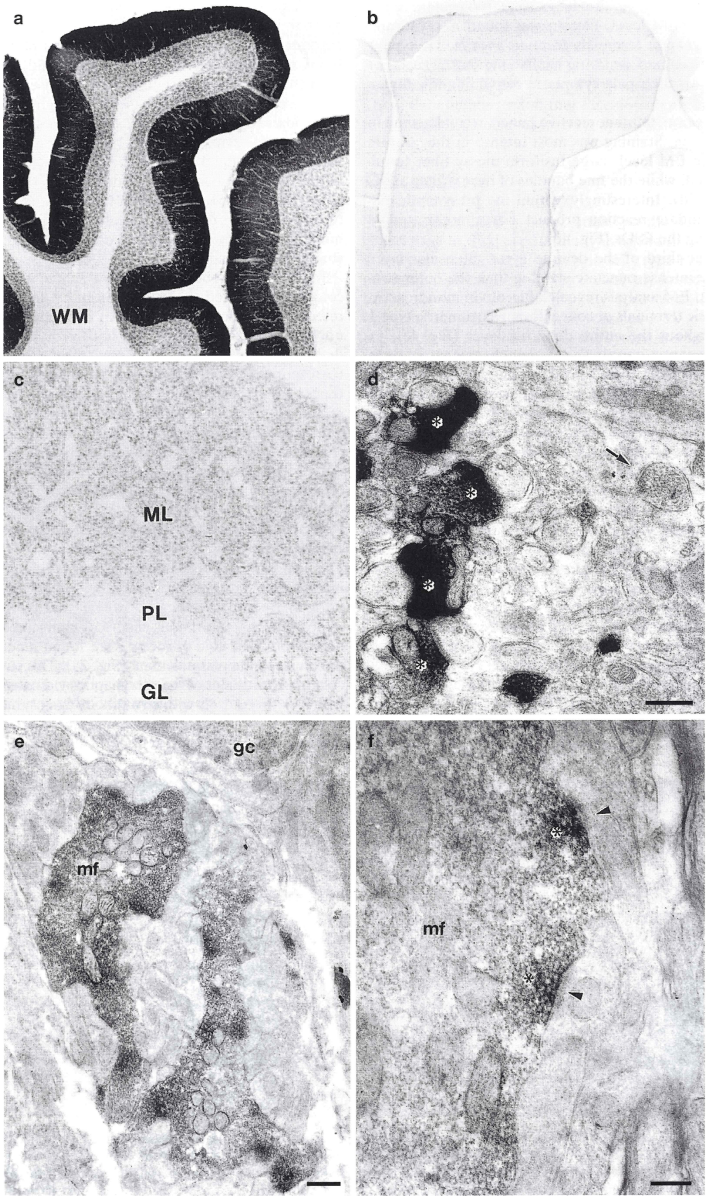

Figure 9: Piccolo localisation in the rat cerebellum

A, B) Sagittal cerebellar section stained with antibodies against Piccolo (A) or negative control (B) reveals strong Piccolo protein expression in the ML and punctate expression in the GCL (WM = white matter tracts). C) Semithin section demonstrates that the pattern of staining observed in the ML resembles the outline of PC and ML interneurone dendrites and somata. D) Electron microscopy analysis demonstrates the expression of Piccolo (horseradish peroxidase (HRP) reaction product) at most (asterisks) but not all (arrow) of PF-PC synapses. E, F) low (E) and high (F) magnification electron microscopy images of MF glomeruli in the GCL. MF terminals filled with SVs stain positive for Piccolo (HRP) concentrated at synaptic junctions (asterisks), opposing postsynaptic densities (arrowheads). Scale bars = 0.6 nm in D, E; 0.25 nm in F. Adapted from Cases-Langhoff et al. [23].

From loss of function and subcellular localisation studies, Piccolo appears to play a role in the SV cycle and the formation of new synapses. What remains unclear is how Piccolo contributes to cerebellar development and whether, as suggested by genetic studies, it has a primary role in the aetiology of PCH3. The recent generation of a Piccolo knockout rat (*Pclo*$^{gt/gt}$) using transposon mutagenesis [116] provides an excellent opportunity to explore this potential relationship.

4. Aim of the study

I sought to elucidate the role of Piccolo in the aetiology of PCH3 by two approaches: firstly, I aimed to compare the *Pclo*$^{gt/gt}$ rat model to PCH3 pathology at the anatomical and behavioural levels, in order to determine if the *Pclo*$^{gt/gt}$ rat could serve as a model to study this disease further. Secondly, I aimed to use the *Pclo*$^{gt/gt}$ model to investigate on a more detailed level the role of the Piccolo protein on the most severely affected regions in PCH3 patients, the cerebellum and the pons. Specifically, I wanted to investigate the synapses involved in the cerebellar networks underpinning the behavioural features observed in patients with PCH3.

On a general level, I was interested to find out the effect of inactivating such a large and multi-functional protein on the brain and how this could therefore affect behaviour.

5. Materials and Methods

5.1 Animals

5.1.1 Animal welfare

Animals of both sexes were used in experiments. All animals were treated and cared for in accordance with national and institutional guidelines:

Generation of mutant Piccolo rat strains and behavioural experiments: Rat protocols were approved by the Institutional Animal Care and Use Committee (IACUC) at UT-Southwestern Medical Centre in Dallas, as certified by the Association for Assessment and Accreditation of Laboratory Animal Care International (AALAC), permit number: NIH OLAW Assurance # D16-00296.

Western blotting, histology, cell culture, immunocytochemistry, electron microscopy and behavioural experiments with OptiMan setup: Animals were treated in accordance with the German Protection of Animals Act (TierSchG §4 Abs. 3); all procedures for experiments involving animals were approved by the animal welfare committee of Charité Medical University and the Berlin state government, permit number: T 0036/14.

Electrophysiology: Animals were treated in accordance with the German Protection of Animals Act (TierSchG §4 Abs. 3) and with the guidelines for the welfare of experimental animals issued by the European Communities Council Directive of 24. November 1986 (86/609/EEC). The local authorities approved the experiments (Landesdirektion Leipzig), permit number: T24/18.

5.1.2 Generation of Piccolo knockout rats (*Pclo*$^{gt/gt}$)

Mutant rat strains harboured Sleeping Beauty β-Geo trap transposons [88], originally transmitted from a donor, recombinant rat spermatogonial stem cell library [89]. Recipient males were bred with wildtype females to produce a random panel of mutant rat strains enriched with genetraps in protein coding genes [89].

5.1.3 Characterisation of pups and genotyping

P0-P2 rats, brains of P0-P2 rats and brains of 3-month rats were weighed using a Kern 440-43N scale; pups were measured for approximate length with a ruler. Pup brains were later extracted and weighed, genotyping of cortices revealed their genetic identity. P0-P2 pups were genotyped using a PCR based reaction. In brief, brain tissue was digested in lysis buffer (100 mM Tris-HCl (pH 8.0), 100 mM NaCl (Roth, Karlsruhe, Germany) with 10 mg/ml Proteinase K (Qiagen, Hilden, Germany)) for 5 min at 55 °C, before inhibiting Proteinase K by incubation at 99 °C for 10 min. Samples were centrifuged at 14,800 rpm for 2 min and 1 µl of supernatant was used for the PCR reaction as outlined below.

For determination of genotype for adult rats, earpieces were digested overnight (ON) at 55 °C in SNET-buffer (400 mM NaCl, 1 % SDS, 200 mM Tris (pH 8.0) (Roth, Karlsruhe, Germany), 5 mM EDTA (Sigma-Aldrich, Missouri, USA) containing 10 mg/ml Proteinase K. Proteinase K enzyme reaction was stopped by incubating the samples for 10 min at 99 °C. The mixture was centrifuged for 2 min at 14,800 rpm. Supernatant was transferred into a fresh tube and DNA was precipitated by addition of 100 % isopropanol (Roth, Karlsruhe, Germany). Following samples were centrifuged for 15 min at 4 °C, 13,000 rpm. Precipitated DNA was washed once with 70 % ethanol (EtOH) (Roth, Karlsruhe, Germany, diluted as appropriate with double distilled water (ddH_2O)) and centrifuged again for 5 min at 13,000 rpm. Supernatant was discarded and the DNA pellet was air dried and resuspended in sterile H_2O (Roth, Karlsruhe, Germany). A PCR reaction with a specific primer combination was performed on isolated DNA. The following primers were used: Pclo KO F2: 3` gcaggaacacaaaccaacaa 5`; Pclo KO R1: 3` tgacctttagccggaactgt 5`; SBF2: 3` tcatcaaggaaaccctggac 5` (Eurofins Genomics, Ebersberg, Germany). The PCR reaction protocol was the following: 2 min 94 °C; 3 x (30 s 94 °C, 60 °C 30 s, 72 °C 30 s); 35 x (94 °C 30 s, 55 °C 30 s, 72 °C 30 s); 72 °C 10 min. Samples were mixed with a loading dye (New England BioLabs, Massachusetts, USA) and run on 2 % agarose gel (Serva, Heidelberg, Germany) at 110 V for 45 min. The gel was imaged using BioDocAnalyze UV transilluminator and BioDocAnalyze2.2 software (Biometra, Göttingen, Germany).

5.2 Western blot analysis

Brains from P0-P2 pups were lysed in Lysis buffer (50 mM Tris-HCl, 150 mM NaCl, 1 % Triton X-100, 0.5 % Deoxycholate, protease inhibitor pH 7.5 (all reagents from Roth, Karlsruhe, Germany), 5 mM EDTA) and incubated on ice for 5 min. Samples were centrifuged at 13,000 rpm for 10 min at 4 °C. The supernatant was transferred into a fresh tube and the protein concentration was determined using a BCA protein assay kit (Thermo Fisher scientific, Massachusetts, USA). The same protein amounts for $Pclo^{wt/wt}$, $Pclo^{wt/gt}$ and $Pclo^{gt/gt}$ samples were separated by SDS-PAGE then transferred onto nitrocellulose membranes (running buffer: 25 mM Tris, 190 mM Glycine, 0.1 % SDS, pH 8.3; transfer buffer: 25 mM Tris, 192 mM Glycine, 1 % SDS, 7 % Methanol, pH 8.3). After the transfer, nitrocellulose membranes were blocked with 5 % milk in TBST (20 mM Tris pH 7.5, 150 mM NaCl, (all reagents from Roth, Karlsruhe, Germany) 0.1 % Tween 20 (Santa Cruz Cruz Biotechnology, Texas USA) and incubated with primary antibodies in 3 % milk (Roth Karlsruhe, Germany) in TBST ON at 4 °C. Nitrocellulose membranes were washed 3 times for 10 min with TBST and incubated with HRP-conjugated secondary antibodies for 1 h at room temperature (RT). Membranes were washed 3 times for 10 min with TBST; afterwards secondary antibody binding was detected with ECL Western Blotting Detection Reagents (Thermo Fisher Scientific, Massachusetts, USA) and a Fusion FX7 image and analytics system (Vilber Lourmat, Collégien, France) (for antibodies see Table 2). To visualise the amount of loaded protein, a coomassie staining was performed: the gel was washed 3 x in ddH_2O then stained with Imperial protein stain (Thermo Fisher Scientific Massachusetts, USA) for 2 hours at RT

with gentle agitation. Gel was then rinsed in ddH_2O several times until the gel was fully de-stained and imaged with the same image analytics system used for western blotting.

5.3 Histology

5.3.1 Fixation and preparation of tissue

5.3.1.1 Fixation for immunofluorescence, immunoperoxidase and Nissl staining

Rats were deeply anesthetised with Isoflurane (Abbott GmbH and Co. KG, Wiesbaden, Germany) before intraperitoneal (IP) injection with mix of 20 mg/ml Xylavet (CO-pharma, Burgdorf, Germany) and 100 mg/ml Ketamin (Inresa Arzneimittel GmbH, Freiburg, Germany) in 0.9 % NaCl (B/BRAUN, Melsungen, Germany), then perfused transcardially to exchange blood for warmed phosphate buffered saline (PBS) (Gibco Thermo Fisher Scientific, Massachusetts, USA), followed by 4 % paraformaldehyde (Roth, Karlsruhe, Germany) dissolved in PB (80 mM Na_2HPO_4 (Roth, Karlsruhe, Germany), 20 mM NaH_2PO_4 (Bernd Kraft, Duisburg, Germany)) (PFA). A tissue sample was taken for genotyping; brains were extracted and placed in 4 % PFA overnight, cryoprotected in 15 % and then 30 % sucrose solution (Sigma-Aldrich, Missouri, USA; dissolved in PB) for 24 hours each. Brains were frozen by submersion in -60 °C 2-methylbutane (Roth, Karlsruhe, Germany) and then stored at -20 °C until use.

5.3.1.2 Fixation for immunofluorescence staining of pre- and postsynaptic proteins

Rats were deeply anaesthetised with Isoflurane and decapitated with a guillotine. A tissue sample was taken for genotyping; brains were extracted, dissected into tissue slabs and submerged in PFA for 40 min then washed 3 x 5 min with ice cold PBS, cryoprotected and frozen as described above [156].

5.3.1.3 Preparation for Golgi staining

Rats were deeply anaesthetised with Isoflurane and decapitated with a guillotine. A tissue sample was taken for genotyping; brains were extracted, rinsed in ddH_2O and then placed into a Falcon tube containing impregnation solution (equal parts solutions A and B from the FD Rapid Golgi Stain kit (FD Neuro Technologies Inc., Maryland, USA)) ON under a chemical fume hood, protected from light using aluminium foil. Impregnation solution was exchanged for fresh solution and brains were then left for 20 days at RT under the fume hood, gently swirled every 2-3 days. Brains were transferred to fresh Falcon tubes containing cryoprotectant solution C from the FD Rapid Golgi Stain kit and incubated ON at 4 °C in the dark; the solution was then changed for fresh solution C and brains were

incubated for 4-5 days in the dark at 4 °C. Brains were then frozen as described above and stored protected from light at -80 °C until sectioning.

5.3.1.4 Tissue sectioning

Fixed/prepared brains were mounted onto a specimen chuck with Tissue freezing medium (Leica, Wetzlar, Germany), cut parasagittally or coronally using a Leica cryostat (Wetzlar, Germany) to obtain either 20 µm tissue sections, mounted on superfrost slides (Thermo Fisher Scientific, Massachusetts, USA) and left to dry for a 1 hour before storage at -20 °C (immunofluorescence and immunoperoxidase) or 60 µm tissue sections, mounted onto gelatine-coated slides and left to dry for 3 days before Golgi staining. Gelatine-coated slides were coated washing in 10 % Meister Proper (Procter & Gamble, Ohio, USA) and coating with 1.5 % Gelatine (Roth, Karlsruhe, Germany) in 3.52 mM potassium chromium sulphate 12-hydrate (Sigma-Aldrich, Missouri, USA), 30 % EtOH (Roth, Karlsruhe, Germany), 7 % glacial acetic acid (Th. Geyer, Renningen, Germany) in ddH_2O for 2-5 min. For free-floating staining either 50 µm (Nissl 3 months/post fixation method) or 35 µm (Nissl P2) sections were stored in antifreeze solution (30 % Ethylene glycol, 30 % Glycerol (Roth, Karlsruhe, Germany), 30 % ddH_2O, 10 % 0.244M PO_4 buffer (NaOH, NaH_2PO_4, Roth, Karlsruhe, Germany)) at -20°C.

5.3.2 Immunostaining

Prior to staining, at least 4 slides (each containing two sections) from each animal were left to equilibrate at RT for 1 hour. Sections were selected to encompass the range of the axis under investigation. A hydrophobic barrier was created around sections using a DAKO pen (DAKO, Glostrup, Denmark) and sections were washed and permeabilised with TBS (20 mM Tris pH 7.5, 150 mM NaCl) with 0.025 % Triton X-100 (all reagents from Roth, Karlsruhe, Germany) (TBST) or PBS with 0.1% Tween-20 (Santa Cruz Biotechnology, Texas USA) (PBST) for free-floating sections for 3 x 5 min, prior to blocking with 10 % Normal Goat Serum (NGS) with 1 % Bovine Serum Albumin (BSA) (both from Sigma-Aldrich, Missouri, USA) in TBS, or 10 % NGS in PBS for free-floating sections for 1 hour.

For immunofluorescence experiments, antibodies (Table 2) diluted in TBS with 1 % BSA or 5 % NGS in PBST (antibody solution) for free-floating sections were applied and left ON at 4 °C. After 3 x 10 min washing with TBST/PBST, differently labelled fluorescent secondary antibodies in respective antibody solution were applied for 1 hour at RT. Sections were then washed with TBS/PBS 2 x 10 min or, if desired, incubated in TBS/PBS with DAPI (1:1000, Roth, Karlsruhe, Germany) for 30 min before washing again 2 x 10 min. Slides were coverslipped with Immu-Mount or mounted onto slides with ProLong Diamond Antifade Mountant (all from Thermo Fisher Scientific, Massachusetts, USA) and sealed with clear nail polish once hardened.

For immunoperoxidase experiments, primary antibodies were diluted with antibody solution and incubated for 30 min at RT, washed for 5 min in TBST and then incubated in prepared VECTASTAIN ABC reagent (Vector laboratories, California, USA). HRP-conjugated secondary antibodies were incubated for 30 min at RT, then washed 5 min in TBS with DAB peroxidase-substrate (Vector laboratories, California, USA) until the stain developed. Slides were then rinsed in tap water, dehydrated through 50 %, 70 %, 95 % and 100 % EtOH before clearing in Roti Histol (Roth, Karlsruhe, Germany), coverslipped using Entellan mounting medium (Entellan, Darmstadt, Germany) and left to dry for 24 hours under a fume hood.

Antibody/stain	Species	Company/product code	Dilution
Calbindin	Rabbit	Synaptic Systems, Göttingen, Germany; Cat# 214002	1:750
$GABA_AR$ α6 subunit	Rabbit	Sigma-Aldrich, St. Louis, USA; Cat# G5544	1.250
GAP-43	Rabbit	Millipore Sigma, Burlington, USA, Cat# AB5220	1:750
Gephyrin	Mouse	Synaptic Systems, Göttingen, Germany; Cat# 147011	1:400
GFAP	Chicken	Millipore Sigma, Burlington, USA, Cat# AB5541	1:500
MAP2	Chicken	Millipore Sigma, Burlington, USA, Cat# AB5543	1:1000
Neuroligin 3	Rabbit	Synaptic Systems, Göttingen, Germany; Cat# 129103	1:300
Piccolo	Guinea pig	Synaptic Systems, Göttingen, Germany; Cat# 142 104	1:200
Piccolo (WB)	Rabbit	Synaptic Systems, Göttingen, Germany; Cat# 142002	1:1000
Tau	Guinea pig	Synaptic Systems, Göttingen, Germany; Cat# 314004	1:1000
VGAT	Rabbit	Synaptic Systems, Göttingen, Germany; Cat# 131003	1:500
VGluT1	Rabbit	Abcam, Cambridge, UK; Cat# ab104898	1:1000
VGluT2	Guinea pig	Synaptic Systems, Göttingen, Germany; Cat# 13540419	1:250
VGluT2	Mouse	Synaptic Systems, Göttingen, Germany; Cat# 135 421	1:300
Anti-chicken Alexa 647	Goat	Thermo Fisher Scientific, Waltham, USA; Cat# A21449	1:1000
Anti-rabbit HRP	Donkey	Sigma-Aldrich, St. Louis, USA; Cat# NA934	1:2500
Anti-rabbit Alexa 568	Goat	Thermo Fisher Scientific, Waltham, USA; Cat# A11036	1:1000
Anti-rabbit Alexa 488	Goat	Thermo Fisher Scientific, Waltham, USA; Cat# A11034	1:1000
Anti-mouse Alexa 568	Goat	Thermo Fisher Scientific, Waltham, USA; Cat# A11031	1:1000
Anti-mouse Alexa 488	Goat	Thermo Fisher Scientific, Waltham, USA; Cat# A11029	1:1000
Anti-guinea pig Alexa 488	Goat	Thermo Fisher Scientific, Waltham, USA; Cat# A11073	1:1000

Table 2: List of primary and secondary antibodies used in western blotting and immunostaining experiments

5.3.3 Nissl staining

Sections were washed 3 times in PBS, mounted onto superfrost slides and allowed to dry for 1-2 days. Slides were inserted into racks and passed through the following solutions: 95 % EtOH (Roth, Karlsruhe, Germany; diluted as appropriate with ddH_2O) for 15 min and 70 % EtOH, 50 % EtOH, ddH_2O for 1 minute each, blue counterstain (TACS from Trevigen, Maryland, USA) for 10 min, followed by a ddH_2O wash, dehydration, clearing and mounting as described above.

5.3.4 Golgi staining

Mounted slides were inserted into racks and passed through the following solutions: ddH_2O for 2 x 2 min, staining solution (FD Rapid Golgi Stain kit, FD Neuro Technologies Inc., Maryland, USA) for 30 seconds, 50 % EtOH, 75 % EtOH, 95 % EtOH, 4 x 99 % EtOH for 4 min each, Roti Histol for 3 x 4 min, then coverslipped and left to dry as described above.

5.4 Electron microscopy

Rats were anesthetised deeply with Isoflurane before IP with 20 mg/ml Xylavet and 100 mg/ml Ketamin in 0.9 % NaCl, then perfused transcardially, replacing blood with warmed PBS for 3 to 4 min followed by PFA and 0.05 % glutaraldehyde (Sigma-Aldrich, Missouri, USA). Brains were extracted, dissected and stored in fixative ON, washed with PBS, glued to a tissue chuck and sliced sagittally (350 µm) on a vibratome (Leica, Wetzlar, Germany) in ice cold PBS. Regions of interest were cut into small pieces and post-fixed in 1 % OsO_4 and 0.1 M sodium cacodylate (both from EMS, Pennsylvania, USA) and en-bloc stained in 1 % uranyl acetate aqueous solution (Merck, Darmstadt, Germany). Finally, samples were dehydrated and embedded in epoxy resin (Epon 812; EMS, Pennsylvania, USA). Ultrathin sections were cut using an Ultracut ultramicrotome (Leica, Wetzlar, Germany) equipped with a diamond knife (Ultra 45, DiATOME, Hatfield, USA) and collected on formvar-coated 200-mesh copper grids (EMS, Pennsylvania USA). Sections were imaged in a Zeiss EM-900 Transmission Electron Microscope (Zeiss, Oberkochen, Germany) operated at 80 keV and equipped with a 2K x 2K CCD camera (Olympus, Hamburg, Germany).

5.5 Cell culture

All cell culture preparations were performed in sterile conditions on a laminar flow clean bench and incubated at 37 °C in a humidified atmosphere with 5 % CO_2 and 95 % air HERAcell 150i CO_2 incubator (both from Thermo Fisher Scientific, Massachusetts, USA).

5.5.1 Pontine explant culture

P0-P1 pups from *Pclo*$^{wt/gt}$ breeding pairs were decapitated and pontine nuclei and cortices dissected in cold Hank's salt solution. Pontine nuclei were placed into prewarmed NBA and shaken at 37 °C, 750 rpm whilst genotyping result was obtained from cortices as described above (5.1.3). *Pclo*$^{wt/wt}$ and *Pclo*$^{gt/gt}$ pontine nuclei were dissected into ~100 µm^2 pieces and plated onto pre acid-washed, PLL (Poly-L-Lysine)- and Laminin (Sigma-Aldrich, Missouri, USA)- coated glass coverslips and incubated in NBA 37 °C, 5 % CO_2 for 24 hours or 3 days. For Wnt-7a experiments explants were treated with 50 ng/ml Wnt-7a for 24 hours before fixation with PFA, untreated explants served as control.

5.6 Immunocytochemistry

The following experiments were all conducted at RT. Dissociated neurones were fixed for 5 min and explants for 20 min with prewarmed 4 % PFA in PBS (Santa Cruz Biotechnology, Texas USA). Cells were permeabilised with PBST for 3 x 5 min with gentle shaking before blocking with 5 % NGS in PBST (blocking solution) for 1 hour. Primary antibodies (Table 2) diluted in blocking solution were incubated for 1 hour and then washed with PBST 1 x fast and 3 x 10 min. Secondary antibodies were diluted in blocking solution and incubated for 1 hour, then washed with PBS 1 x fast and 3 x 10 min. Coverslips were dipped into ddH_2O and mounted onto microscope slides using ProLong Diamond Antifade Mountant (both from Thermo Fisher Scientific, Massachusetts, USA).

5.7 Electrophysiology

5.7.1 Cerebellar slice recordings

Cerebellar slices were prepared from 3- to 4-month-old $Pclo^{wt/wt}$ and $Pclo^{gt/gt}$ rats. Animals were anesthetized with isoflurane (Baxter, Illinois, USA) followed by a rapid decapitation with a custom-built guillotine. The cerebellar vermis was quickly removed and mounted in a chamber filled with chilled extracellular solution. Parasagittal 300 µm slices were cut using a Leica VT1200 microtome (Leica, Wetzlar, Germany), transferred to an incubation chamber at ~35 °C for 30 min and subsequently stored at RT. Artificial cerebrospinal fluid (ACSF) was used for slice cutting, storage, and experiments. ACSF contained: 125 mM NaCl, 25 mM $NaHCO_3$, 2.5 mM KCl, 1.25 mM NaH_2PO_4, 1.1 mM $CaCl_2$, 1 mM $MgCl_2$, 3 mM Glucose, 17 mM Sucrose (~310 mOsm, pH 7.3 when bubbled with Carbogen (5 % O_2/95 % CO_2)). Patch pipettes were pulled from borosilicate glass (Science Products, Hofheim, Germany) using a DMZ Puller (Zeitz-Instruments, Martinsried, Germany). Patch pipettes had open-tip resistances of 6–9 MΩ. The intracellular solution contained: 150 mM K-gluconate, 10 mM NaCl, 10 mM K-HEPES, 3 mM Mg-ATP, 0.3 mM Na-GTP (300–305 mOsm, pH adjusted to 7.3 with KOH). In some of the experiments, the intracellular solution contained 10 µM of the fluorescence dye Atto594. Experiments were performed at 35–37 °C and slices were continuously perfused with ACSF containing 20 µM SR95531 and 40 µM D-(2R)-amino-5-phosphonovaleric acid (D-APV) to block Golgi-cell inhibition and NMDA-receptors, respectively. Atto594 was obtained from Atto-Tec (Atto-Tec, Siegen, Germany); all other chemicals were purchased from Sigma-Aldrich (Missouri, USA). Due to obvious differences in cerebellar size, it was not possible to blind the experimenter during slice recordings.

5.7.2 Current clamp recordings

To determine the input resistance, subthreshold current pulses were applied from -20 to +20 pA in 2 pA steps. Action potentials were evoked in current-clamp mode by current pulses (amplitude 20-400

pA, duration 300 ms). The access resistance was 24.9 ± 1 MΩ and 23 ± 1 MΩ for *Pclo*$^{wt/wt}$ and *Pclo*$^{gt/gt}$ rats respectively. Patch-clamp recordings were made using a HEKA EPC10/2 USB amplifier (HEKA Elektronik, Lambrecht/Pfalz, Germany). Data were sampled at 200 kHz. Measurements were corrected for a liquid junction potential of +16 mV.

The current clamp data were analysed using custom-made procedures in Igor Pro software (WaveMetrics, Oregon, USA) as described previously [45]. In short, properties of action potentials of GCs were determined from the injected currents that elicited the largest number of APs. The AP threshold was defined as the membrane voltage at which the first derivative exceeded 100 V s^{-1}, the minimal AP peak was set as -20 mV and the minimal amplitude to 20 mV. All APs with a half-width smaller than 50 µs and higher than 500 µs were excluded. AP frequency and AP half-width were calculated from the first three APs. Membrane capacitance, resting membrane potential and series resistance were read from the amplifier software (HEKA) after achieving the whole-cell configuration. Input resistance (R_{in}) was analysed by plotting the steady-state voltage elicited by the subthreshold current injections against the injected current and a spline interpolation was performed to obtain the slope at the holding membrane potential (0 pA current injection).

5.7.3 Excitatory postsynaptic currents

To measure evoked excitatory postsynaptic currents (EPSCs), GCs were held at a holding potential of -80 mV and MF axons were stimulated at 1 Hz. The stimulation voltage ranged between 16 to 40 V for control and *Pclo*$^{gt/gt}$ animals. For spontaneous EPSCs, GCs were held at -80 mV for around 3 min. Single events were detected using the Igor Pro extension NeuroMatic [146] tool for event detection. Tetrodotoxin (TTX) was not used to prevent spontaneous MF action potentials, as the somata of MF axons are located outside of the cerebellum. As no hillock is present in the slice preparation, no spontaneous action potentials can be initiated.

EPSCs were analysed with the Igor Pro software. The amplitude and the kinetics were determined from the average of 25 individual single EPSCs. To obtain the decay kinetics, single EPSCs were fitted with one or two exponentials. The weighted time constant was calculated as:

$$\tau w = \frac{Aslow\ \tau slow\ +\ Afast\ \tau fast}{Aslow\ +\ Afast}$$

5.8 Image acquisition and quantification

5.8.1 Confocal Z-stack and brightfield image acquisition

Images were acquired on a spinning disc confocal microscope (Zeiss Axio Observer.Z1 with an Andor spinning disc and cobalt, omicron, I-beam laser) (Zeiss, Oberkochen, Germany) using a 20x (0.8 NA) 40x (1.3 NA) or 100x (1.4 NA) Plan-Apochromat oil objective and an iXon ultra (Andor, Belfast, UK) camera controlled by iQ software (Andor, Belfast, UK). The same microscope and software were used with a brightfield setup to image Golgi, Nissl and DAB-stained sections using a Zyla-4.2 sCMOS camera and 5x (0.16 NA) or 10x (0.45 NA) objectives. Sections for $GABA_A\alpha6$ analysis were imaged with a Nikon Spinning Disk Confocal CSU-X using a 100x (1.45 NA) Plan Apochromat oil objective and an EMCCD camera with Andor Revolution SD System (Andor, Belfast, UK), controlled using Nikon Imaging Software (Nikon, Leuven, Belgium).

5.8.2 Tile scan overview images

An upright microscope (Olympus BX61, Hamburg, Germany) with a magnesium lamp (X-cite series 120Q from Excelitas technologies, Ontario, Canada) or brightfield was used to image fluorescently labelled cerebellar or Nissl stained whole-brain sections. A CCD colour or monochrome camera (Q Imaging, British Columbia, Canada) was used with a 2x (0.06 NA) or 10x (0.3 NA) objective for overview pictures. CellSens software (Olympus, Hamburg, Germany) stitched multiple images together to give an overview of the whole region.

5.8.3 Image analysis

For image processing and analysis ImageJ/FIJI software was used [153]. For analysis of $Pclo^{wt/wt}$ and $Pclo^{gt/gt}$ tissue, sections were selected from the vermis and approximately every 10th slide laterally (each slide containing 2 sections) was analysed. The best quality section per slide was imaged. For layer thickness, all lobes were measured and for closer analysis of MF size, CF coverage and GC density, images were taken from lobes I, III, V, VII and IX where possible.

Layer “thickness” was calculated per lobe by dividing the area of the layer by the inner length of the layer for both GCL and ML, referred to as thickness hereinafter. For Purkinje cell density, the number of PCs per lobe was counted and divided by the length of the PC layer for that lobe. Data points represent thickness values from individual lobes.

Granule cell density was calculated from 100x magnification image stacks stained with DAPI. GCs were counted according to [115] using the unbiased optical dissector method, where 3D tissue can be quantified by dividing it into multiple 2D sections (focus planes of a confocal Z-stack). Each section is then assessed and only the cells that exist in their entirety within the tissue slice, not cut at

the edges or at the top or bottom of the slice can be counted. This method removes confounding factors such as shape and orientation of the cells from the analysis. The experimenter was also blinded to the genotype of each image.

MF cluster size was measured using a script within ImageJ to analyse particles stained with vesicular glutamate transporter 1 (VGluT1) and/or vesicular glutamate transporter 2 (VGluT2). The area of each puncta was measured; data points represent average cluster size of each animal. Climbing fibre innervation was assessed using VGluT2 and Calbindin staining. The molecular layer area was defined in the Calbindin channel, consisting of Calbindin positive PC dendrites, and the VGluT2 channel was selected and pasted into a new ImageJ file. The same script as for MF analysis was run to calculate the total area stained with VGluT2, divided by the area of the ML and x100 to give percentage coverage.

For $GABA_A\alpha6$ subunit expression, average signal intensity was measured for the whole field of view in the $GABA_A\alpha6$ antibody channel and then normalized to the MAP2 channel for each image. Golgi-stained hippocampal pyramidal cells were reconstructed using Neurolucida software (MBF Bioscience, Vermont, USA) using an upright microscope (Olympus BX61) with a 40x objective (0.75 NA) and a CCD colour camera (MBF Bioscience, Vermont, USA).

Electron microscopy (EM) data, β-catenin quantification and pontine explant growth cone images were also analysed using ImageJ. A P2A value for complexity (Hall et al., 2000) was calculated by perimeter^2/area of MF glomerulus (EM) or growth cone (explant). β-catenin intensity was measured in the nucleus - as determined by DAPI staining - in one plane of a Z-stack through the centre of the nucleus and then normalised to the signal from the DAPI channel.

Due to the severity of the genotype, it was not possible to blind the experimenter when acquiring images from brain sections and for some of the analysis. However, analysis of GC density was conducted blind; MF and CF analysis were conducted using an ImageJ script (therefore immune to experimenter bias). EM data were analysed blindly, however, as the MF phenotype was also detectible at the ultrastructural level, it was not possible to be completely blinded. For immunocytochemistry (ICC), image acquisition and analysis was performed blinded to the genotype/ treatment condition.

5.9 Behavioural assessment

5.9.1 Rotarod task

The apparatus (IITC Life Science, California, USA) consisted of 5 semi-enclosed lanes and an elevated metal rod (9.525 cm diameter, 29.21 cm elevation) with a fine textured finish to enhance grip. For each trial, all rats were placed on the unmoving rod, allowed to stabilise their posture, and then rod rotation was initiated. Test parameters were: rotation direction, toward investigator to encourage rats to face away while walking; start speed, 4 rpm; top speed, 44 rpm; acceleration rate, 0.2 rpm/s (200 s

from start to top speed); max test duration, 300 s. Each rat's trial ended when it fell from the rod, triggering the fall-detection sensor. Data was automatically recorded to a computer. Rats underwent 4 trials/day, with an inter-trial interval of at least 10 min for 4 consecutive days.

5.9.2 Ladder rung task

Ladder rung tests were performed on cohorts of *Pclo*$^{wt/wt}$, Pclo$^{wt/gt}$ and *Pclo*$^{gt/gt}$ rats by methods previously described [119]. Rats were trained to cross a plexiglass tunnel about 1 m long with metal rods provided at regular intervals as steps. Each step that the rat took was scored on the basis of paw placement on a 7 category scale with 0 being paw totally missing the rung and 6 being correct paw placement. The average score per pair of limbs was used to quantify step score. During the trial, the error per step was also quantified by number of low scoring steps (0-2) divided by the total number of steps that the rat took during the test with each pair of limbs. Data were derived from 3 trials with 3 cm rung separation conducted on the same test day with at least a 10 min inter-trial interval, and group means were compared.

5.9.3 Grip test

To assess grip strength, rats were allowed to cling on to a support by forelimbs or hindlimbs and pulled [34]. The support is attached to a transducer that can measure the pull force being applied on the rat by the tester. During each trial, force that was necessary to be applied by the tester to release the grip of the rat was recorded. Three trials per limb pair were done and the means compared. To assess grip strength, the rat's torso was supported ventrally while both forelimbs were allowed to grasp a metal support bar, then the rat was pulled in a horizontal plane until the bar was released. Peak force was measured by a transducer attached to the support bar (San Diego Instruments, San Diego, USA). Nine trials per rat were conducted over two days (inter-trial interval at least 5 min) and group means were compared.

5.9.4 Open field test

The open field test [34] was performed for each rat using a rectangular arena (91.44 cm x 60.96 cm) divided into 9 equal sectors (1 centre, 8 perimeter). At the start of the experiment, the rat was placed in the centre sector and allowed to explore for 10 min. The test was recorded by digital video for later analysis. One test was conducted per rat. The behaviours counted were crossing, rearing and grooming. Each crossing event was counted when all four limbs of the test subject crossed the boundary of one sector into another. Rearing was defined as the number of times the subject stood up on its hind limbs. Grooming was defined as the number of times a rat licked or scratched itself while remaining stationary. Events that occurred in the centre versus perimeter sectors were tallied separately, and group means were analysed for each region.

During the above experiments, the experimenter was blinded to the genotype of the animals during data acquisition and analysis.

5.9.5 OptiMan system

Four groups of *Pclo*$^{wt/wt}$, *Pclo*$^{wt/gt}$ and *Pclo*$^{gt/gt}$ rats were used in this study. Rats carried subcutaneous radio-frequency identification (RFID) tags in ventral location. Animals were group-housed with 6 - 8 rats per group. Initially, all rats were habituated to the Operator Independent Motor-Analysis, PhenoSys (OptiMan) multi-cage environment with open sorter gates for voluntary exploration. Then, automated sorting was activated so that only one rat could enter the operant chamber at a time. During pull-task training, force thresholds and handle positions were adapted every day for each session to the current skill level reached by a rat. Each session had 20 trials, and two to three individual sessions were given per day with an intersession interval of 30 to 60 min. Within a session, the maximum time interval a rat was allowed to remain inactive between trials was 6 - 8 min. A session ended when such inactivity occurred. The OptiMan (system consists of two interconnected group home cages (EU Type IV cage and 2000P) resting on an RFID sensor array plate that automatically tracks RFID tag movement within the cage, and thus the locomotor activity of individual rats, day and night. One of the home cages was connected via an electronic guillotine gate to a second cage. From this compartment, an animal entered a cage containing the isometric pull-task.

5.9.6 Isometric pull task

Rats were trained to pull a handle attached to a stationary force transducer with a predetermined force threshold upon which they received a sugar pellet reward. Upon a rat's entry into the isometric pull task cage a sugar pellet was delivered into the reward tray. A session started when the rat retrieved this first reward, which led to the automatic closing of the entry gate, and to the motorised slide-in appearance of the force handle to its predefined position. During each session, 5 different handle positions were presented to a rat. These positions varied from 11 mm inside the cage wall (easiest position), to 7 mm outside of the cage wall (most difficult position). Handle positions changed automatically during a session through a motorised slide. The difficulty level within each handle position increased stepwise by increasing the force threshold for pellet release. This started at 30 g pull-force and was increased to 40 g, 50 g and finally 60 g. A trial started when a pull-force of 5 g was sensed. From then on, the pull-force was sampled for a duration of 4 s. If a rat reached the force threshold within a 2 s time interval then a trial was successful and a reward delivered. The schedule then advanced to the next level of difficulty by either increasing force threshold or moving the handle one position further towards the outside. Thus, a rat needed a minimum of 20 trials to complete a session with 5 different handle positions and 4 different force thresholds at each position. If the threshold was not reached, then a trial was considered unsuccessful and the rat had to continue with its

next trial with unchanged conditions. Experiments lasted for 15 experimental days with 2 - 3 daily sessions per individual.

Due to the automated setup, experimenter bias is greatly reduced. Nonetheless, the experimenter was also blinded to the genotype of the rats during training and test phases.

5.10 Experimental design and statistical analysis

GraphPad Prism (RRID:SCR_002798) was used to analyse and represent data. For all data, a normality test was performed (D'Agostino-Pearson omnibus normality test). If data proved to meet the conditions of normality, then a student's t-test was used to compare *Pclo*$^{wt/wt}$ to *Pclo*$^{gt/gt}$ rats, or alternatively a test for non-normal data (Mann-Whitney U test) was used. To compare multiple conditions, the appropriate ANOVA was performed. Statistical design, sample sizes and tests for each experiment can be found in the figure legends.

6. Results

6.1 Transposon mutagenesis removes most isoforms of the active zone protein Piccolo

In collaboration with Kent Hamra and colleagues, we have taken advantage of the sleeping beauty genetrap technique [88, 116] to generate a rat Piccolo knockout model. This transposon, inserted into exon 3 of the *PCLO* gene is predicted to cause a frame shift in the reading frame (Figure 10A) and thus disrupts the expression of full-length Piccolo (560 kDa) as well as most of its alternatively spliced lower molecular weight isoforms (70-350 kDa). Nonetheless, $Pclo^{wt/wt}$, $Pclo^{wt/gt}$ and $Pclo^{gt/gt}$ pups were born in normal Mendelian numbers (Figure 10B). To verify loss of Piccolo protein expression, we performed western blots and immunohistochemical analysis. In Western blots of rat brain lysates, we observed prominent bands between 70-520 kDa in $Pclo^{wt/wt}$ and $Pclo^{wt/gt}$ lanes. Nearly all of these were absent in $Pclo^{gt/gt}$ brain lysates (Figure 10C, left). A coomassie loading control demonstrates equal levels of protein between lanes on the SDS-PAGE gel (Figure 10C, right). Immunostaining of $Pclo^{gt/gt}$ cerebellar sections with antibodies against Piccolo reveals an absence of immnuofluorescence in the molecular and granule cell layers. This is in contrast to robust staining with antibodies against the excitatory presynaptic vesicle marker VGluT1. Note immunoreactivity for both Piccolo and VGluT1 antibodies in these layers is quite prominent in $Pclo^{wt/wt}$ sections (Figure 10D and E).

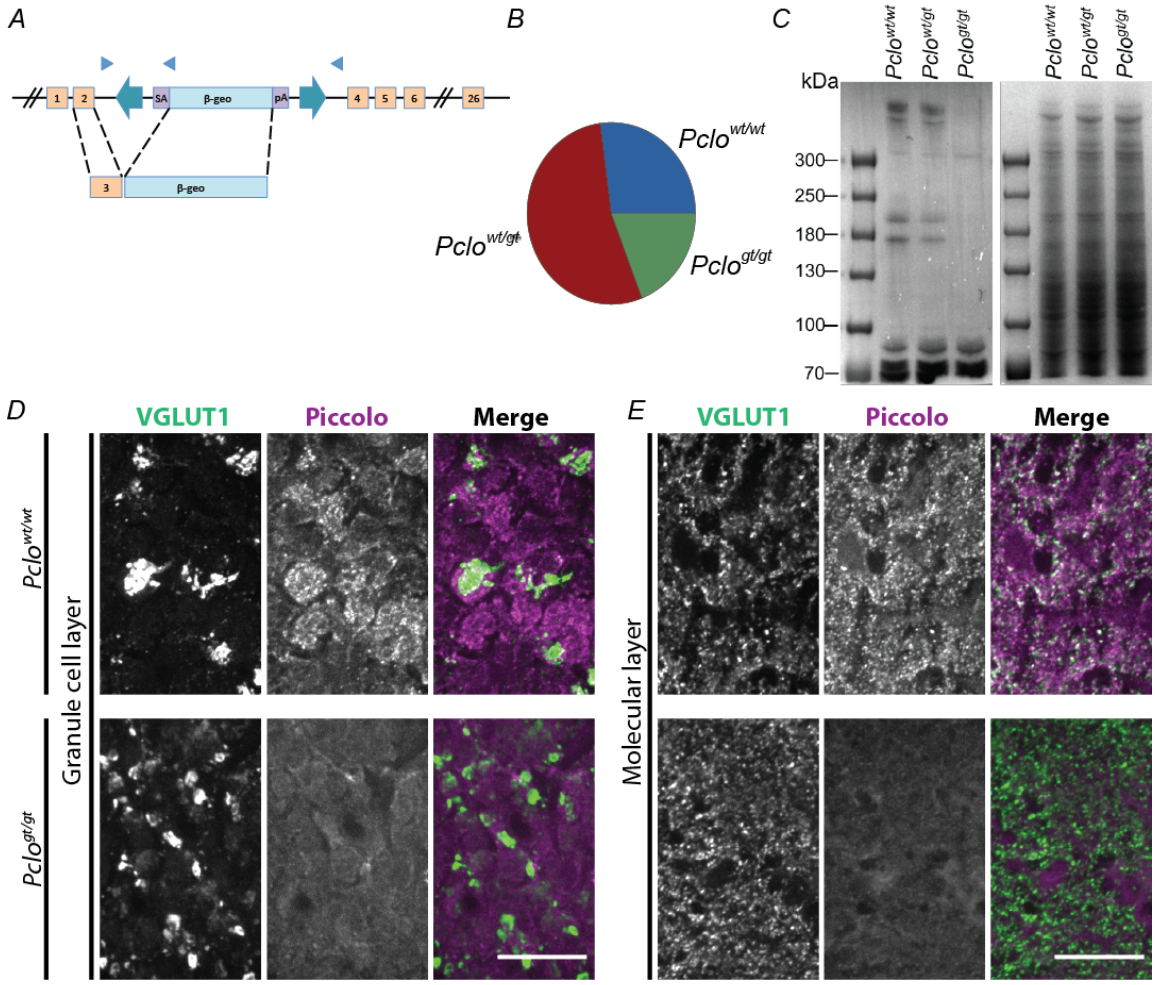

Figure 10: Genetrap mutagenesis of the Piccolo gene removes most isoforms of the active zone protein

A) Sleeping beauty transposon mutagenesis was used to generate genetrap Piccolo knockout rats. The transposon element was inserted into exon 3 of the *Pclo* genomic sequence and caused a stop in the reading frame. Adapted from Ackermann et al. [2]. B) Pairs of heterozygous ($Pclo^{wt/gt}$) males and females produced litters with Mendelian distribution. Pie chart demonstrates the birth rates of homozygous wildtype ($Pclo^{wt/wt}$), homozygous genetrap mutation ($Pclo^{gt/gt}$) and heterozygous ($Pclo^{wt/gt}$) pups (data collected from 63 litters: $Pclo^{wt/wt}$ = 195 pups; $Pclo^{wt/gt}$ = 387 pups; $Pclo^{gt/gt}$ = 137 pups). C) Left: western blot analysis of brain lysates prepared from P2 animals confirms the loss of full-length Piccolo protein from the brain. A band corresponding to the largest Piccolo isoform (~560 kDa) is detectable in lysates prepared from $Pclo^{wt/wt}$ and $Pclo^{wt/gt}$ animals. Also present are bands between 70-420 kDa representing smaller Piccolo isoforms. Nearly all of these are absent in $Pclo^{gt/gt}$ brain lysates (data are representative of 3 independent experiments), though smaller bands between 100 and 70 kDA are still present in $Pclo^{gt/gt}$ brain lysates. Right: coomassie blue stain of SDS-PAGE gel as a loading control. D, E) Images of sagittal sections of $Pclo^{wt/wt}$ and $Pclo^{gt/gt}$ cerebella at 3 months of age stained with antibodies against VGluT1 and Piccolo, demonstrating the loss of Piccolo in the ML (D) and the GCL (E) in $Pclo^{gt/gt}$ rats. Scale bars = 20 µm. Adapted from Falck et al. [46].

6.2 $Pclo^{gt/gt}$ pups are smaller at birth and as adults

In an initial characterisation of the $Pclo^{gt/gt}$ mutation, we assessed the length and weight of newborn litters. We found $Pclo^{gt/gt}$ pups to be smaller and lighter than their $Pclo^{wt/wt}$ littermates (mean length, weight: $Pclo^{wt/wt}$ = 5.50 cm, 8.09 g; $Pclo^{gt/gt}$ = 5.15 cm, 7.31 g) (Figure 11A-C), though there was no significant difference in their brain weights (Figure 11 D and E). At 3 months of age, however, $Pclo^{gt/gt}$

rats are still smaller than *Pclo*$^{wt/wt}$ (not shown) and *Pclo*$^{gt/gt}$ brains weigh 31.6 % less than *Pclo*$^{wt/wt}$ (Figure 11F), indicating that the loss of Piccolo causes several developmental phenotypes. A more detailed analysis of Nissl stained sections at birth and at 3 months of age revealed an overall reduction in brain size in older rats (Figure 11F-H), although not all regions seem to have the same attenuation of volume. Our qualitative assessment of brain architecture in sagittal sections (Figure 11H) showed a reduction in overall size in *Pclo*$^{gt/gt}$ animals, with an exaggerated loss of brain volume in areas such as the pons and the cerebellum. Furthermore, the ventricles in *Pclo*$^{gt/gt}$ appear much larger than in *Pclo*$^{wt/wt}$ brains, indicating further loss of brain matter.

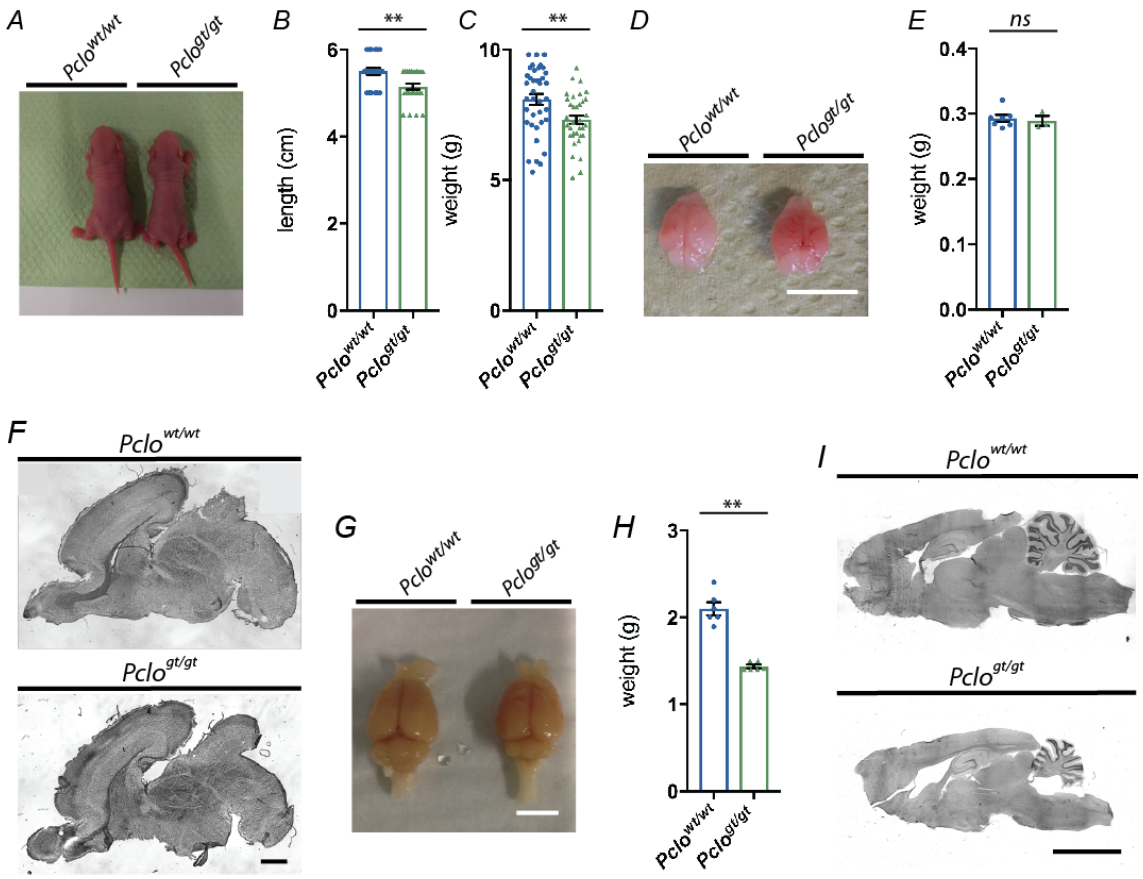

Figure 11: *Pclo*$^{gt/gt}$ animals are smaller at birth and have smaller brains as adults
A) Image of P1 *Pclo*$^{wt/wt}$ and *Pclo*$^{gt/gt}$ littermates. B, C) Quantification of the body length and weight of P0-P2 *Pclo*$^{wt/wt}$ and *Pclo*$^{gt/gt}$ pups (*Pclo*$^{wt/wt}$ = 8.09 g ± 0.203, n = 39; *Pclo*$^{gt/gt}$ = 7.31 g ± 0.166, n = 35; 12 independent litters; unpaired t-test (72) t = 2.937, p** = 0.0044). D) Image of brains dissected from P1 *Pclo*$^{wt/wt}$ and *Pclo*$^{gt/gt}$ pups. E) Quantification of the brain weight of P0-P2 *Pclo*$^{wt/wt}$ and *Pclo*$^{gt/gt}$ pups (*Pclo*$^{wt/wt}$ = 0.293 ± 0.00533, n = 7; *Pclo*$^{gt/gt}$ = 0.289 g ± 0.00758 n = 3; 3 independent litters; unpaired t-test (8) t = 0.423, p = 0.683) F) Nissl stained sagittal sections from P2 rat brains. No overt differences in size between *Pclo*$^{gt/gt}$ and *Pclo*$^{wt/wt}$ pups are seen. G) Image of 4 % PFA-perfused brains from *Pclo*$^{wt/wt}$ and *Pclo*$^{gt/gt}$ animals at 3 months of age. H) Quantification of the brain weight showing that *Pclo*$^{gt/gt}$ brains are significantly lighter than *Pclo*$^{wt/wt}$ brains (*Pclo*$^{wt/wt}$ = 2.098 g ± 0.074, *Pclo*$^{gt/gt}$ = 1.435 g ± 0.021; n = 6, Mann-Whitney U test, U = 0, p** = 0.0022). I) Nissl stained sagittal sections from 3-month-old rat brains reveal microcephaly in *Pclo*$^{gt/gt}$ compared to *Pclo*$^{wt/wt}$. Note ventricles are larger and cerebellum, pons, cerebrum and subcortical regions are smaller. Scale bars = 1 cm in D, G; 1 mm in F; 0.5 cm in I. Error bars represent SEM. Adapted from Falck et al. [46].

6.3 Piccolo loss of function affects brain anatomy and cell distribution

6.3.1 Pontine and cerebral volumes are reduced in *Pclo*$^{gt/gt}$ brains

As the brain regions most severely affected in PCH3 are the pons, cerebral cortex and the cerebellum [127, 137], and the initial examination of brain architecture using a Nissl stain indicated that these areas are also smaller in the *Pclo*$^{gt/gt}$ rat (Figure 11G), we decided to inspect these areas more closely.

As in the human PCH3 condition, the thickness of the cerebral cortex is less in *Pclo*$^{gt/gt}$ (mean thickness: *Pclo*$^{wt/wt}$ = 2.18 mm; *Pclo*$^{gt/gt}$ = 1.98 mm) (Figure 12A and B) and the pons is dramatically reduced in size. As the density of neurones in the pons was not changed (Figure 12C, zoom), these data indicate a loss of the total number of neurones within the pons. This conclusion is supported by data from brainstem sections stained with antibodies against the SV protein VGluT1, prominently expressed in pontine neurones, which reveals a 46.63 % smaller area occupied by these neurones (Figure 12D and E).

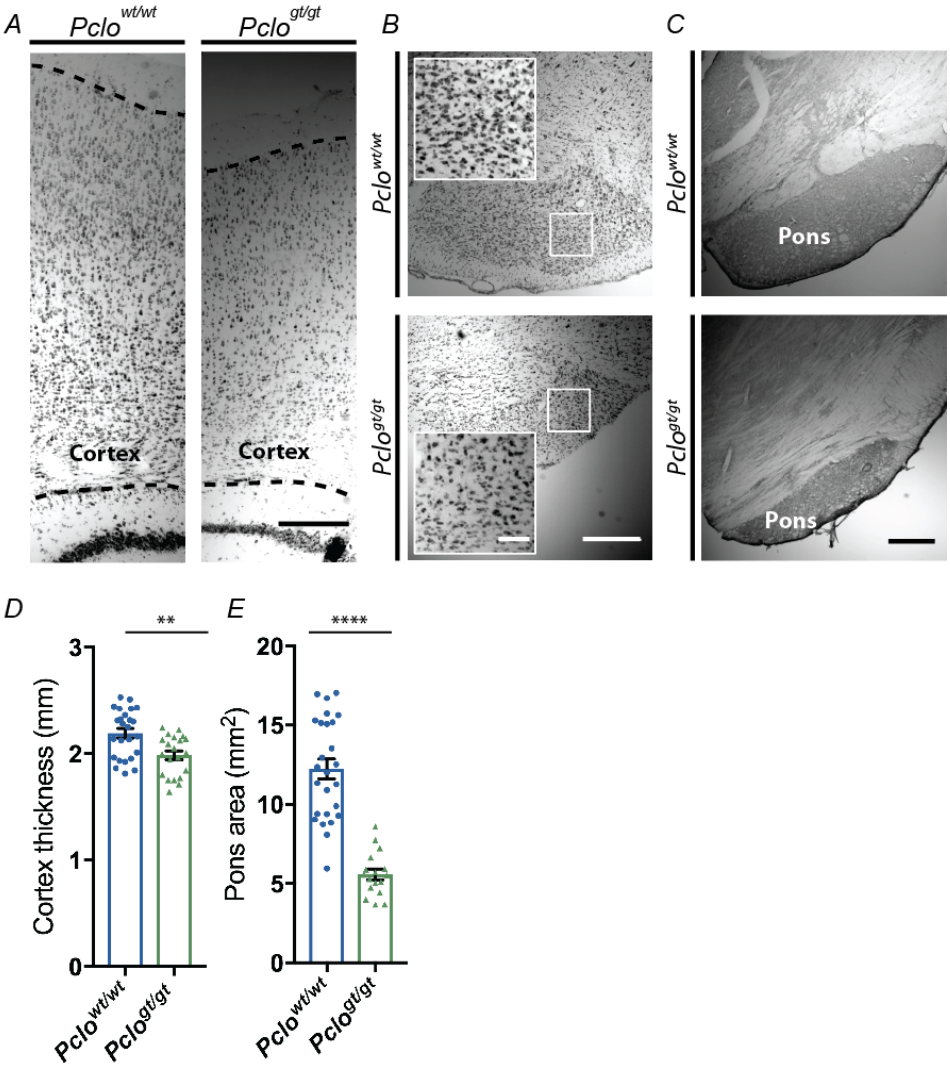

Figure 12: *Pclo*$^{gt/gt}$ rats show cortical thinning and a smaller pons area compared to *Pclo*$^{wt/wt}$

A, B) Nissl stained somatosensory cortex (indicated by dashed lines) (A) and the brainstem including pontine area (B) of *Pclo*$^{wt/wt}$ and *Pclo*$^{gt/gt}$ brains at 3 month of age. Zoom areas (B) demonstrate that pontine neurones are of similar density in *Pclo*$^{wt/wt}$ and *Pclo*$^{gt/gt}$. C) Pontine area visualized with antibodies against VGluT1 and subsequent immunoperoxidase conversion on *Pclo*$^{wt/wt}$ and *Pclo*$^{gt/gt}$ brains at 3 month of age. D) Quantification of the thickness of the somatosensory cortex (*Pclo*$^{wt/wt}$ = 2.18 mm ± 0.045, n = 25 brain sections; *Pclo*$^{gt/gt}$ = 1.98 mm ± 0.041, n = 21 brain sections; n = 3 independent experiments; unpaired t-test (44), $t = 3.323$, $p^{**} = 0.0018$). E) Quantification of the area of the pons (*Pclo*$^{wt/wt}$ = 12.24 mm^2 ± 0.620, n = 26 brain sections; *Pclo*$^{gt/gt}$ = 5.58 mm^2 ± 0.333, n = 17 brain sections; n = 3 independent experiments; unpaired t-test (41), $t = 8.164$, $p^{****} < 0.0001$). Scale bars = 200 µm in A, C: 500 µm in B, C: 100 µm in B (zoom). Error bars represent SEM. Adapted from Falck et al. [46].

6.3.2 Piccolo loss of function affects cerebellar layers and cell distribution

As the cerebellum is also severely reduced in size in both PCH3 patients and in *Pclo*$^{gt/gt}$ rats, we explored which sub-regions of the cerebellum were most affected. Analysis of sagittal sections through the cerebellum of 3-month adult rats reveals that, whilst the cerebellum is smaller in *Pclo*$^{gt/gt}$ animals, the overall anatomy is not altered (Figure 13A). For example, there are no remarkable defects in foliation of *Pclo*$^{gt/gt}$ animals, with all lobes present and appearing to be formed normally at the

vermis (Figure 13A and E). Our analysis of the GCL, using DAPI to stain GC nuclei, revealed that this layer is significantly reduced in size in *Pclo*$^{gt/gt}$ compared to *Pclo*$^{wt/wt}$ controls (mean GCL size: *Pclo*$^{wt/wt}$ = 200.8 µm; *Pclo*$^{gt/gt}$ = 134.8 µm) (Figure 13A and C). However, this decrease was not associated with a proportional increase in GC packing density, as the number of GCs per GCL area is unchanged (Figure 13B and D). These data indicate an overall loss of GCs in *Pclo*$^{gt/gt}$ cerebella. Conceptually, this is predicted to reduce the total number of GC parallel fibres innervating PC dendrites in the ML, a situation that could lead to a thinner ML and perhaps an altered packing density of PCs.

Sections immunostained with antibodies against Calbindin, which specifically labels PCs, support this concept. In particular, we find that the organization of the ML and the PCL appear to be intact and that the dendritic arbours of PCs are correctly orientated (Figure 13E, F and I). However, quantifying the average area per unit length of the ML reveals a 32.1 % reduction in the thickness of this layer in *Pclo*$^{gt/gt}$ brains (Figure 13G). Furthermore, cells in the PCL appear overcrowded in *Pclo*$^{gt/gt}$ cerebella (Figure 13E, F and I), a conclusion supported by data showing an increased packing density of PCs in *Pclo*$^{gt/gt}$ brains (Figure 13H).

Taken together, these data indicate smaller *Pclo*$^{gt/gt}$ cerebella are related to reduced numbers of GCs, thinner MLs and a higher packing density of PCs in *Pclo*$^{gt/gt}$ cerebella compared to *Pclo*$^{wt/wt}$ controls.

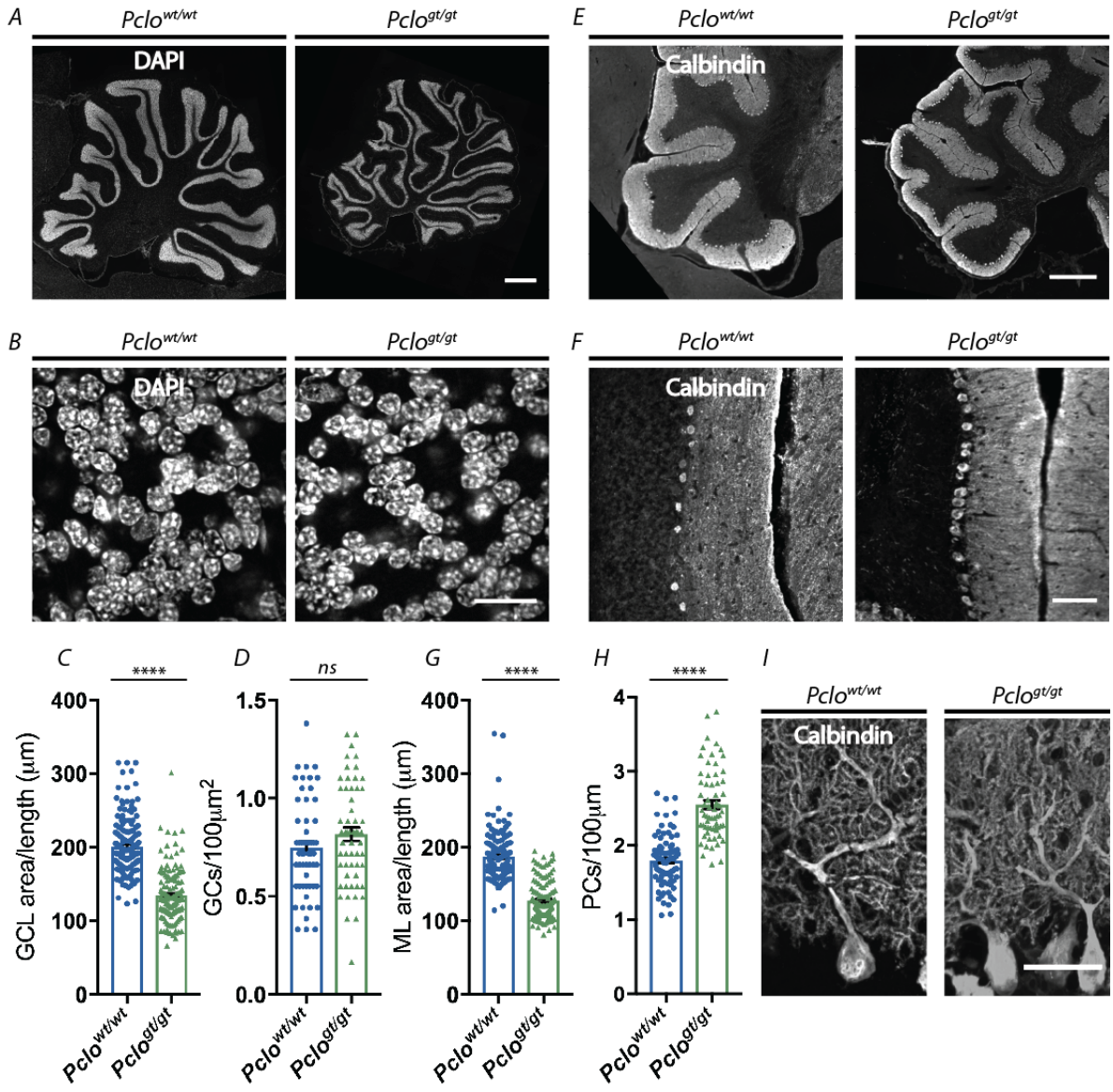

Figure 13: Morphometric comparison of *Pclo*$^{gt/gt}$ and *Pclo*$^{wt/wt}$ cerebella

A-D) Images of sagittal sections of *Pclo*$^{wt/wt}$ and *Pclo*$^{gt/gt}$ cerebella at 3 month of age. The densely packed granule cell layer was visualised by DAPI staining (A, B). B) Higher magnification images of (A) revealing normal GC density in the GCL of *Pclo*$^{wt/wt}$ and *Pclo*$^{gt/gt}$ cerebella. C) Quantification of the GCL thickness (*Pclo*$^{wt/wt}$ = 200.8 µm ± 2.932, n = 160 lobes; *Pclo*$^{gt/gt}$ = 134.8 µm ± 2.859, n = 148 lobes; n = 4 independent experiments; Mann-Whitney U test, U = 1953, p**** <0.0001). D) Quantification of the number of GCs per 100 µm^2 (*Pclo*$^{wt/wt}$ = 0.747 ± 0.326, n = 56 images from 3 rats; *Pclo*$^{gt/gt}$ = 0.817 ± 0.343, n = 57 images from 4 rats; unpaired t-test (111), t = 1.462, p = 0.147). E-H) Images of sagittal sections of *Pclo*$^{wt/wt}$ and *Pclo*$^{gt/gt}$ cerebella at 3 months of age stained with antibodies against Calbindin, a marker of PCs was used to define the molecular layer (lobes I-III shown). F) Higher magnification images of (E). Note the closer packing of PCs in *Pclo*$^{gt/gt}$ compared to *Pclo*$^{wt/wt}$. G) Quantification of the ML thickness (*Pclo*$^{wt/wt}$ = 187.2 µm ± 2.719, n = 148 lobes; *Pclo*$^{gt/gt}$ = 127.2 µm ± 2.378, n = 125 lobes; n = 4 independent experiments; Mann-Whitney U test, U = 1368, p**** < 0.0001). H) Quantification of the number of PCs per 100 µm length of PC layer (*Pclo*$^{wt/wt}$ = 1.797 ± 0.036; n = 89 lobes; *Pclo*$^{gt/gt}$ = 2.554 ± 0.058; n = 65 lobes; n = 3 independent experiments; unpaired t-test (152), t = 11.62, p**** < 0.0001). I) Images of sagittal sections stained with antibodies against Calbindin showing that PCs migrate correctly to their position in the ML and are correctly orientated. Scale bars = 1cm in A; 20 µm in B,; 50 µm in I; 200 µm in F. Error bars represent SEM. Data points represent images taken from all lobes; 4 sections per animal (B, D). Adapted from Falck et al. [46].

Because Bergmann glia cells of the cerebellum are essential for GC migration to the IGL [196] and we see an overall loss of GCs in the GCL, we examined the glial cells of the molecular layer by immunostaining for the Glial fibrillary acidic protein (GFAP), expressed by astrocytes. Bergmann glia cell bodies are located in the PCL and their radial fibres project out into the ML. These can be easily distinguished from Purkinje cell bodies and dendrites, visualised by immunostaining for Calbindin. In *Pclo*$^{gt/gt}$ sections, the Bergmann glia processes are noticeably closer together and more abundant in *Pclo*$^{gt/gt}$ cerebella. This is paralleled by the higher packing density of PC cell bodies in the PCL (Figure 14). No other discernible differences were observed.

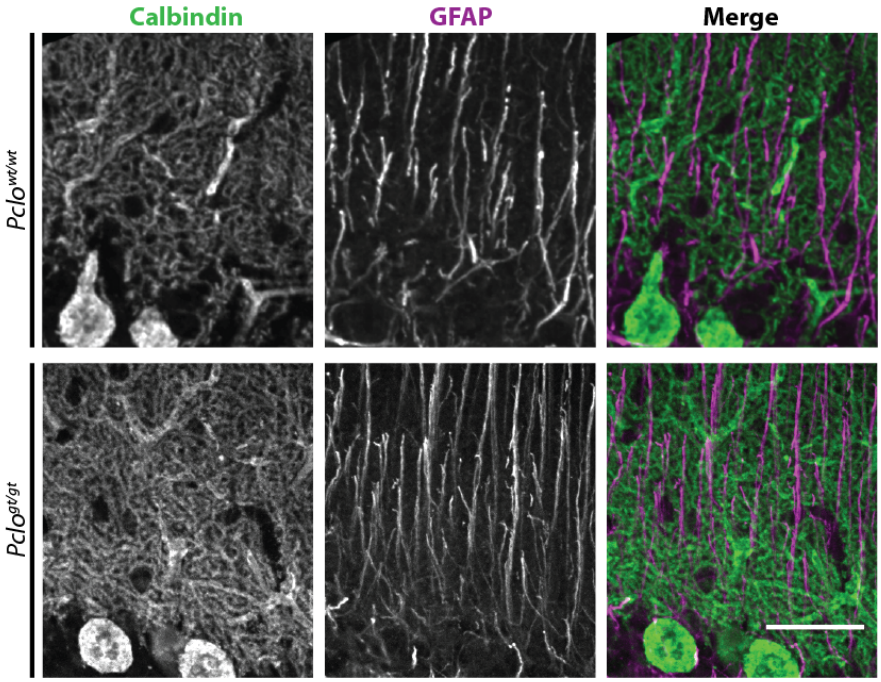

Figure 14: Radial Bergmann glia fibres appear normal in *Pclo*$^{gt/gt}$ cerebella
Images of sagittal sections from *Pclo*$^{wt/wt}$ and *Pclo*$^{gt/gt}$ cerebella at 3 month of age immunostained with antibodies against Calbindin and GFAP. Radial Bergmann glial fibres in the ML appear to be correctly formed and orientated. Scale bar = 50 µm.

6.4 Piccolo loss of function does not affect neurone subtypes and their distribution in the hippocampus, cerebral and the cerebellar cortices

Taking an exploratory approach, we took a closer look at cells in the hippocampus and the cerebral cortex. Cell development and layer formation has been extensively studied in these areas [51, 172] and can be affected by mutations in the Reelin gene, causative for some disorders such as temporal lobe epilepsy and Cerebellar Hypoplasia [51, 81]. As discussed above and can be seen in Figure 12, the brains of *Pclo*$^{gt/gt}$ are smaller than their wildtype counterparts, as can also be observed in a cortical section from 6-week-old animals (Figure 15A). Golgi staining of hippocampal and cortical neurones labelled 1-3 % of these cells (Figure 15A) [198] and allows for both a qualitative and quantitative assessment of cell morphologies. Upon closer inspection of hippocampal CA1 pyramidal cells, we

found branching, layer formation and orientation to be normal (Figure 15A and B). In both *Pclo*$^{gt/gt}$ and *Pclo*$^{wt/wt}$, we can observe CA1 pyramidal cells (PyCs), defined by their triangular-shaped soma and spiny dendrites as well as their somatic position within *Stratum Pyramidale* with somas correctly situated in *Stratum Pyramidale*, basal dendritic trees occupying *Stratum Oriens* and apical dendrites branching in *Stratum Radiatum* (Figure 15B) [98].

Cortical cells are typically arranged into layers to optimise cell signalling and to increase computing power of incredibly complex cortical network [118]. In Figure 15A and C, cells of the cortex can be observed in a laminar organisation, which can be distinguished by the arrangement of PyC bodies and dendrites. In both *Pclo*$^{wt/wt}$ and *Pclo*$^{gt/gt}$, PyC somas are found in layers 2/3, 5 and 6, with apical dendrites reaching toward the *pia* and the basal dendritic tree branching around the soma.

To investigate branching further, we reconstructed the principle CA1 cells of the hippocampus from Golgi-stained sections. For neuronal reconstructions, we used brains from 6-week-old animals as staining of the hippocampus proved to be more abundant and of higher quality at this younger age. It is speculated that, due to a smaller size brain at 6 weeks, penetration of potassium chromate was improved and so cells in the deeper regions of the brain were visualised better. The laminar organisation and dendritic branching should be well established at this age [12]; therefore parameters investigated are expected to be consistent with data collected from 3-month animals, as in the remainder of this thesis. Sholl analysis revealed no significant differences between *Pclo*$^{gt/gt}$ and *Pclo*$^{wt/wt}$ in terms of length and intersections of PyC dendrites present in each Sholl ring (Figure 16A-C). The number of nodes did differ at 90 μm from the soma, where *Pclo*$^{gt/gt}$ had significantly fewer nodes of their basal dendrites than *Pclo*$^{wt/wt}$. This difference reflects the whole group rather than one outlier (mean number of nodes: *Pclo*$^{wt/wt}$ = 1.33; *Pclo*$^{gt/gt}$ = 0.17). However, on the whole, we did not consider there to be any drastic differences in dendritic branching between *Pclo*$^{wt/wt}$ and *Pclo*$^{gt/gt}$ (Figure 16).

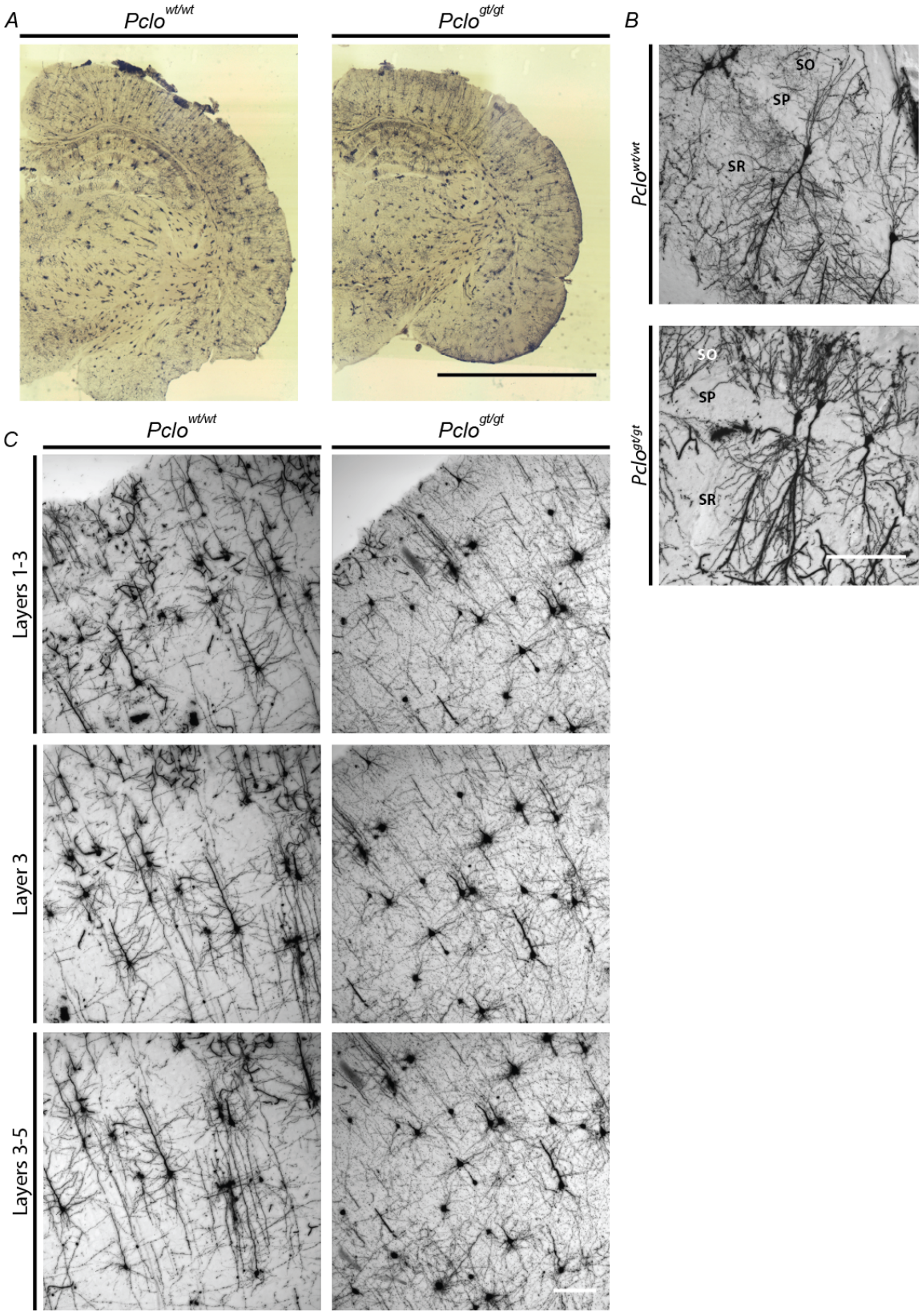

Figure 15: Layer formation and dendritic branching are normal in the cortex and hippocampus of *Pclo*$^{gt/gt}$ rat brains

A) Coronal section of Golgi-stained rat brains at 6 weeks of age. B, C) Images taken from coronal sections of 3-month brains from *Pclo*$^{wt/wt}$ and *Pclo*$^{gt/gt}$ rats. B) Hippocampal pyramidal cells are correctly orientated and their somata and dendrites are situated in the correct layers. C) Cortical pyramidal cells correctly form layers and dendrites branch in the appropriate orientation. Scale bars = 5 mm in A; 500 µm in B, C.

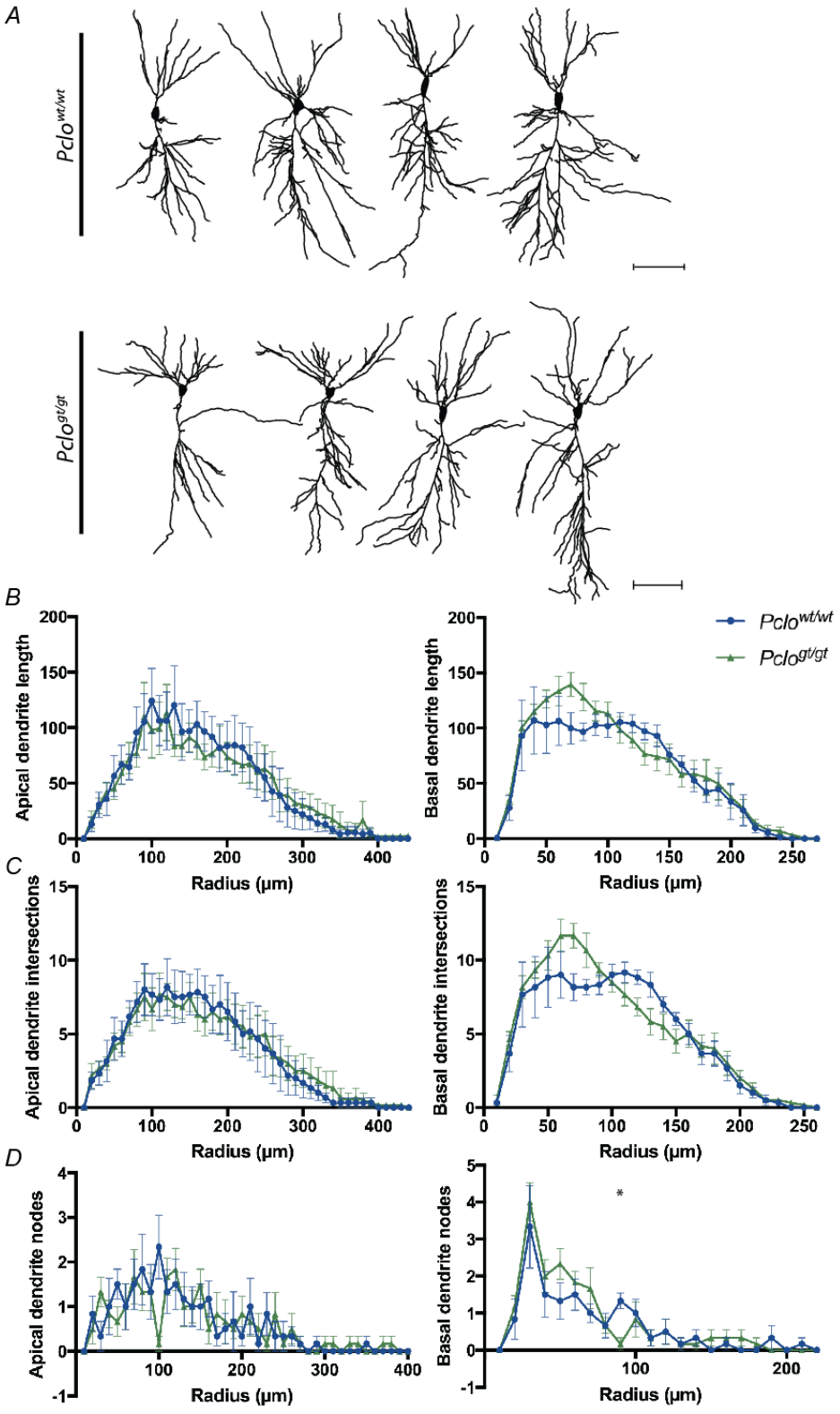

Figure 16: No change in dendritic branching of pyramidal cells in *Pclo*$^{gt/gt}$ hippocampi

A) Examples of Neurolucida reconstructions of hippocampal pyramidal cells from 6-week-old animals. B, C) Sholl analysis of Neurolucida reconstructions reveals no changes in basal or apical dendrite properties such as length (B) or intersections (C). D) At 90 µm from the soma, *Pclo*$^{gt/gt}$ neurones demonstrate a significantly lower number of nodes; all other distances were not significantly different (mean number of nodes at 90 µm: *Pclo*$^{wt/wt}$ = 1.33 ± 0.211 nodes; n = 6 cells; *Pclo*$^{gt/gt}$ = 0.167 ± 0.167; n = 6 cells, 1 independent experiment; unpaired t-test (10), $t = 4.341$, $p^* = 0.274$). Scale bars = 100 µm.

Taking advantage of the Golgi staining technique, we also looked at the different cell types within the cerebellum. This revealed that most of the different neuronal cell types such as the ML interneurones (basket and stellate cells), granule cells and Golgi interneurones migrate to their appropriate layers and grow dendrites in the correct orientation. This is also true for the morphologies of GCs and interneurones of the GCL and ML, which are comparable between $Pclo^{wt/wt}$ and $Pclo^{gt/gt}$ (Figure 17). Due to their extensive dendritic arbour and the sparse labelling of the Golgi technique, PCs were not found contained within any one of the Golgi-stained sections. However, the positioning and dendritic arbours of PCs, as assessed by Calbindin staining (see Figure 13), suggest that these cells differentiate normally.

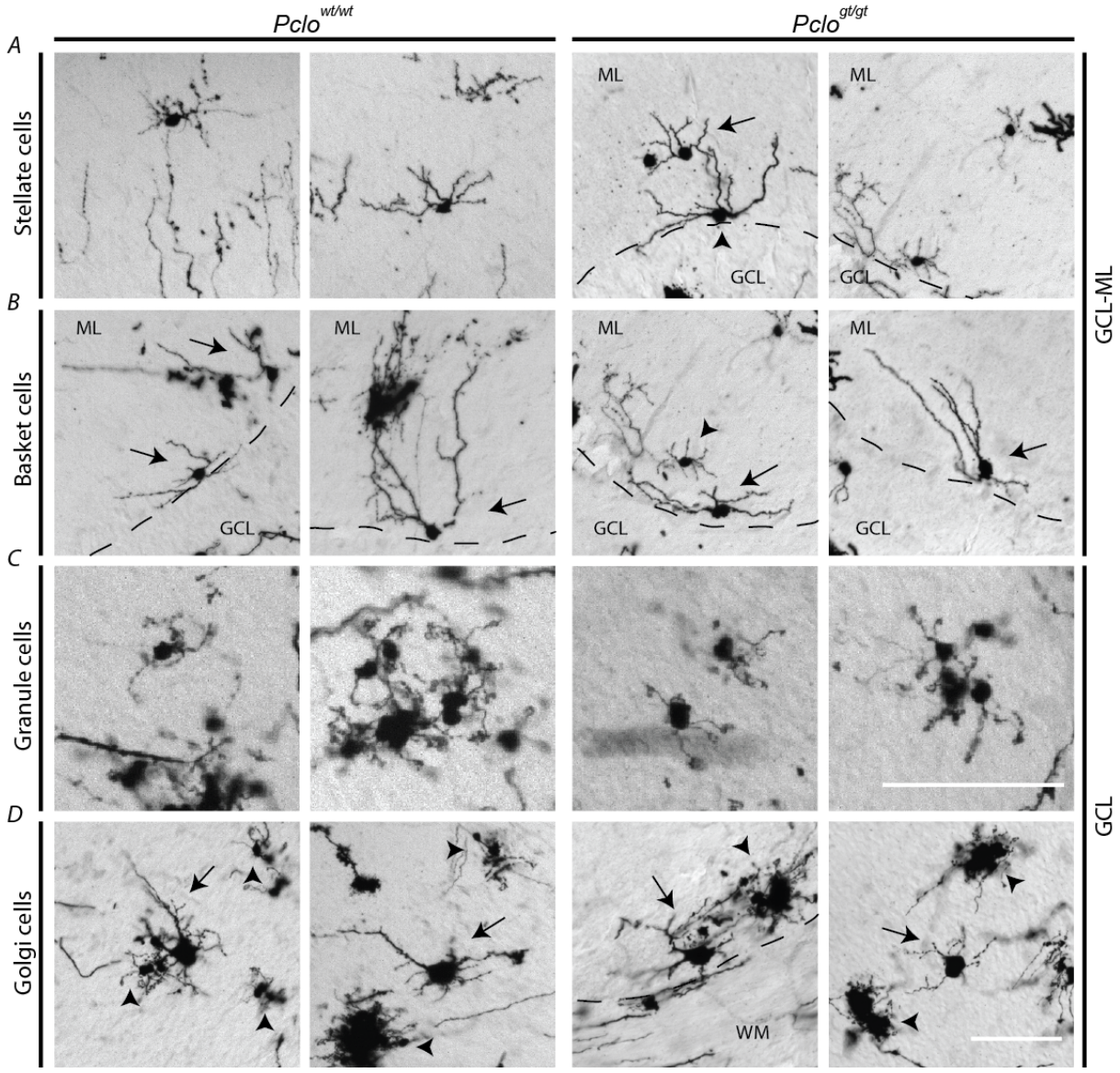

Figure 17: Cerebellar cell morphology and positioning appears normal in *Pclo*$^{gt/gt}$ animals

Golgi staining of cerebellar cells. A) Putative stellate cells were found correctly oriented in the upper portion of the ML (arrows), defined by star-like shape and dendritic processes radiating from the soma. Arrowhead = Putative basket cell of the ML. B) Putative basket cells (arrows) in the ML are found in the lower portion of the ML with their long, sparsely branching dendrites ramifying in the ML. Putative stellate cells (arrowhead) can also be observed in the ML. C) Putative granule cells of the GCL can be identified by their small size and ~ four claw-like dendrites protruding from the soma. Putative granule cells (arrowheads) can also be observed in this cell layer. D) Putative Golgi cell bodies reside in the GCL but have much larger somas than granule cells, their dendrites extend into the ML. ML = molecular layer, GCL = granule cell layer, WMT = white matter tract. Arrows = cells referred to in legend on left hand side, arrowheads = other cells present in field of view. Cell types were distinguished based on the location of their soma and dendrites; hence, a "putative" cell type classification has been given. A complete classification would require the entire dendritic/axonal arbours and in some cases immunostaining for molecular markers. Scale bars = 250 µm.

6.5 Network analysis: Loss of Piccolo alters climbing fibre and mossy fibre innervation in the cerebellum

As Piccolo is located primarily at the presynaptic active zone in the developing and adult brain, it is not surprising that the orientation, layering and branching of major cell types within the brain are unaffected by the loss of Piccolo. However, given its location at the active zones of presynaptic boutons [23], we investigated the effect of Piccolo LOF directly on the formation and maturation of several cerebellar synapses. Given that the pons and cerebellum are the most severely affected regions in terms of size in $Pclo^{gt/gt}$ brains (and the synaptic terminals of pontine neurones terminate in the granule cell layer of the cerebellum), we took a closer look at the synapses within the cerebellum. The cerebellum receives its major excitatory afferents in the form of CFs and MFs that project from the inferior olive or the brainstem/spinal cord respectively [106]. Both form glutamatergic synapses that terminate in different layers of the cerebellum [9]. For example, CFs form excitatory synapses onto the proximal branches of PC dendritic arbours, modulating the dynamic firing properties of PCs and motor learning[70]. In contrast, MFs terminate on the dendrites of GCs, which then provide direct excitatory input to PCs via their PF axons. Both also extend collaterals to the deep cerebellar nuclei before projecting into the cerebellar cortex [162].

In previous studies, we observed that Piccolo was present in the boutons of each of these excitatory synapses [23]. This was confirmed by immunostaining cerebellar sections of $Pclo^{wt/wt}$ and $Pclo^{gt/gt}$ brains with antibodies against Piccolo and the SV protein VGluT1 (Figure 10D and E). This revealed that Piccolo immunoreactivity was indeed present at each of these synaptic types and that this immunoreactivity was lost in cerebella from $Pclo^{gt/gt}$ animals. To explore whether deficiencies in either could contribute to the anatomical and functional changes in the cerebellum, we first looked for general synaptic markers in the ML and GCL of the cerebellum.

Using antibodies against Neuroligin3 (Ngl3), an adhesion molecule localised to postsynaptic densities and VGluT1 to visualise PF presynapses, we observed that excitatory synapses throughout the ML are formed in both $Pclo^{wt/wt}$ and $Pclo^{gt/gt}$ animals (Figure 18A). Specifically, VGluT1 positive PFs project from GCs in the GCL into the ML and form synapses onto PC dendrites. These can be seen tightly packed in the ML of $Pclo^{wt/wt}$ and $Pclo^{gt/gt}$ cerebella (Figure 18A). This implies that PF axons project normally and form a robust number of synapses with PCs. Given that fewer number of GCs in $Pclo^{gt/gt}$ cerebella (Figure 13A-D), we postulate that the thinner ML, observed in Figure 13, is most likely due to fewer PFs and therefore less total synaptic innervation of PC dendrites.

Robust Nlg3 staining is also observed throughout the ML for both genotypes (Figure 18A). Nlg3 is present at both excitatory and inhibitory synapses; hence staining could represent postsynaptic sites juxtaposed to climbing fibre collaterals, parallel fibres or ML interneurones. In the GCL, excitatory synapses, known as mossy fibre rosettes, are present that arise from precerebellar nuclei or in some cases internally from unipolar brush cells. Immunostaining $Pclo^{wt/wt}$ and $Pclo^{gt/gt}$ cerebella with VGluT1 antibodies revealed that immunopositive glomeruli are severely reduced in size in

Pclo$^{gt/gt}$ cerebella (Figure 18B). It should be noted, however, that the presence of Nlg3 puncta juxtaposed to VGluT1 positive puncta indicate that pre- and postsynaptic sites still align indicating that MF terminals in *Pclo*$^{gt/gt}$ cerebella still form functional synapses, a topic explored by electrophysiological experiments presented below.

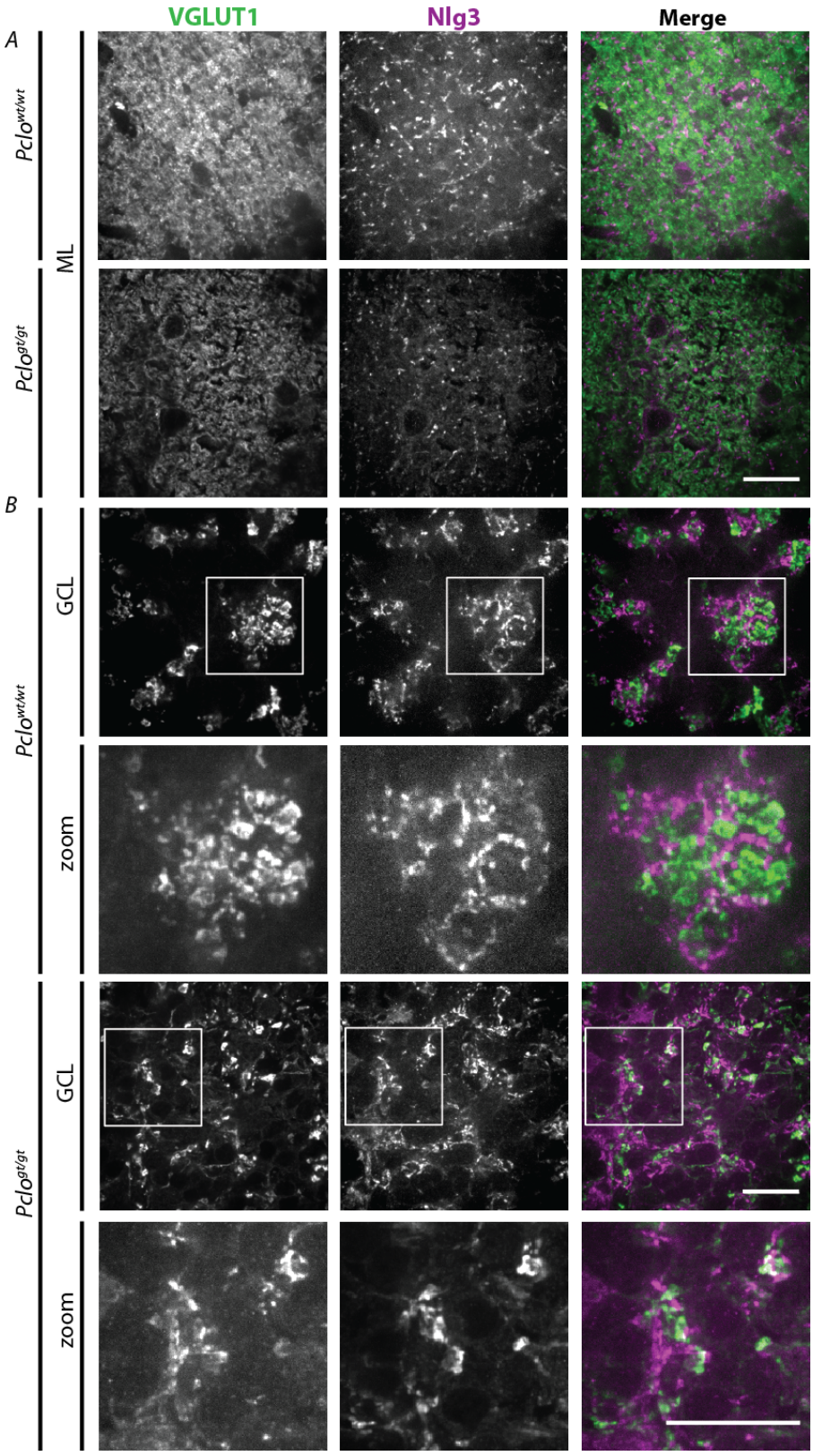

Figure 18 (figure legend on next page)

Figure 18: Images show no drastic changes in synapse distribution in the ML, but reduced size of MF boutons in the GCL of *Pclo*$^{gt/gt}$
A, B) High magnification images of sagittal sections of *Pclo*$^{wt/wt}$ and *Pclo*$^{gt/gt}$ cerebella from 3-month-old rats. A) VGluT1 staining was used to visualise PF boutons from GCs in the ML, whilst Nlg3 marks postsynaptic densities. No overt differences between genotypes were observed. B) In the GCL, VGluT1 was used to visualise MF glomeruli; Nlg3 marks postsynaptic densities. In *Pclo*$^{wt/wt}$ large MF glomeruli with multiple pre- and postsynaptic sites can be observed. In *Pclo*$^{gt/gt}$ presynaptic areas are dramatically smaller than in *Pclo*$^{wt/wt}$. Postsynaptic densities are present and align with presynaptic proteins at MF synapses in both *Pclo*$^{wt/wt}$ *and Pclo*$^{gt/gt}$ animals. Scale bars = 20 µm.

We also investigated the formation of inhibitory synapses within the cerebellum. Here, we stained sagittal sections with antibodies against the vesicular GABA transporter (VGAT) and Gephyrin, a postsynaptic scaffold protein specific to inhibitory postsynapses. In the molecular layer, we detected alignment of presynaptic VGAT and postsynaptic Gephyrin puncta, likely synapses from ML interneurones onto PCs. The pattern of staining is similar in both genotypes, indicating normal innervation of interneurones onto PCs in the ML (Figure 19A). In the GCL, presynaptic MF terminals are modulated by GABAergic input from Golgi interneurones (Figure 19B). As mentioned, the excitatory presynaptic area is greatly reduced in *Pclo*$^{gt/gt}$ compared to wildtype; however the presence and size of VGAT positive puncta does not seem to be as noticeably different between genotypes.

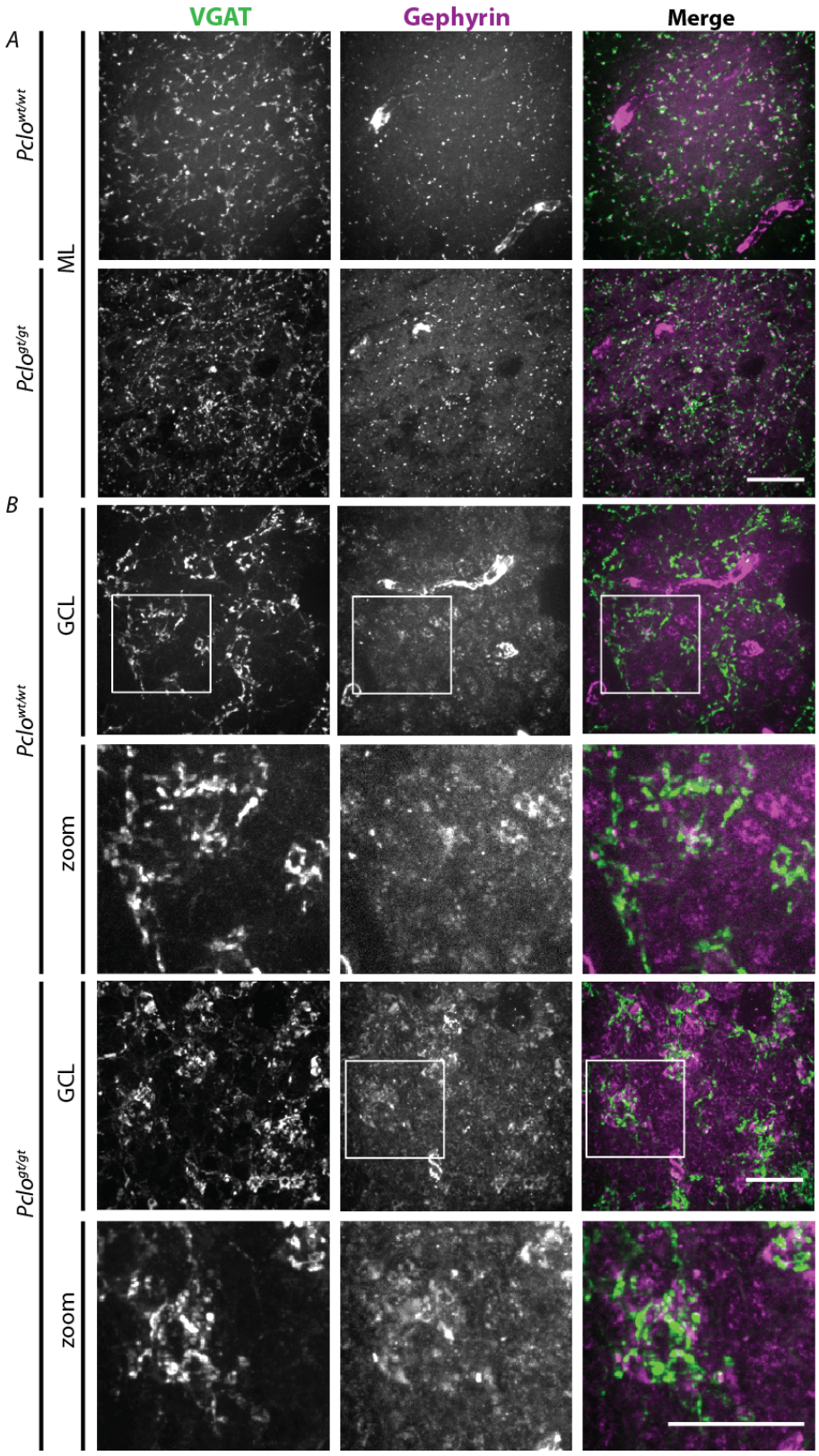

Figure 19 (figure legend on next page)

Figure 19: Images of the cerebellar cortex reveal no overt differences in inhibitory synapse arrangement between *Pclo*$^{wt/wt}$ and *Pclo*$^{gt/gt}$.

A, B) High magnification images of sagittal sections of *Pclo*$^{wt/wt}$ and *Pclo*$^{gt/gt}$ cerebella from 3-month-old rats. A) VGAT staining in the ML was used to visualise GABAergic presynapses, whilst Gephyrin antibodies revealed inhibitory postsynaptic densities. In the ML, colocalising VGAT and Gephyrin puncta likely represent synapses from ML interneurones forming onto other interneurones or PCs in both *Pclo*$^{wt/wt}$ *and Pclo*$^{gt/gt}$. B) VGAT and Gephyrin also colocalise at MF rosettes. These likely represent Golgi cell inhibition at the MF-GC synapse. Other than the aforementioned changes in MF size (Figure 9), the normal arrangement of inhibitory synapses seen in *Pclo*$^{wt/wt}$ cerebella are also present in *Pclo*$^{gt/gt}$ animals. Scale bars = 20 µm.

Calbindin positive PCs are also innervated by VGluT2 positive CFs projecting from the inferior olive [121]. Here, our analysis of sagittal cerebellar sections revealed the presence of a large number of VGluT2 positive puncta decorating Calbindin positive dendrites in *Pclo*$^{gt/gt}$ and *Pclo*$^{wt/wt}$ sections (Figure 20A). These data indicate that the loss of Piccolo does not affect the ability of CFs to project into the ML and form synapses with PC soma and dendrites. Qualitatively, VGluT2 positive puncta in *Pclo*$^{wt/wt}$ and *Pclo*$^{gt/gt}$ sections were of similar size and beautifully decorated both primary and tertiary PC dendrites, though the total number of puncta appeared more numerous in *Pclo*$^{gt/gt}$ sections. Quantification of the total area of VGluT2 per ML supports this impression (Figure 20B), demonstrating a 24.3 % increase in VGluT2 coverage of the ML.

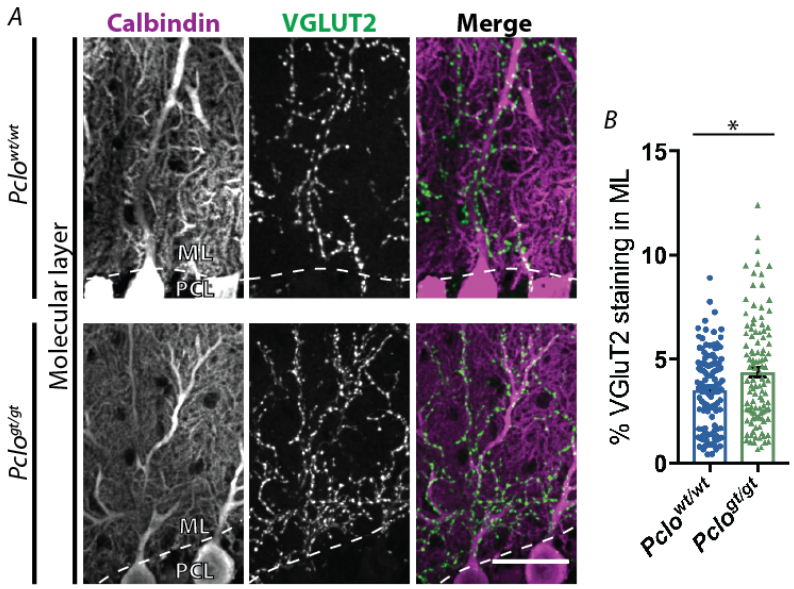

Figure 20: Aberrant climbing fibre innervation of Purkinje cells in *Pclo*$^{gt/gt}$ rats compared to *Pclo*$^{wt/wt}$

A) Images of sagittal sections of *Pclo*$^{wt/wt}$ and *Pclo*$^{gt/gt}$ cerebella at 3 months of age stained with antibodies against Calbindin and VGluT2. Note that the climbing fibre synapses, immunopositive for VGluT2, are increased in the ML of *Pclo*$^{gt/gt}$ cerebella compared to *Pclo*$^{wt/wt}$ controls.B) Quantification of the percentage of the ML (indicated by dashed lines) immunopositive for VGluT2 from (A) (*Pclo*$^{wt/wt}$ = 3.521 ± 0.160, n = 128 images; *Pclo*$^{gt/gt}$ = 4.377 ± 0.241, n = 112 images; n = 3 independent experiments; Mann-Whitney U test, U = 5987, p^* = 0.0278). Scale bar: 20 µm. Error bars represent SEM. Data points represent images taken from lobes I, III, V, VII and IX; 4 sections per animal. Adapted from Falck et al. [46].

The difference in size of VGluT1 positive MFs in the GCL of *Pclo*$^{gt/gt}$ rats (Figure 18) is striking. Precerebellar nuclei project collaterals to the GCL and form large glomerular structures with multiple AZs. The rosette of synapses is contacted by multiple claw-like dendrites from surrounding GCs; these presynaptic termini are immunopositive for VGluT1, VGluT2 or both [78, 90, 197]; differences in the expression of VGluT1 and/or VGluT2 is related to the origin of these axons from different brain stem nuclei [79]. Given initial observed difference in the morphology and size of MF terminal (Figure 18), we looked closer at the size and arrangement of these MF rosettes by staining sagittal sections of the GCL with antibodies against the somatodendritic marker MAP2 and presynaptic marker for MFs, VGluT2. In *Pclo*$^{wt/wt}$ sections, multiple large VGluT2 positive puncta are seen packed tightly together within a dense meshwork of MAP2 positive dendrites projecting from a ring of GCs. These puncta represent subclusters of SVs with large 100-200 μm^3 terminals [90]. In sections from *Pclo*$^{gt/gt}$ animals, each bouton appeared smaller in size and less organized, though they still appear to contact GC dendrites (Figure 21A). These data are consistent with those presented in Figure 18, and reveal that pre- and postsynaptic alignment appears to be intact. To quantify the size of these presynaptic areas, we stained sagittal sections with antibodies against both VGluT1 and VGluT2. In these images, distinct VGluT1 and/or VGluT2 positive clusters are observed in both *Pclo*$^{wt/wt}$ and *Pclo*$^{gt/gt}$ animals, consistent with individual boutons present per glomeruli (Figure 21B). Here again, MF terminals from *Pclo*$^{gt/gt}$ animals appeared to have much smaller VGluT1 or VGluT2 positive clusters (Figure 21B, zoom). Because the total number of puncta analysed was so large, quantification in Figure 21C was calculated as an average of cluster size per animal for each genotype. The spread of the data can be seen in Figures 12D and E. Quantifying the average size of the VGluT1 and VGluT2 positive clusters revealed that clusters in *Pclo*$^{wt/wt}$ cerebella were more than double the size of those detected in the same lobes in *Pclo*$^{gt/gt}$ animals (Figure 21B and C). In the *Pclo*$^{wt/wt}$ condition, there was no difference in size between VGluT1 and VGlut2-expressing MFs. However, in *Pclo*$^{gt/gt}$ cerebella, VGlut2 clusters are significantly smaller than VGluT1 clusters, but both were dramatically smaller than in *Pclo*$^{wt/wt}$ (mean cluster size: *Pclo*$^{wt/wt}$ VGluT1 = 23.05 μm^2, VGluT2 = 25.71 μm^2; *Pclo*$^{gt/gt}$ VGluT1 = 8.463, VGluT2 = 11 μm^2) (Figure 12D). Furthermore, the distribution of VGluT1/2 cluster sizes is far more shifted towards smaller cluster sizes in *Pclo*$^{gt/gt}$, with mutant cerebella displaying approximately 45 % more small synaptic clusters of 5 μm^2 in size than *Pclo*$^{wt/wt}$ counterparts (Figure 21E). At the larger end of the scale, cluster sizes over 50 μm^2 were much more frequent for *Pclo*$^{wt/wt}$ than *Pclo*$^{gt/gt}$ cerebella (Figure 21E).

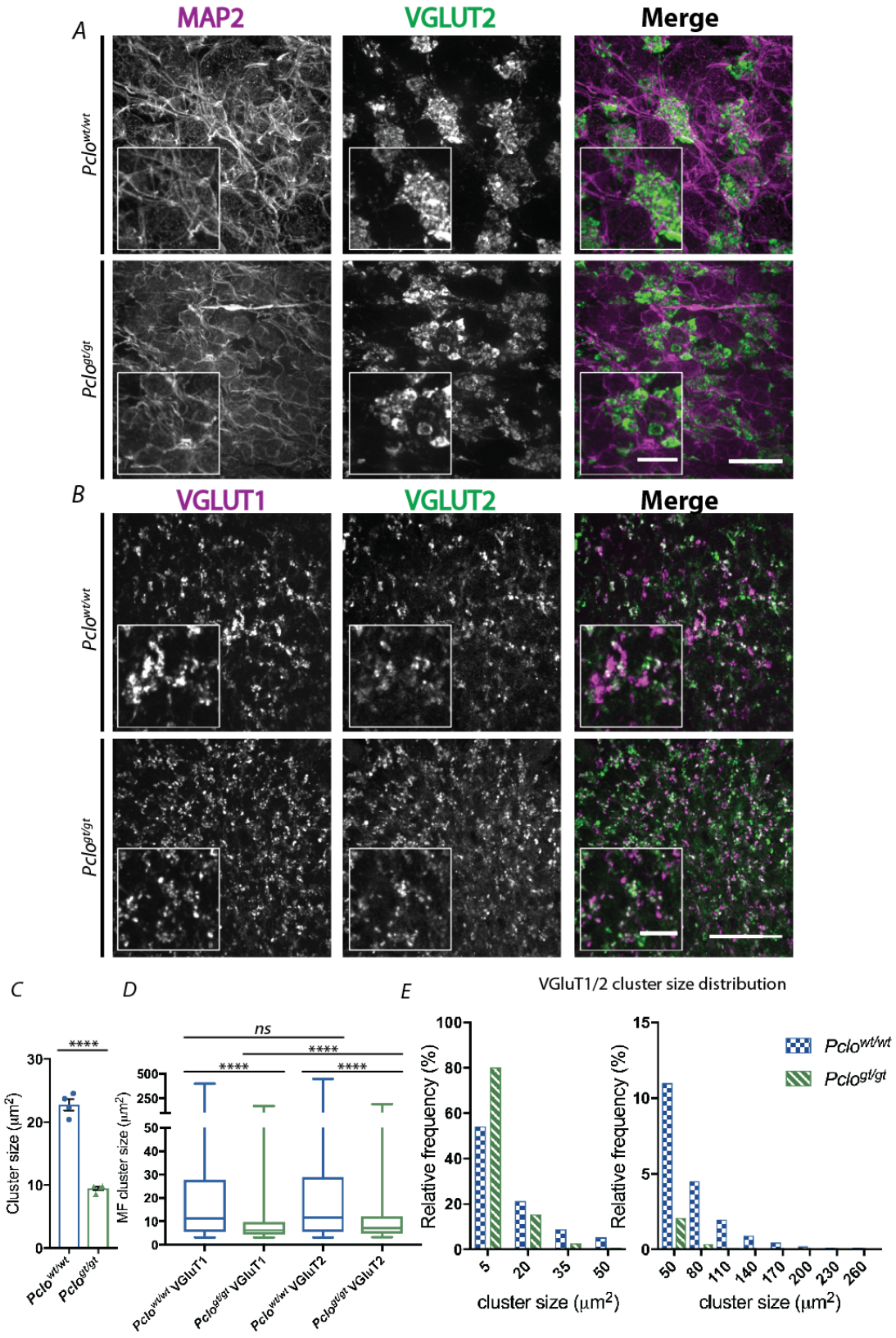

Figure 21 (figure legend on next page)

Figure 21: Cerebella from *Pclo*$^{gt/gt}$ animals have smaller mossy fibre rosettes

A, B) Images of sagittal sections of *Pclo*$^{wt/wt}$ and *Pclo*$^{gt/gt}$ cerebella at 3 months of age stained with antibodies against VGluT2, a presynaptic protein highly expressed at MF boutons, and the somatodendritic marker MAP2 (A) or VGluT2 and VGluT1 (B). A) GCs extend their dendrites into MF boutons in the *Pclo*$^{wt/wt}$ condition. However, in *Pclo*$^{gt/gt}$, whilst GC dendrites are still juxtaposed to VGluT2 positive boutons, the boutons are smaller and therefore the arrangement is less organised. B) Presynaptic MF glomeruli from lobe VII are visualised by VGluT1 and VGluT2. C) Quantification of the size of VGluT1/VGluT2 clusters, averaged per animal (*Pclo*$^{wt/wt}$ = 22.73 µm^2 ± 0.896, n = 4 animals; *Pclo*$^{gt/gt}$ = 9.46 µm^2 ± 0.2899, n = 4 animals; unpaired t-test (6), t = 14.1, p**** < 0.0001). Data points represent average puncta size per animal. D) Quantification of VGluT1 and VGluT2 clusters in *Pclo*$^{wt/wt}$ and *Pclo*$^{gt/gt}$ (VGluT1 mean cluster size: *Pclo*$^{wt/wt}$ = 23.05 µm^2 ± 0.267, n = 12659 puncta; *Pclo*$^{gt/gt}$ = 8.463 µm^2 ± 0.0752, n = 9736 puncta; VGluT2 mean cluster size: *Pclo*$^{wt/wt}$ = 25.71 µm^2 ± 0.343, n = 11640 puncta; *Pclo*$^{gt/gt}$ = 11 µm^2 ± 0.127, n = 8874 puncta. Mann-Whitney U test *Pclo*$^{wt/wt}$ VGluT1 vs VGluT2 puncta size: U = 72640213, p = 0.0581; *Pclo*$^{gt/gt}$ VGluT1 vs. VGluT2 puncta size: U = 38387685, p**** = <0.0001. Mann-Whitney U test VGluT1 puncta size *Pclo*$^{wt/wt}$ vs. *Pclo*$^{gt/gt}$: U = 38369400, p**** = <0.0001; VGluT2 puncta size *Pclo*$^{wt/wt}$ vs. *Pclo*$^{gt/gt}$: U = 36797263, p**** = <0.0001). E) Histograms to show the distribution of puncta sized 5-50 µm^2 (left) and 50-260 µm^2 (right). The shift of the data indicates *Pclo*$^{gt/gt}$ MFs have more smaller puncta (5 µm^2), whereas *Pclo*$^{wt/wt}$ MFs have more larger puncta (up to 260 µm^2). Scale bars = 20 µm in A; 10 µm in A (zoom); 50 µm in B; 20 µm in B (zoom). Error bars represent SEM. Data points represent individual animals (C) or individual puncta (D). Images taken from lobes I, III, V, VII and IX, 4 sections per animal (C, D, E). Adapted from Falck et al. [46].

Different precerebellar nuclei terminate in different lobes within the cerebellum [164], therefore we checked for differences in size distribution across different lobes. There was no difference between the size of *Pclo*$^{gt/gt}$ MF terminals across all lobes measured (Figure 22A, B). These findings suggest that defects in the formation of large robust MF glomeruli in *Pclo*$^{gt/gt}$ cerebella is a common feature shared by MF afferents arising from the pons and other brainstem nuclei, and may reflect aberrant signalling during development between GCs and these neurones.

Interestingly, the number of MF terminals per area of the GCL was unchanged between *Pclo*$^{wt/wt}$ and *Pclo*$^{gt/gt}$ animals (Figure 22C). In contrast, the total area covered by VGluT1/2 staining was dramatically reduced in *Pclo*$^{gt/gt}$ (mean VGluT1/2 per µm^2: *Pclo*$^{wt/wt}$ = 0.479; *Pclo*$^{gt/gt}$ = 0.207) (Figure 22D). This is consistent with data showing that each puncta is smaller in size (Figure 21C-E). Interestingly, we also observed a reduction in the number of pontine nuclei cell bodies (Figure 12), which could be expected to reduce the number of presynaptic terminals reaching the GCL. Intriguingly, the number of puncta per area remains the same. Given that there are fewer GCs reaching the GCL and there are less cell bodies in the pontine nucleus (Figure 12B, C and E and Figure 13B and D), it seems that the pontocerebellar connections are scaling the same, e.g. the ratio of GCs, MFs and precerebellar cells remains the same in *Pclo*$^{gt/gt}$ brains, as in the *Pclo*$^{wt/wt}$ condition. An interesting question is how these ratios are normally controlled and whether such mechanisms operate in *Pclo*$^{gt/gt}$ animals or whether it is only the consequence of Piccolo loss in each cell type disrupting only the number of cells born in each area.

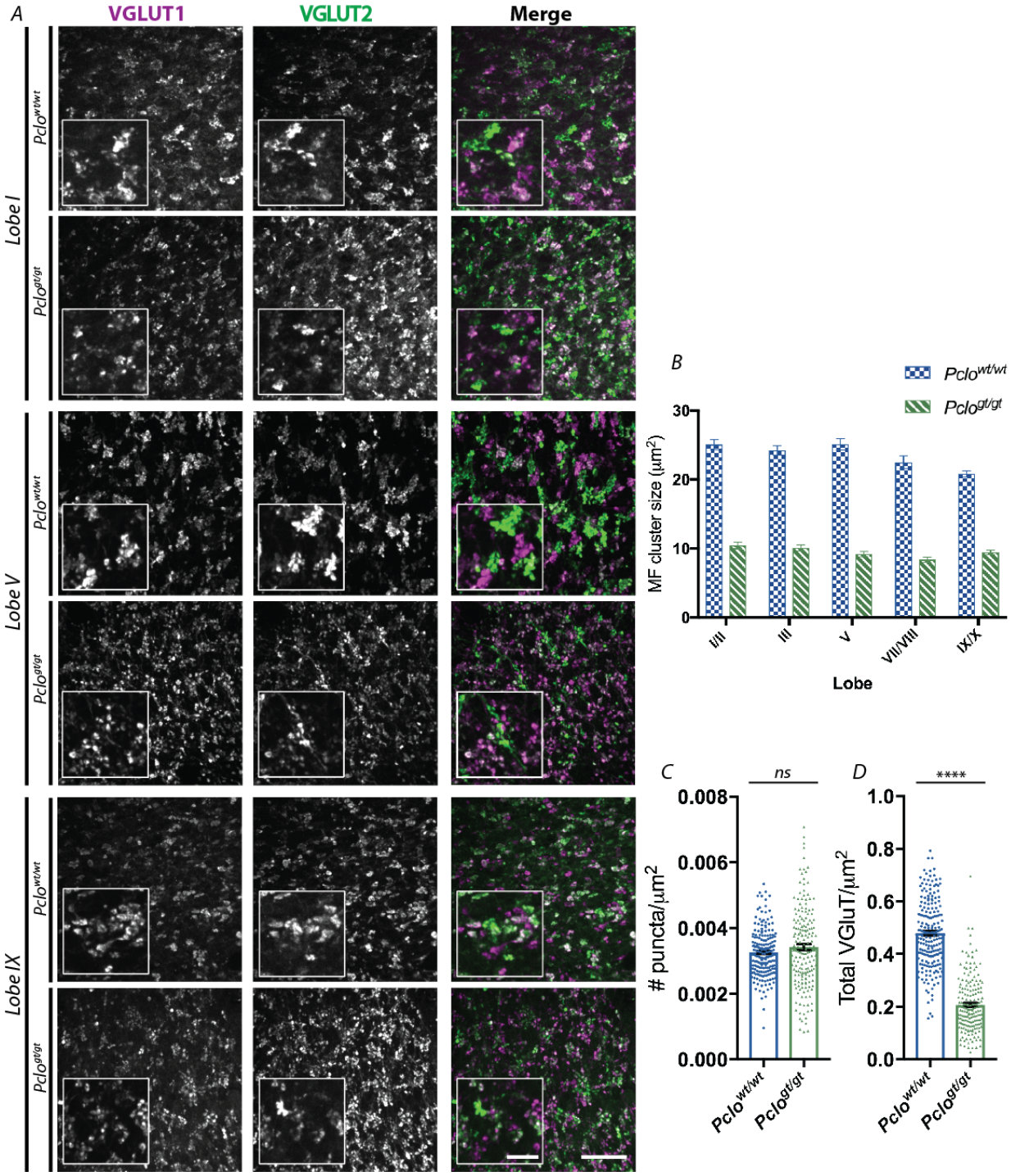

Figure 22 (page 63): Reduction in MF size is not lobe-specific in *Pclo*$^{gt/gt}$

A) Images of sagittal sections of *Pclo*$^{wt/wt}$ and *Pclo*$^{gt/gt}$ cerebella at 3 months of age stained with antibodies against VGluT1 and VGluT2 to label MFs. Presynaptic MF glomeruli from lobes I (upper panel), V (middle panel) and IX (lower panel) are constantly smaller in size in *Pclo*$^{gt/gt}$ cerebella regardless of the lobe. B) Quantification of the size of VGluT1/VGluT2 clusters in images collected from lobes I-IX (Lobe I/II: *Pclo*$^{wt/wt}$ = 25.06 µm^2 ± 0.709, n = 43 images; *Pclo*$^{gt/gt}$ = 10.44 µm^2 ± 0.51, n = 34 images; lobe III: *Pclo*$^{wt/wt}$ = 24.2 µm^2 ± 0.65, n = 42 images; *Pclo*$^{gt/gt}$ = 10.09 µm^2 ± 0.45, n = 34 images; lobe V: *Pclo*$^{wt/wt}$ = 25.14 µm^2 ± 0.827, n = 42 images; *Pclo*$^{gt/gt}$ = 9.19 µm^2 ± 0.37, n = 44 images; lobe VII/VIII: *Pclo*$^{wt/wt}$ = 22.5 µm^2 ± 0.932, n = 34 images; *Pclo*$^{gt/gt}$ = 8.354 µm^2 ± 0.389, n = 30 images; lobe IX/X: *Pclo*$^{wt/wt}$ = 20.82 µm^2 ± 0.47, n = 40 images; *Pclo*$^{gt/gt}$ = 9.454 µm^2 ± 0.312, n = 40 images). C) Quantification of the number of VGluT1/2 puncta per µm^2. Density is unchanged between *Pclo*$^{wt/wt}$ and *Pclo*$^{gt/gt}$ (*Pclo*$^{wt/wt}$ = 0.00326 ± 4.969e-005, n = 201 images; *Pclo*$^{gt/gt}$ = 0.00342 ± 9.168e-005, n = 182 images; n = 4 independent experiments; unpaired t-test (381), t = 1.504, p = 0.133). D)

Quantification of the total amount of VGluT1/2 staining per μm^2 ($Pclo^{wt/wt}$ = 0.479 ± 0.00908, n = 201 images; $Pclo^{gt/gt}$ = 0.207 ± 0.00765, n = 182 images; n = 4 independent experiments; Mann-Whitney U test, U = 1928, p**** = <0.0001). Scale bars = 20 µm in A; 10 µm in A (zoom). Error bars represent SEM, data points represent individual images taken from lobes I, III, V, VII and IX. Adapted from Falck et al. [46].

In addition to excitatory input, MF glomeruli are also modulated by GABAergic inhibition via cerebellar Golgi cells that contribute regulatory feedback to the module, as they themselves are excited by GCs [111]. In principle, smaller MF terminals seen in $Pclo^{gt/gt}$ animals could represent less excitatory drive onto GCs. This may also reduce excitatory drive onto PCs via PFs from GCs, as well as perhaps inhibitory drive via the Golgi cells. One of the dominant receptors mediating inhibitory input from Golgi cells to GCs is the α6 subunit-expressing $GABA_A$ receptor, which is highly concentrated within MF glomeruli [130]. Sagittal sections immunostained with antibodies against VGluT2 and α6 subunits revealed that the $GABA_A$ α6 receptor subunit is only weakly expressed in $Pclo^{gt/gt}$ MF rosettes, whereas in $Pclo^{wt/wt}$, it nicely localises to the synaptic complex (Figure 23A). Antibody staining of the granule cell layer demonstrates higher intensity of $GABA_A$ α6 antibody staining in $Pclo^{wt/wt}$ compared to $Pclo^{gt/gt}$ GCL (normalised to MAP2 channel, mean intensity: $Pclo^{wt/wt}$ = 0.661 a.u.; $Pclo^{gt/gt}$ = 0.443 a.u.) (Figure 23B). Of note, knockout models of $GABA_A$α6 [80] do not display PCH3 phenotypes or alterations in the anatomy of the cerebellum. These data imply that $GABA_A$α6 downregulation can be attributed to Piccolo loss and does not necessarily generate the observed PCH3 phenotypes. Interestingly, we observed the presence of the inhibitory pre- and postsynaptic proteins VGAT and Gephyrin at the MF synapse of both $Pclo^{wt/wt}$ and $Pclo^{gt/gt}$ (Figure 19B). This suggests that though these inhibitory synapses are present in $Pclo^{gt/gt}$ animals, however, may not be fully functional as they do not express the same level of $GABA_A$α6 as $Pclo^{wt/wt}$. Whether these receptors are simply downregulated or replaced by other receptors remains to be explored.

These data suggest that the loss of Piccolo not only affects the size of MF inputs into the cerebellum but also inhibitory drive within each glomerulus, a condition that could relate to the maturation of these structures and/or their functionality and create a situation that could adversely affect cerebellar function. These concepts were explored in electrophysiological experiments presented below.

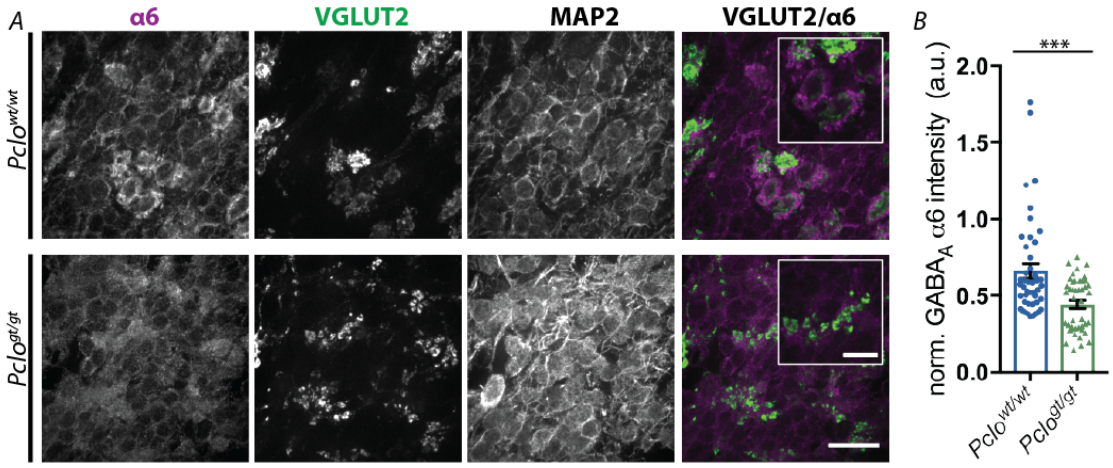

Figure 23: $GABA_A$α6 subunit expression is lower in *Pclo*$^{gt/gt}$ than in *Pclo*$^{wt/wt}$

A) Representative images of sagittal sections of *Pclo*$^{wt/wt}$ and *Pclo*$^{gt/gt}$ cerebella at 3 months of age stained with antibodies against the $GABA_A$ subunit α6, VGluT2 and MAP2. Note the decreased levels of $GABA_A$α6 in the GCL of *Pclo*$^{gt/gt}$ animals compared to *Pclo*$^{wt/wt}$ controls. B) Quantification of $GABA_A$ α6 subunit, measured by the average intensity of antibody staining in images taken from the GCL of the cerebellum normalised to MAP2 antibody intensities for the same image (*Pclo*$^{wt/wt}$ = 0.661 ± 0.0479 a.u., n = 45 images from 3 individual animals; *Pclo*$^{gt/gt}$ = 0.443 ± 0.26 a.u., n = 44 images from 3 individual animals; Mann-Whitney U test, U = 589, p*** = 0.0009). Scale bars = 20 µm. Error bars represent SEM. Data points represent individual image intensities. Adapted from Falck et al. [46].

6.6 Synapse analysis: ultrastructural changes in *Pclo*$^{gt/gt}$ mossy fibre glomeruli

The reduced area of VGluT1 and VGluT2 clusters within *Pclo*$^{gt/gt}$ MF terminals (Figures 18, 21 and 22) could be due to a reduction in size of MF glomeruli themselves and/or in the number of VGluT1/2 positive SVs per bouton. To explore these possibilities, we investigated MF glomeruli in *Pclo*$^{wt/wt}$ and *Pclo*$^{gt/gt}$ cerebella using electron microscopy (EM). Analysis of ultrathin cerebellar brain sections revealed that the average size of *Pclo*$^{gt/gt}$ glomeruli was significantly smaller than *Pclo*$^{wt/wt}$ glomeruli (mean glomeruli area: *Pclo*$^{wt/wt}$ = 34.59 µm^2; *Pclo*$^{gt/gt}$ = 18.82 µm^2) (Figure 24A and C), while the number of SVs per area remained unchanged (Figure 25C). These findings provide evidence for an overall reduction of SVs at MF terminals. Furthermore, the complexity of the glomeruli indicated by a P2A value - measuring the ratio of perimeter per area - was significantly reduced by 35.8 % (Figure 24B and E). The size of the presynaptic area was also reduced in *Pclo*$^{gt/gt}$ cerebellar sections (mean presynaptic area: *Pclo*$^{wt/wt}$ = 17.73 µm^2; *Pclo*$^{gt/gt}$ = 11.69 µm^2) (Figure 24B and D).

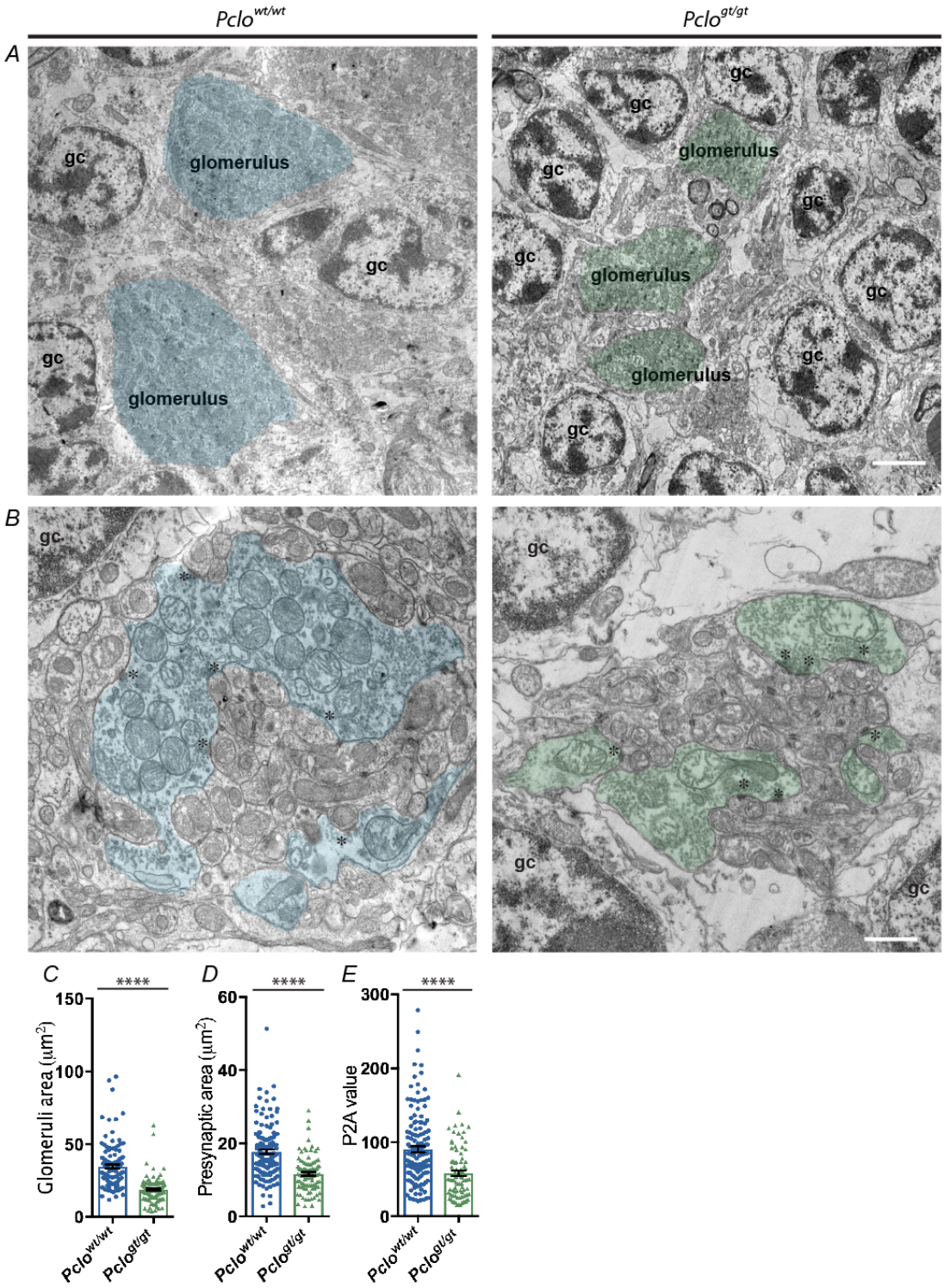

Figure 24: Glomerular rosettes are smaller and less complex in *Pclo*$^{gt/gt}$

A-D) Electron microscopy images of the GCL of *Pclo*$^{wt/wt}$ and *Pclo*$^{gt/gt}$ cerebella at 3 months of age. Granule cells are indicated by "gc", cerebellar glomeruli/presynaptic terminals are highlighted in blue (*Pclo*$^{wt/wt}$) and green (*Pclo*$^{gt/gt}$) (A, B). Asterisks mark AZs (B). C-E) Quantification of the size of glomeruli (C) and the size (D) and complexity (E) of the MF presynapse. Note the strong decrease in MF size and complexity (C) (*Pclo*$^{wt/wt}$ = 34.59 µm^2 ± 1.287, n = 130 images; *Pclo*$^{gt/gt}$ = 18.82 µm^2 ± 0.853, n = 103 images; n = 3 independent experiments; Mann-Whitney U test, U = 1733, p**** < 0.0001). (D) (*Pclo*$^{wt/wt}$ = 17.73 µm^2 ± 0.603, n = 141 images; *Pclo*$^{gt/gt}$ = 11.69 µm^2 ± 0.497, n = 95 images; n = 3 independent experiments; Mann-Whitney U test, U = 3057, p**** < 0.0001). (E) (*Pclo*$^{wt/wt}$ = 90.5 ± 4.089, n = 141 images; *Pclo*$^{gt/gt}$ = 58.1 ± 3.818, n = 84 images; n =

3 independent experiments; Mann-Whitney U test, $U = 3373$, $p^{****} < 0.0001$). Scale bars = 2.5 µm in A; 1 µm in B. Error bars represent SEM. Adapted from Falck et al. [46].

The number of AZs present at each glomerulus was still proportional to their size, as $Pclo^{wt/wt}$ and $Pclo^{gt/gt}$ had a similar number of AZs per glomerular area (Figure 24B and 25D). This leads to a reduction in the total number of AZs per presynaptic profile (mean AZs per terminal: $Pclo^{wt/wt} = 10.00$; $Pclo^{gt/gt} = 6.75$) (Figure 24B and 25F). Piccolo loss of function did not, however, affect the length of the AZ itself (Figure 25A and E). These data indicate that the overall output of the MF glomeruli could be reduced in $Pclo^{gt/gt}$ cerebellum. Intriguingly, we also noticed an accumulation of Clathrin-coated vesicles (CCVs) in the terminals of $Pclo^{gt/gt}$ MFs (Figure 25B). This phenotype resembles recent findings from hippocampal synapses from $Pclo^{gt/gt}$ animals, which revealed defects in the formation of endosomal membranes and an overall reduction in SV number [2] and suggest possible changes in the recycling of SVs within MF boutons post fusion with the plasma membrane.

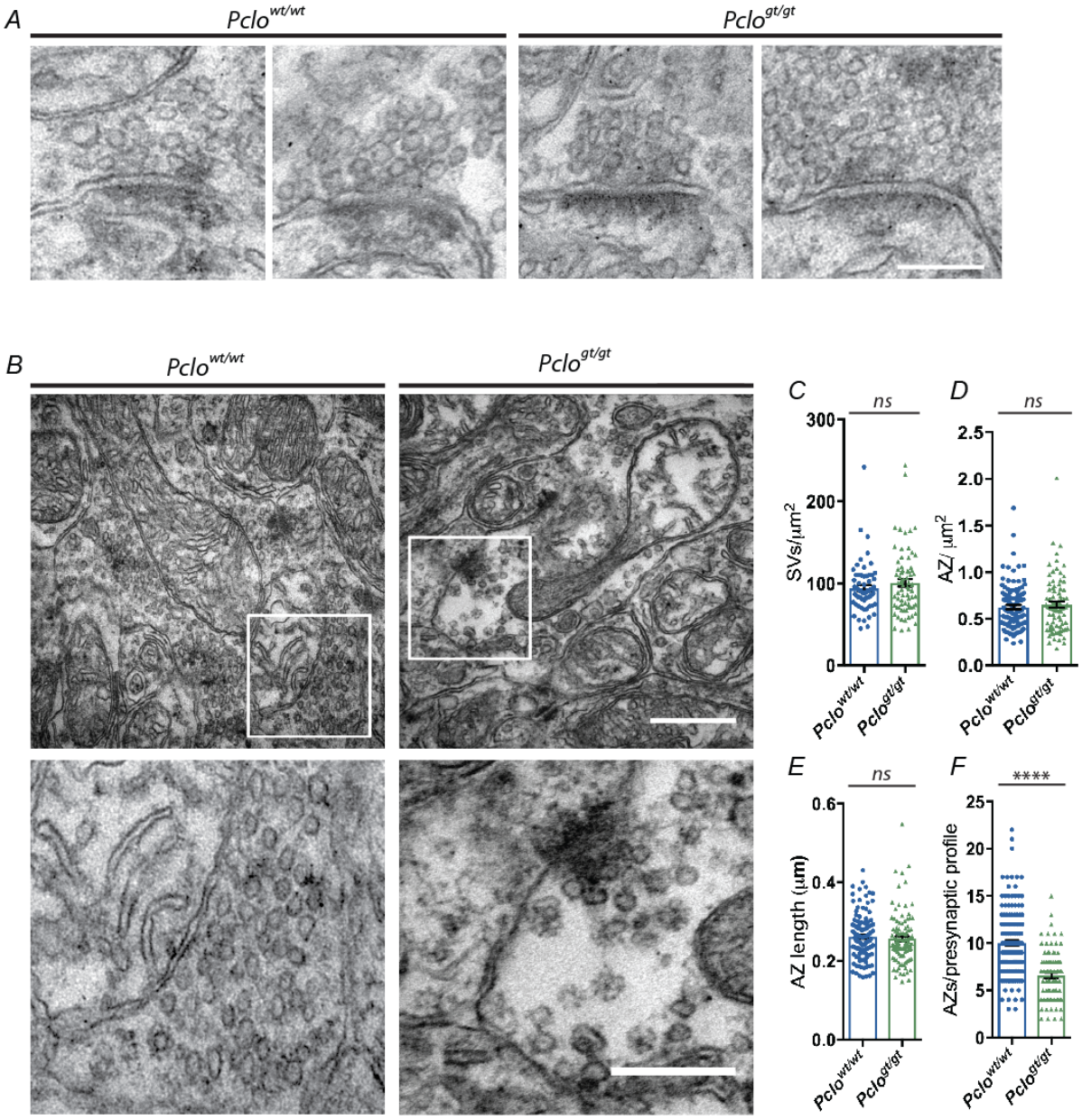

Figure 25: *Pclo*$^{gt/gt}$ glomerular rosettes have fewer SVs and AZs per terminal and an increase in CCVs

A) High magnification images of AZs at *Pclo*$^{gt/gt}$ and *Pclo*$^{wt/wt}$ MFs demonstrate the length of the AZ and the density of SVs, quantified in (C) and (E). B) demonstrates the presence of more CCVs in *Pclo*$^{gt/gt}$ MF boutons compared to *Pclo*$^{wt/wt}$ (lower panel: zoom). C-F) quantification of the density of SVs per area (C), the number of AZs per area (D), the AZ length (E) and the number of AZs per presynaptic profile (F). C) (*Pclo*$^{wt/wt}$ = 94.24 SVs/µm^2 ± 3.853, n = 62 images; *Pclo*$^{gt/gt}$ = 100.7 SVs/µm^2 ± 4.705, n = 71 images; n = 3 independent experiments; Mann-Whitney U test, U = 2042, p = 0.476). D) (*Pclo*$^{wt/wt}$ = 0.625 AZs/µm^2 ± 0.021, n = 121 images; *Pclo*$^{gt/gt}$ = 0.652 AZs/µm^2 ± 0.032, n = 84 images; n = 3 independent experiments; Mann-Whitney U test, U = 4942, p = 0.7390). E) (*Pclo*$^{wt/wt}$ = 0.261 µm ± 0.000487, n = 129 images; *Pclo*$^{gt/gt}$ = 0.257 µm ± 0.00653, n = 101 images; n = 3 independent experiments; Mann-Whitney U test, U = 5963, p = 0.271). F) (*Pclo*$^{wt/wt}$ = 10 AZs/profile ± 0.304, n = 141 images; *Pclo*$^{gt/gt}$ = 6.571 AZs/profile ± 0.295, n = 84 images; n = 3 independent experiments; Mann-Whitney U test, U = 2650, p**** < 0.0001). Scale bars = 125 nm in A; 500 nm in B; 250 nm in B (zoom). Error bars represent SEM. Adapted from Falck et al. [46].

6.7 Piccolo loss of function alters granule cell properties and mossy fibre to granule cell synaptic transmission

The anatomical and morphological changes observed in MF boutons lacking Piccolo are predicted to not only represent altered afferent input into the cerebellum from the pons and other brainstem nuclei, but also altered cerebellar function. As an initial test of this hypothesis, we performed whole-cell current clamp recordings of cerebellar GCs from acute 3-to-4-month rat cerebellar slices. A two-photon image of a typical cerebellar GC from $Pclo^{gt/gt}$ filled with ATTO dye reveals a normal radial arrangement of its dendrites as they project their claws into MF glomeruli (Figure 26A). An analysis of the intrinsic biophysical properties of these cells revealed that some GC properties differed between $Pclo^{gt/gt}$ and $Pclo^{wt/wt}$ animals. Specifically, no changes were detected in either the capacitance or the membrane potential of these cells, but the input resistance was significantly increased by 60 % (Figure 26B). Since these experiments were performed in the presence of $GABA_A$ receptor blockers, the decreased shunting inhibition mediated by tonic activation of α6-subunit-containing $GABA_A$ receptors [15, 129] is expected to further increase the difference in input resistance. Yet, there was also no change in the amplitude, threshold of activation or duration of action potentials fired by these cells (Figure 26B), indicating unaltered active membrane properties. Examining the frequency and amplitude of spontaneous miniature excitatory postsynaptic currents (mEPSCs) of these GCs revealed a dramatic increase of 151 % in the frequency of these events in $Pclo^{gt/gt}$ slices with no change in mEPSC amplitudes (Figure 26C). These data suggest that on average each excitatory synapse formed on to these GC dendrites has normal levels of postsynaptic AMPA-type glutamate receptors. The change in frequency could either be due to an increase in the number of MF boutons contacting GC dendrites and/or an increase in the release probability of MF boutons. Consistently, the average amplitude of the evoked EPSCs was increased in $Pclo^{gt/gt}$ animals (mean EPSC amplitude: $Pclo^{wt/wt}$ = 47.58 pA; $Pclo^{gt/gt}$ = 67.62 pA), with no change in the weighted time constant (τ_w) (Figure 26D). Given the amplitudes of the mEPSCs are not changed, these results suggest that there is a higher number of synaptic connections between MF boutons and the dendrites of GCs. Taken together, these data indicate that, in addition to changes in GC number, the loss of Piccolo in the cerebellum and brainstem is associated with changes in the function of GCs and their mossy fibre input.

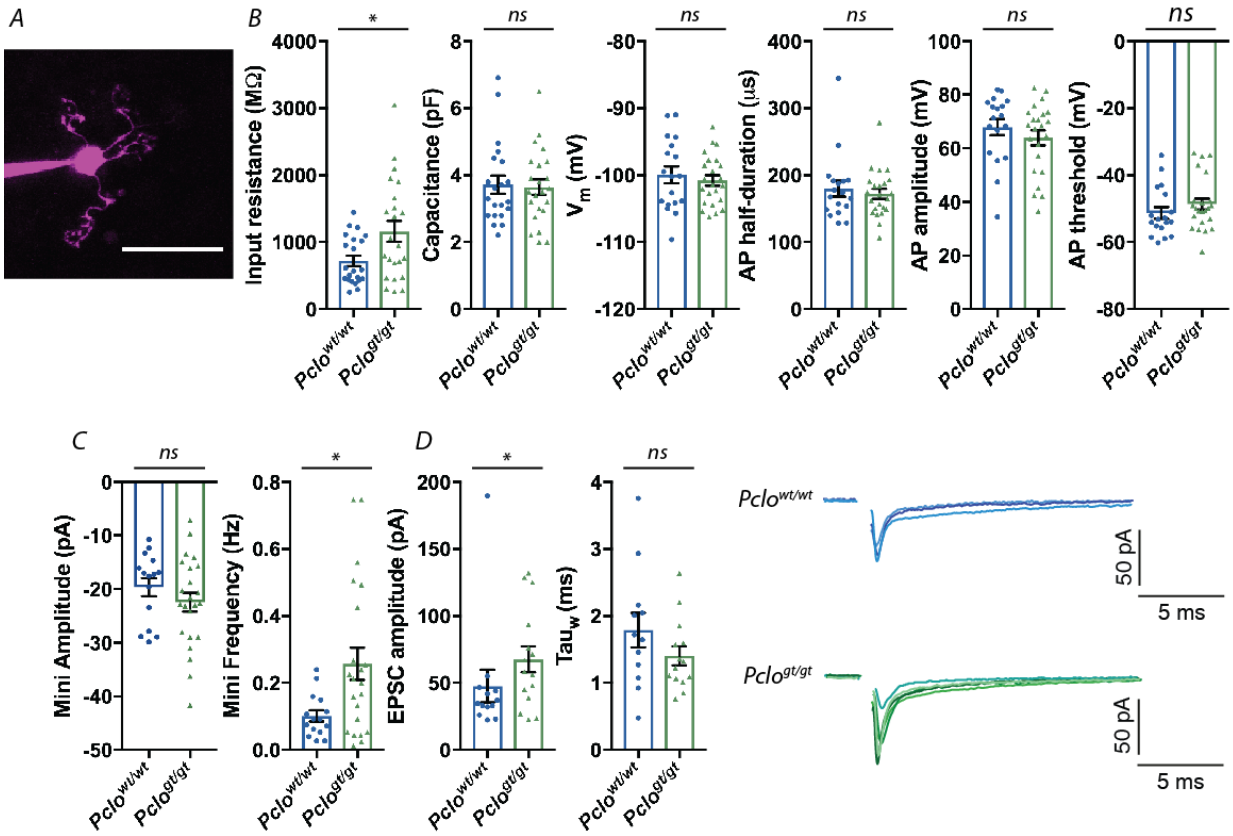

Figure 26: Physiological assessment of mossy fibre boutons

A) Example two-photon image of a cerebellar granule cell filled with ATTO dye from a *Pclo*$^{gt/gt}$ rat. B) Average data of biophysical properties of GCs for *Pclo*$^{wt/wt}$ and *Pclo*$^{gt/gt}$ rats. The input resistance of GCs was higher in *Pclo*$^{gt/gt}$ compared to *Pclo*$^{wt/wt}$ (*Pclo*$^{wt/wt}$ = 722.6 MΩ ± 76.24, n = 22 cells; *Pclo*$^{gt/gt}$ = 1160 MΩ ± 154.9, n = 23 cells; n = 3 rats per genotype; Mann-Whitney U test, $U = 165$, $p^* = 0.0462$). Whereas no differences were found in capacitance (*Pclo*$^{wt/wt}$ = 3.717 pF ± 0.269, n = 21 cells; *Pclo*$^{gt/gt}$ = 3.643 pF ± 0.231, n = 23 cells; n = 3 rats per genotype; Mann-Whitney U test, $U = 236.5$, $p = 0.912$), resting membrane potential (Vm) (*Pclo*$^{wt/wt}$ = -99.96 mV ± 1.261, n = 18 cells, *Pclo*$^{gt/gt}$ = -100.8 mV ± 0.786, n = 23 cells; n = 3 rats per genotype; Mann-Whitney U test, $U = 187$, $p = 0.612$), the half-duration of the action potential (*Pclo*$^{wt/wt}$ = 179.7 µs ± 11.84, n = 18 cells; *Pclo*$^{gt/gt}$ = 172.2 µs ± 7.366, n = 23 cells; n = 3 rats per genotype; Mann-Whitney U test, $U = 200$, $p = 0.866$), the amplitude of the action potential (*Pclo*$^{wt/wt}$ = 67.85 mV ± 3.016, n = 18 cells; *Pclo*$^{gt/gt}$ = 63.92 mV ± 2.761, n = 23 cells; n = 3 rats per genotype; Mann-Whitney U test, $U = 166$, $p = 0.291$) and the voltage threshold to elicit an action potential (*Pclo*$^{wt/wt}$ = -51.27 mV ± 1.748, n = 18 cells; *Pclo*$^{gt/gt}$ = -48.6 mV ± 1.659, n = 23 cells; n = 3 rats per genotype; Mann-Whitney U test, $U = 153$ $p = 0.162$). C) Miniature excitatory postsynaptic currents from *Pclo*$^{gt/gt}$ GCs were not different in their amplitude (*Pclo*$^{wt/wt}$ = -19.62 pA ± 1.682, n = 15 cells from 2 rats; *Pclo*$^{gt/gt}$ = -22.44 pA ± 1.765, n = 23 cells from 3 rats; Mann-Whitney U test, $U = 136$, $p = 0.286$) but in their frequency (*Pclo*$^{wt/wt}$ = 0.102 Hz ± 0.0167, n = 15 cells from 2 rats; *Pclo*$^{gt/gt}$ = 0.257 Hz ± 0.0481, n = 22 cells; from 3 rats; Mann-Whitney U test, $U = 98.5$, $p^* = 0.0392$). D) Excitatory postsynaptic currents from GCs measured after stimulation of single mossy fibres were increased in *Pclo*$^{gt/gt}$ compared to *Pclo*$^{wt/wt}$ (*Pclo*$^{wt/wt}$ = 47.58 pA ± 12.12, n = 13 cells; *Pclo*$^{gt/gt}$ = 67.62 pA ± 9.64, n = 15 cells; n = 3 rats per genotype; Mann-Whitney U test, $U = 52$, $p^* = 0.0356$), whereas the decay of the EPSC was not alerted (*Pclo*$^{wt/wt}$ = 1.79 ms ± 0.258, n = 12 cells; *Pclo*$^{gt/gt}$ = 1.404 ms ± 0.141, n = 14 cells; n = 3 rats per genotype; Mann-Whitney test U, $U = 60$, $p^* = 0.231$). Right hand panel: example traces of evoked EPSCs, as quantified in D), in response 1 Hz stimulation in the presence of 20 µM SR95531 and 40 µM D-(2R)-amino-5-phosphonovaleric acid (D-APV). Scale bar = 20 µm. Error bars represent SEM. Data points represent individual cells. Adapted from Falck et al. [46].

6.8 Behavioural and motor defects in *Pclo*$^{gt/gt}$ rats

The motor difficulties reported [42] in humans with PCH3 and the anatomical changes observed in the cerebellum and brainstem of rats lacking Piccolo predict altered motor function in these animals. To test this hypothesis, *Pclo*$^{wt/wt}$, *Pclo*$^{wt/gt}$ and *Pclo*$^{gt/gt}$ rats were monitored for their motor abilities. In rotarod tasks, *Pclo*$^{gt/gt}$ rat performance was significantly reduced compared to *Pclo*$^{wt/wt}$ and *Pclo*$^{wt/gt}$ rats (Figure 27A). Specifically, while *Pclo*$^{wt/wt}$ and *Pclo*$^{wt/gt}$ rats exhibited increasing performance levels regarding the ability to stay on the rotarod over time, *Pclo*$^{gt/gt}$ rats showed no indication of being able to adapt to the task. *Pclo*$^{gt/gt}$ rats were less adept at staying on the task apparatus once rod rotation was initiated (mean time at trial 16: *Pclo*$^{wt/wt}$ = 56.5 s; *Pclo*$^{wt/gt}$ = 68.75 s; *Pclo*$^{gt/gt}$ = 2.25 s) (Figure 27A, Table 3). Intriguingly, no differences in forelimb grip strength were scored between Piccolo genotypes (Figure 27B, Table 3), indicating that *Pclo*$^{gt/gt}$ rats showed impaired coordination.

In addition to deficits in motor ability, *Pclo*$^{gt/gt}$ rats displayed an increased frequency in front and rear foot stepping errors during ladder rung walking compared to *Pclo*$^{wt/wt}$ and *Pclo*$^{wt/gt}$ rats (mean forelimb error/step: *Pclo*$^{wt/wt}$ = 0.09; *Pclo*$^{wt/gt}$ = 0.148; *Pclo*$^{gt/gt}$ = 0.29, mean hindlimb error/step: *Pclo*$^{wt/wt}$ = 0.0563; *Pclo*$^{wt/gt}$ = 0.0663; *Pclo*$^{gt/gt}$ = 0.238) (Figure 27C, Table 3). In open field tests, no significant differences were recorded between *Pclo*$^{wt/wt}$, *Pclo*$^{wt/gt}$ and *Pclo*$^{gt/gt}$ rats for peripheral line crossing or self-grooming events (Figure 27D, Table 3). However, *Pclo*$^{gt/gt}$ rats displayed two- to three-fold decreases in peripheral rearing events compared to *Pclo*$^{wt/wt}$ and *Pclo*$^{wt/gt}$ animals (Figure 27D). Deficits in *Pclo*$^{gt/gt}$ rat performance during rotarod, ladder rung and open field tests in comparison to *Pclo*$^{wt/wt}$ and *Pclo*$^{wt/gt}$ (Figure 27A-D) reflected traits consistent with dysfunction in proprioceptive sensation and motor control [34].

Alongside traditional tests for motor coordination, we tested the behaviour of *Pclo*$^{wt/wt}$, *Pclo*$^{wt/gt}$ and *Pclo*$^{gt/gt}$ rats in a home cage setup, the OptiMan (Operator Independent Motor-analysis) system, where animals can be monitored without interference from experimenters. Rats were tagged with a radio frequency identification chip that allowed for tracking of locomotor activity while they were also required to complete an isometric pull task that requires precise and finely controlled movements. In the home cage, the *Pclo*$^{gt/gt}$ rats were more active and covered almost twice the distance than *Pclo*$^{wt/wt}$ rats (Figure 27E) during each measurement. In the isometric pull task, performance of *Pclo*$^{gt/gt}$ rats was significantly lower than the performance of *Pclo*$^{wt/wt}$ rats, quantified using four different force thresholds (mean success rate at 60g: *Pclo*$^{wt/wt}$ = 69.186; *Pclo*$^{wt/gt}$ = 70.409; *Pclo*$^{gt/gt}$ = 30.003) (Figure 27F). Taken together, *Pclo*$^{gt/gt}$ rats show clear motor deficits, very similar to symptoms seen in PCH3 patients [137].

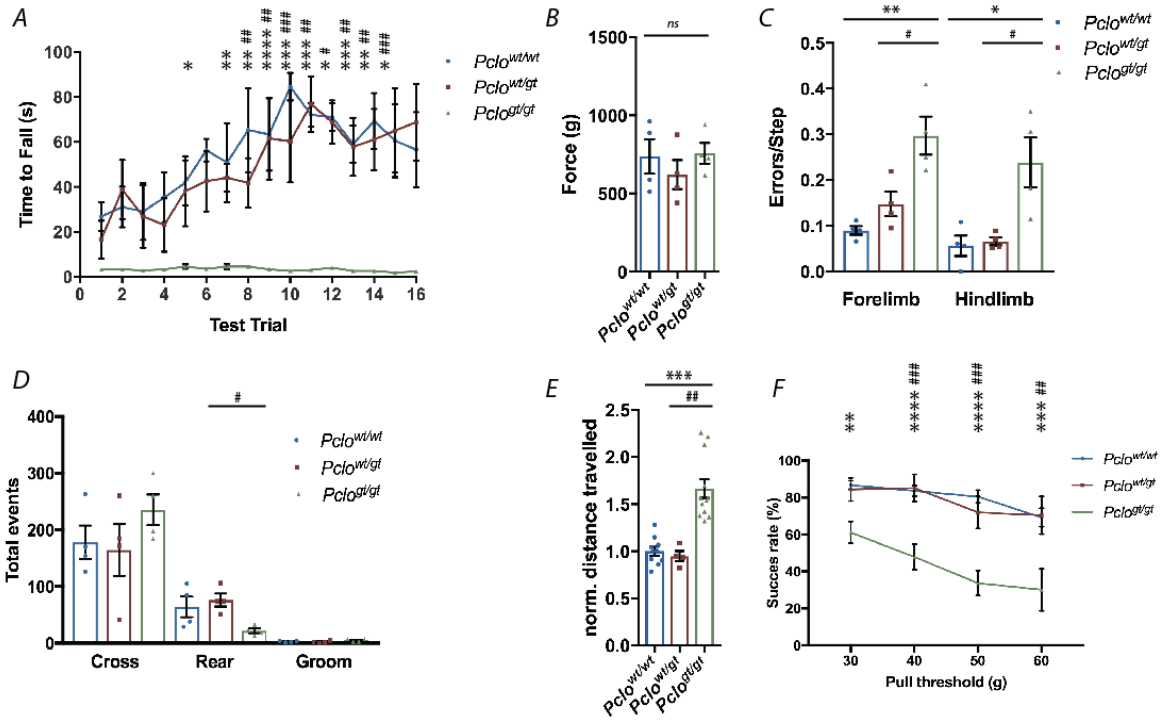

Figure 27: Behavioural outcome of Piccolo loss of function resembles PCH3 symptoms

A) Rotarod performance for *Pclo*$^{wt/wt}$, *Pclo*$^{wt/gt}$ and *Pclo*$^{gt/gt}$ rats for 16 trials over 4 days. *Pclo*$^{gt/gt}$ rats fell significantly faster than *Pclo*$^{wt/wt}$ on trials 6 and 8 and faster than both *Pclo*$^{wt/wt}$ and *Pclo*$^{wt/gt}$ on trials 9-16. B) Grip strength task for *Pclo*$^{wt/wt}$, *Pclo*$^{wt/gt}$ and *Pclo*$^{gt/gt}$ rats for 9 trials over 2 days. No differences were found for forelimb grip strength between the groups. C) Ladder walk task for *Pclo*$^{wt/wt}$, *Pclo*$^{wt/gt}$ and *Pclo*$^{gt/gt}$ rats for 3 trials over 1 day. *Pclo*$^{gt/gt}$ rats had a higher rate of stepping errors (ladder rung foot slips/misses) than *Pclo*$^{wt/wt}$ and *Pclo*$^{wt/gt}$ rats. D) Open field task for *Pclo*$^{wt/wt}$, *Pclo*$^{wt/gt}$ and *Pclo*$^{gt/gt}$ rats for 1 trial each over 1 day. *Pclo*$^{gt/gt}$ rats performed fewer rearing behaviours than *Pclo*$^{wt/wt}$ and significantly less than *Pclo*$^{wt/gt}$ rats in the perimeter sectors of the arena. Other behaviours such as crossing the open field and grooming were not different between the three groups. E). Locomotor activity of *Pclo*$^{wt/wt}$, *Pclo*$^{wt/gt}$ and *Pclo*$^{gt/gt}$ rats during the 12 h dark phase. *Pclo*$^{gt/gt}$ rats covered more than 50 % further distance than *Pclo*$^{wt/wt}$ and *Pclo*$^{wt/gt}$ rats. F) Performance of *Pclo*$^{wt/wt}$, *Pclo*$^{wt/gt}$ and *Pclo*$^{gt/gt}$ rats during the isometric pull-task (handle position 11 mm inside the cage). Only 4 out of 11 *Pclo*$^{gt/gt}$ rats succeeded at the 60 g force threshold and *Pclo*$^{gt/gt}$ rats pulled with a significantly lower success rate at all force thresholds as compared to *Pclo*$^{wt/wt}$ and *Pclo*$^{wt/gt}$. Error bars represent SEM. A-D and F: Data points represent individual rats; E: Data points are individual means over 15 nights. * = significance of difference between *Pclo*$^{wt/wt}$ and *Pclo*$^{gt/gt}$; # = significance of difference between *Pclo*$^{wt/wt}$ and *Pclo*$^{wt/gt}$. For statistical analysis see Table 3. Adapted from Falck et al. [46].

Behavioural test	trial/event	$Pclo^{wt/wt}$	n	$Pclo^{wt/gt}$	n	$Pclo^{gt/gt}$	n	*wt/wt* vs *wt/gt*	*wt/wt* vs *gt/gt*	1-way ANOVA
								(df), t value, p value	***(df), t value, p value***	
Rotarod performance:	1	26.75 ± 6.486	4	16.5 ± 8.431	4	3.25 ± 0.75	4	(144), 0.681, > 0.9999	(144), 1.561, > 0.9999	
time to fall (s)	2	3 ± 9.138	4	38.75 ± 13.231	4	3.25 ± 0.479	4	(144), 0.515,> 0.9999	(144), 1.843, > 0.9999	
	3	29 ±12.748	4	26.75 ± 13.949	4	2.75 ± 0.25	4	(144), 0.15, > 0.9999	(144), 1.744, > 0.9999	
	4	35.25 ± 11.25	4	23 ± 11.979	4	3.25 ± 0.479	4	(144), 0.814, > 0.9999	(144), 2.126, > 0.9999	
	5	41.75 ± 10.053	4	38 ± 15.647	4	4.5 ± 1.041	4	(144), 0.249, > 0.9999	(144), 2.474, 0.6963	
	6	56.25 s ± 5.023	4	42.5 ± 13.531	4	3.5 ± 0.5	4	(144), 0.1913, > 0.9999	(144), 3.504, 0.0293	
	7	50.75 ± 17.585	4	44 ± 6.205	4	4.5 ± 1.323	4	(144), 0.45, > 0.9999	(144), 3.072, 0.122	
	8	65.25 s ± 18.688	4	41.75 ± 11.048	4	4.5 s ± 0.957	4	(144), 1.561, > 0.9999	(144), 4.035, 0.0042	
	9	63.25 s ± 16.163	4	61.5 s ± 18.319	4	3.25 s ± 0.75	4	(144), 0.116, 0.0079	(144), 3.986, 0.0051	
	10	84.5 s ± 6.225	4	60.25 s ± 18.396	4	2.5 s ± 0.5	4	(144), 1.611, 0.0089	(144), 5.447, 0.0001	
	11	72 s ± 5.339	4	76.75 s ± 12.419	4	3 s ± 0.408	4	(144), 0.316, 0.001	(144), 4.583, 0.0005	
	12	71 s ± 6.178	4	68.75 s ± 9.681	4	4 s ± 0.707	4	(144), 0.15, 0.0015	(144), 4.451, 0.0008	
	13	59 s ± 8.297	4	57.75 s ± 12.99	4	2.5 s ± 0.5	4	(144), 0.083, 0.0164	(144), 3.753, 0.0121	
	14	69.25 s ± 12.479	4	61 s ± 13.638	4	2.5 s ± 0.645	4	(144), 0.548, 0.0074	(144), 4.434, 0.0009	
	15	60.5 s ± 16.297	4	65 s ± 18.757	4	1.75 s ± 0.479	4	(144), 0.3, 0.0022	(144), 3.903, 0.0070	
	16	56.5 s ± 16.775	4	68.75 s ± 17.109	4	2.25 s ± 0.25	4	(144), 0.814,0.009	(144), 3.604, 0.0207	
Grip strength task:force (g)		737.2 ± 109.9	4	621.2 ± 93.46	4	757.5 ± 66.74	4			$F(2,9) = 0.642, p = 0.549$
Ladder walk: FL errors/step		0.09 ± 0.00925	4	0.148 ± 0.0263	4	0.297 ± 0.0145	4	$p^{\#} = 0.0157$	$p^{**} = 0.002$	
Ladder walk: HL errors/step		0.0563 ± 0.0221	4	0.0663 ± 0.00877	4	0.238 ± 0.0543	4	$p^{\#} = 0.0186$	$p^{*} = 0.0135$	
Open field task:	Cross	178.3 ± 29.68	4	164.5 ± 45.51	4	235.5 ± 27.11	4	*p > 0.9999*	*p = 0.8337*	*F (2,9) = 1.154, p = 0.828*
total events	Rear	64.25 ± 18.31	4	76.25 ± 11.3	4	22 ± 4.203	4	*p > 0.9999*	*p = 0.1277*	*F (2,9) = 5.069, p = 0.0335*
	Groom	2.75 ± 0.75	4	2 ± 1.08	4	5 ± 1.155	4	*p > 0.9999*	*p = 0.4494*	*F (2,9)= 2.388, p = 0.1473*
norm. distance travelled		1 ± 0.046	10	0.948 ± 0.547	4	1.664 ± 0.099	12	*p > 0.9999*	$p^{***} = 0.0004$	$F(2, 23) = 22.68, p < 0.0001$
Pull-task:	30 g	86.722 ± 2.3	10	84.374 ± 6.324	4	61.044 ± 5.928	11	(78), 0.242, *p > 0.9999*	*(78), 3.578,* $p^{**} = 0.0018$	
force (g), success rate	40 g	83.603 ± 2.86	10	85.136 ± 7.373	4	47.804 ± 6.897	10	(78), 0.158, *p > 0.9999*	(78), 4.874, $p^{****} = 0.0001$	
	50 g	80.49 ± 3.442	10	71.93 ± 8.695	4	33.647 ± 6.802	10	(78), 0.881, *p > 0.9999*	(78), 6.377, $p^{****} = 0.0001$	
	60 g	69.19 ± 4.99	10	70.409 ± 10.181	3	30.003 ± 11.359	4	(78), 0.113, *p > 0.9999*	(78), 4.032, $p^{***} = 0.0004$	

Table 3: Supplementary statistical information supporting Figure 27
Mean, standard error of the mean (SEM), *F* values, *n* numbers, degrees of freedom (*df*), *t* and *p* values for behavioural data as depicted in Figure 27 .* = *p* value for difference between $Pclo^{wt/wt}$ and $Pclo^{gt/gt}$; # = p value for difference between $Pclo^{wt/wt}$ and $Pclo^{wt/gt}$. Adapted from Falck et al. [46].

6.9 Exploring mechanisms of synapse maturation: Wnt signalling in *Pclo*$^{gt/gt}$

Because Wnt signalling plays a role in the size and maturation of MF synapses [4, 63, 108], we wanted to investigate whether Wnt signalling could be affected in *Pclo*$^{gt/gt}$ neurones. This was accomplished by culturing pontine explants that extend axons and form MF boutons. In this system, one can readily manipulate growth conditions, for example, by the addition of growth factors, chemoattractants or chemorepellents [94, 136]. Wnt-7a is usually released from cerebellar granule cells and has been found to promote the stabilisation of microtubules, axonal growth and the size of growth cones [4, 63]. We thus grew pontine explants from *Pclo*$^{wt/wt}$ or *Pclo*$^{gt/gt}$ P0-P1 rat pups on laminin-coated slides in culture medium either with or without Wnt-7a.

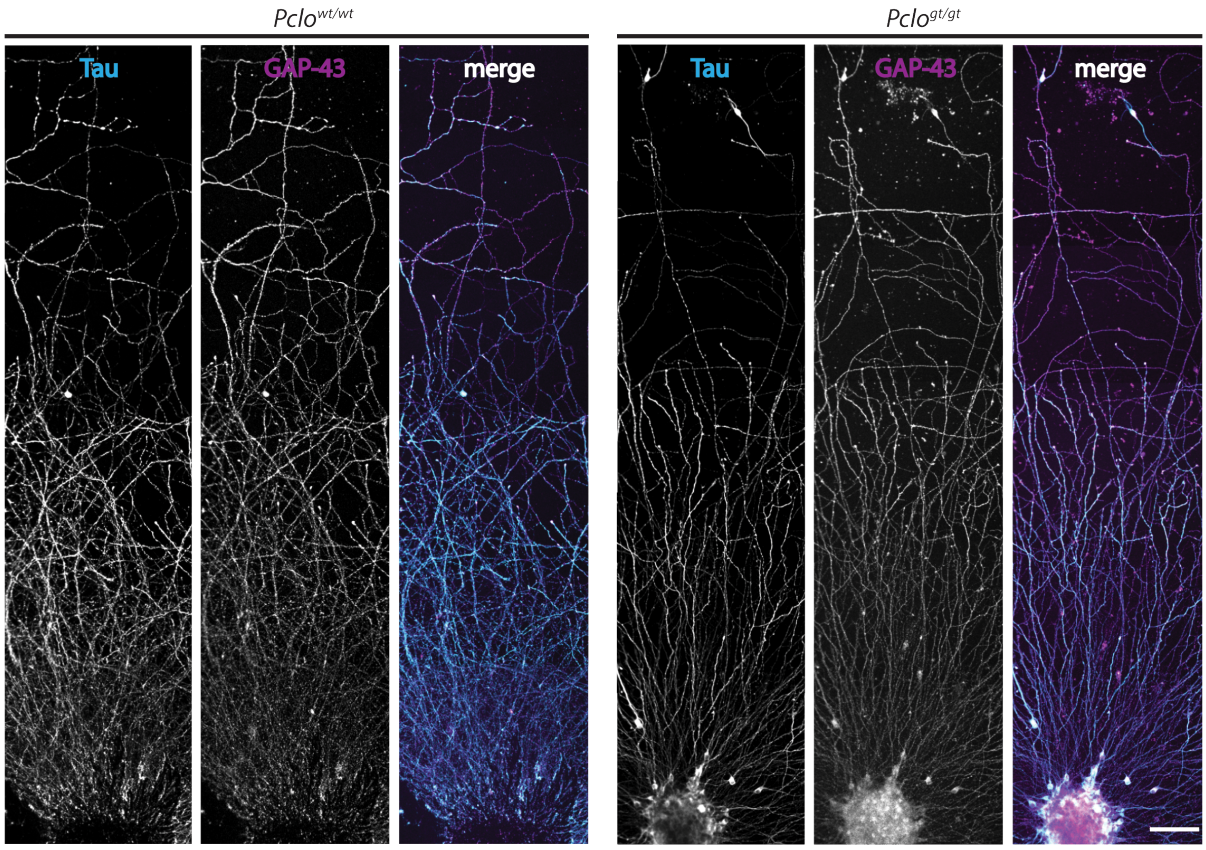

Figure 28: both *Pclo*$^{wt/wt}$ and *Pclo*$^{gt/gt}$ pontine explants are able to grow extensive processes in normal neurobasal medium

Low magnification images of pontine neurites at 3 DIV, demonstrating that the explant culture technique is successful. Tau staining indicates that outgrowths are axonic and GAP-43 labels developing growth cones. Scale bar = 50 µm.

To study the impact of Wnt-7a on MF growth cones, explants of the pontine nuclei were plated onto PLL- and laminin-coated coverslips and the extent of axonal growth evaluated in *Pclo*$^{wt/wt}$ and *Pclo*$^{gt/gt}$ derived neurones after 3 DIV (Figure 28). After fixation, neurones were stained with Tau to visualise axons and with GAP-43, which is highly expressed in neuronal growth cones [6]. Representative images of these neurones reveal that axons and growth cones are readily formed by

neurones from both geneotypes (Figure 28). At 1 DIV, analysis of growth cones revealed that whilst there were no differences in the size of growth cones between *Pclo*$^{wt/wt}$ and *Pclo*$^{gt/gt}$ explants, *Pclo*$^{gt/gt}$ growth cones failed to increase their area upon treatment with Wnt-7a compared to *Pclo*$^{wt/wt}$ growth cones, which increase their area significantly (mean area normalised to *Pclo*$^{wt/wt}$: *Pclo*$^{wt/wt}$ = 1; *Pclo*$^{wt/wt}$ + Wnt-7a = 1.548; *Pclo*$^{gt/gt}$ = 0.932, *Pclo*$^{gt/gt}$ + Wnt-7a = 0.866) (Figure 28). In terms of growth gone complexity, calculated by the perimeter^2/area of growth cones, no significant differences were found between conditions. There was nonetheless a trend toward *Pclo*$^{wt/wt}$ growth cones being more complex than *Pclo*$^{gt/gt}$ growth cones, regardless of whether they were treated with Wnt-7a or not (Figure 29C). These data suggest that factors other than Piccolo or Wnt-7a are necessary to induce growth cone complexity in our system. Importantly, the inability of *Pclo*$^{gt/gt}$ growth cones to change their size following the addition of Wnt-7a indicates that growth cones lacking Piccolo are less responsive to Wnt-7a, which may contribute to the defects in maturation of MF in the granule cell layer of the cerebellum. Additional experiments will be necessary to solve this important question.

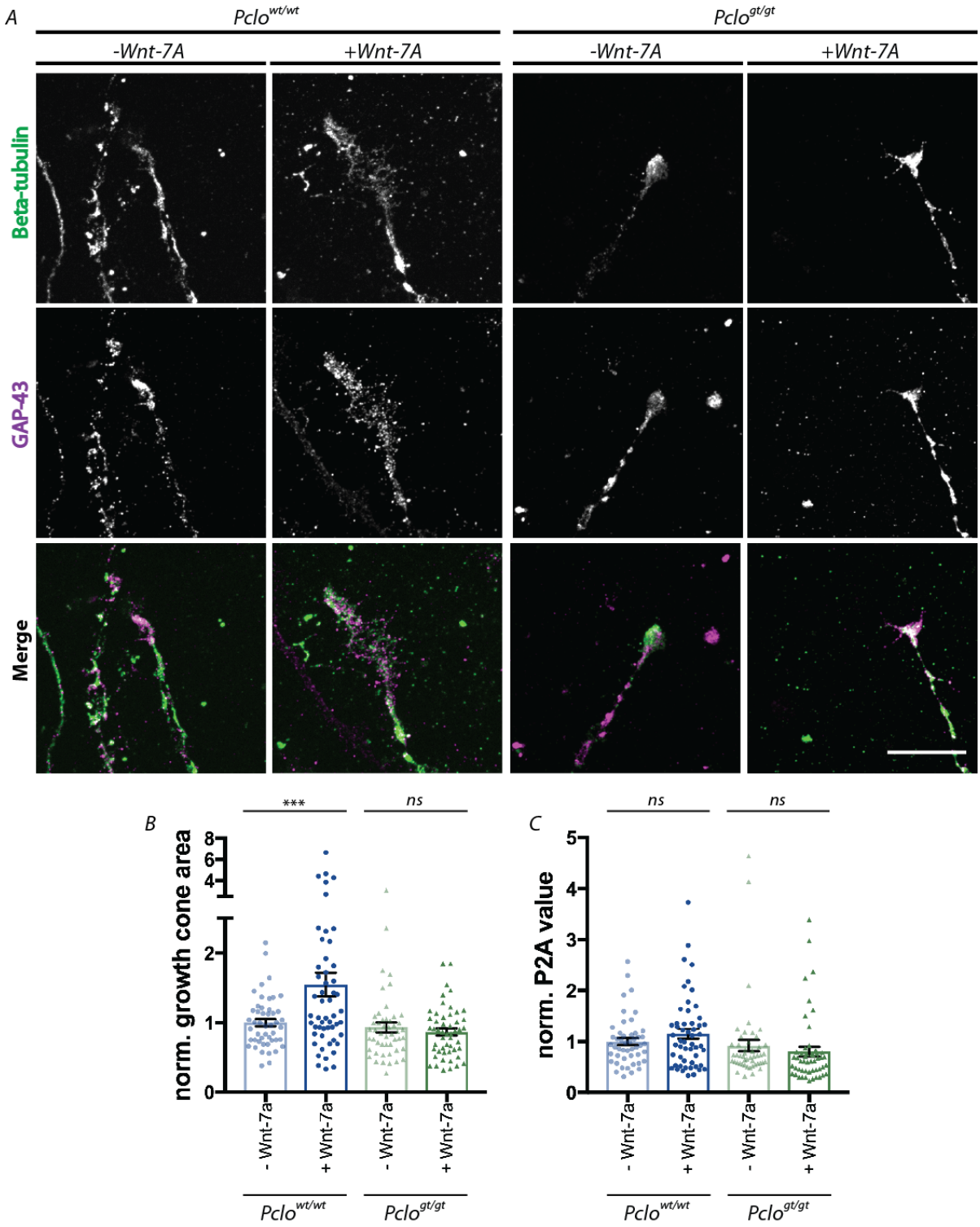

Figure 29: *Pclo*$^{wt/wt}$ but not *Pclo*$^{gt/gt}$ growth cones respond to treatment with Wnt-7a

A) Example images of MF growth cones from pontine explants stained with antibodies against GAP-43 to label growth cones and Beta-tubulin to label microtubules. *Pclo*$^{wt/wt}$ growth cones treated with Wnt-7a larger and more complex than untreated *Pclo*$^{wt/wt}$ growth cones and *Pclo*$^{gt/gt}$ growth cones. B) Quantification of growth cone area (normalised to *Pclo*$^{wt/wt}$) of *Pclo*$^{wt/wt}$ and *Pclo*$^{gt/gt}$ pontine explants untreated or treated with Wnt-7a. *Pclo*$^{wt/wt}$ growth cones increase in size when treated with Wnt-7a but *Pclo*$^{gt/gt}$ do not show a change (*Pclo*$^{wt/wt}$ = 1 ± 0.0534, n = 48 growth cones; *Pclo*$^{wt/wt}$ + Wnt-7a = 1.548 ± 0.169, n = 53 growth cones; *Pclo*$^{gt/gt}$ = 0.932 ± 0.0711, n 49 growth cones; *Pclo*$^{gt/gt}$ + Wnt-7a = 0.866 ± 0.0511, n = 51 growth cones; 3 independent experiments, 2-way ANOVA, *Pclo*$^{wt/wt}$ treated vs. untreated (197) $t = 3.794$, $p^{***} = 0.0004$; *Pclo*$^{gt/gt}$ treated vs. untreated (197) $t = 0.457$, $p = 0.877$). C) Quantification of normalised growth cone complexity of *Pclo*$^{wt/wt}$ and

Pclo$^{gt/gt}$ pontine explants untreated or treated with Wnt-7a. No significant changes were observed across conditions (*Pclo*$^{wt/wt}$ = 1 a.u. ± 0.0689, n = 48 growth cones; *Pclo*$^{wt/wt}$ + Wnt-7a = 1.52 ± 0.0967, n = 53 growth cones; *Pclo*$^{gt/gt}$ = 0.921 ± 0.113, n = 49 growth cones; *Pclo*$^{gt/gt}$ + Wnt-7a = 0.801 ± 0.0942, n = 51 growth cones; 3 independent experiments, 2-way ANOVA, *Pclo*$^{wt/wt}$ treated vs. untreated (197) $t = 1.135$, $p = 0.449$; *Pclo*$^{gt/gt}$ treated vs. untreated (197) $t = 0.882$, $p = 0.615$). Scale bar = 20. Error bars represent SEM. Data points represent individual growth cones.

7. Discussion

We sought out to determine the function of Piccolo in the brain and thereby its role in the development of diseases such as PCH3 based on characterisation of the *Pclo*$^{gt/gt}$ rat. Our study demonstrates that Piccolo LOF causes alterations in brain anatomy. In particular, the cerebrum, pons, brainstem and cerebellum are severely reduced in size. Changes in brain anatomy are associated with reductions in cerebellar and pontine cell numbers and perturbations in cerebellar CF and MF afferents. Said perturbations are predicted to adversely affect cerebellar function, supported by changes in synaptic transmission and motor control and the presence of seizures [116]. Interestingly, the changes in brain morphology resemble changes in children with PCH3, recently linked to a SNP in the *PCLO* gene [5]. In addition to brain atrophy, patients with PCH3 display cognitive and motor deficits as well as seizures.

7.1 Piccolo genetrap mutagenesis: effect on protein expression and brain anatomy

Despite its large size and multiple binding domains, relatively little is known about the active zone protein Piccolo. Thus far, due to its size and multiple isoforms, genetic manipulation has been difficult and studies have relied on shRNAs or partial knockout, which yielded considerably mild phenotypes [104, 124, 182]. By utilising the genetrap mutagenesis technique, Medrano and colleagues [116] were able to eliminate the majority of the protein and its isoforms, which can be visualised by western blotting and immunostaining of tissue (Figure 10).

Upon first inspection, *Pclo*$^{gt/gt}$ pups are smaller than their *Pclo*$^{wt/wt}$ littermates, but their brains are the same weight. However, as these rats develop, *Pclo*$^{gt/gt}$ brains fail to increase in size and weight at the same rate as *Pclo*$^{wt/wt}$. By three months, *Pclo*$^{gt/gt}$ rats are lacking in body size (data not shown), brain size and brain weight (Figure 11).

Considering that *Pclo*$^{gt/gt}$ pups are smaller at birth and this trait continues through to adulthood, it is possible that hormonal regulation of growth - in terms of both body and brain weight - could be affected in *Pclo*$^{gt/gt}$ [116]. Since the cerebellum develops postnatally, it is perhaps more vulnerable to deficiencies in growth factors or hormones than other brain regions that develop in the womb and could receive these factors from the mother.

7.2 Piccolo loss of function leads to a reduction in PCH3-affected brain regions

A remarkable feature of *Pclo*$^{gt/gt}$ brains is the cerebellum; along with an overall loss in brain volume, the cerebellum is disproportionately smaller than the rest of the brain (Figure 11). Because loss in brain volume is a phenotype of PCH3, we looked closer at the specific areas affected in this disease: the cerebral cortex, the pontine nucleus and the cerebellum. Like PCH3 patients, *Pclo*$^{gt/gt}$ rats have a

smaller cortex, a dramatically smaller pons and a thinning of both the molecular layer and the granule cell layer (Figure 13) [5]. The Purkinje cells in the Purkinje cell layer are more tightly packed together, whilst the densities of granule cells and pontine neurones (PNs) remain the same for *Pclo*$^{wt/wt}$ and *Pclo*$^{gt/gt}$, implying an overall loss of GCs and PNs in the brains of *Pclo*$^{gt/gt}$ rats (Figures 12 and 13). Bergmann glia arrangement appears to be normal in *Pclo*$^{gt/gt}$ (Figure 14).

Concerning GC and PN numbers, there are a number of signalling factors to consider. Math1 is essential for proper development of members of the proprioceptive pathway including GCs and PNs. Interestingly, mice lacking Math1 are born without a cerebellar GCL, pontine nucleus nor inner ear hair cells [13], as migration from the rhombic lip seems to require Math1. It has also been shown that MF precerebellar nuclei are reliant on Math1 whereas those derived from the inferior olive are not [185]. The affected brain regions in both Math1 mutants and *Pclo*$^{gt/gt}$ indicate that the number of Math1 positive cells migrating from the rhombic lip in *Pclo*$^{gt/gt}$ could be somehow affected, yet how these proteins might interact remains ambiguous.

GCs arise from the rhombic lip and migrate to the external granule cell layer, where they proliferate to form the most abundant cell population in the brain. A number of mitogenic pathways are involved in this expansion of cells, which then exit the cell cycle and migrate on Bergmann glia fibres to the internal granule cell layer, extending a parallel fibre which forms synapses with distal PC dendrites [106]. Whilst a thinning of the ML could be explained by a reduction in PF synapses - caused by a lower number of GCs - the reason for the loss in GC numbers remains enigmatic.

Canonical Wnt signalling increases proliferation of multipotent neural stem cells (NSCs) [134], which give rise to the majority of neurone types in the cerebellum and glia whereas GC proliferation in the cerebellum is regulated by the morphogenic factor Sonic hedgehog (Shh). The precerebellar progenitor pools within the rhombic lip that give rise to MF precerebellar neurones have a high Wnt1 expression, whereas progenitors that differentiate into climbing fibre precerebellar neurones have low Wnt1 expression [102], again demonstrating the existence of different mechanisms involved in the development of different afferents into the cerebellum. For example, Shh is secreted by PCs during postnatal development and is necessary for GC generation *in vivo* [192]; interrupting the Shh pathway leads to a loss of GC precursors, a reduction in foliation and cerebellar hypoplasia [33]. Shh also promotes Bergmann glia proliferation, which is essential to provide support to GCs during their radial migration from the EGL to the IGL. Other factors controlling the number of GCs in the cerebellum include the Notch signalling proteins, which are expressed by GCs during proliferation and activate the same signalling pathway as Shh in order to increase the pool of GCs in the EGL [165]. Interestingly, Wnts and Shh are upregulated in some cases of medullablastoma [106] - a common pediatric cancer consisting of cells very closely resembling GCs and GC precursors - and pontine glioma [122], highlighting comparable mechanisms of growth and proliferation in the two cell populations.

How Piccolo loss could influence these signalling pathways is unclear; although alterations of neuronal gene expression, a consequence of Piccolo LOF [82, 87, 116], could contribute to the loss of GCs as a downstream effect. Further studies are needed to resolve this mechanism, which could give hints at those implicated in PCH3. The architecture of *Pclo*$^{gt/gt}$ rats brains mirrors the change of brain volume in patients - in the GCL as well as the cortex and pons, paired with an expansion of ventricular size - indicating that *Pclo*$^{gt/gt}$ rats could be used as a model to investigate further the loss of these brain regions.

An important consideration in the discussion of these data is the role of hormones in the development of the cerebellum. Piccolo is strongly expressed in endocrine tissues such as the thyroid and pituitary glands [174] and RNA sequencing (RNAseq) analysis of *Pclo*$^{gt/gt}$ revealed that genes involved in hormonal secretion are downregulated [116]. Perinatal hypothyroidism arrests the development of the cerebellum and mouse models show a severe reduction in cerebellar volume. This is paired with a reduction in PC dendritic branching and loss of PFs, as well as a delay in GC migration from the EGL to the IGL [99, 106]. Whilst we do not observe attenuation of PC dendritic branching (Figure 13) or a build up of GCs in the EGL, we do see a reduction in the overall size of the cerebellum and a thinner ML, implying less PFs. We also observe a persistence of olivocerebellar projections (Figure 20), as in cases of hypothyroidism. Hajos et al. [61] found that, as well as delay in translocation of CFs from the PC soma to the dendritic tree, MFs are smaller in size in thyroid deficient rats. These smaller MFs had a similar SV density to control rats resulting in a reduced number of SVs per terminal, comparable to that observed in *Pclo*$^{gt/gt}$ (Figures 24 and 25). It appears that thyroid deficiency affects the synaptic organisation of the cerebellar circuit, which fails to exit the immature state with dominating CF-PC synapses over MF-PC. This could be due to the delay in arrival of GCs to the IGL, as they are responsible for secreting a number of trophic and signalling factors to induce cerebellar maturation (see chapter 7.4.2). It would therefore be interesting to track the timing of GC migration from the EGL to IGL in *Pclo*$^{gt/gt}$ rats in the future.

Timely convergence of pathways involved in cerebellar development is critical for proper formation and growth. The cerebellar and pontine nuclei phenotype in *Pclo*$^{gt/gt}$ and PCH3 is remarkable, though it is not clear exactly how Piccolo LOF is causative. Other precerebellar nuclei such as those in the brainstem or the spinal cord were not investigated in this study. It would be very interesting to see if those nuclei also suffer from a loss of cells or if this phenomenon is specific to the pons. Furthermore, investigation into previous studies suggests that loss of cells might somehow be mediated by signalling factors such as Shh, Notch or Math1, or that its role in the endocrine system could have an effect on cerebellar development. Further studies are required to investigate the role of Piccolo in the cellular mechanism of this phenotype.

7.3 Morphological analysis: cell properties, layers and distribution in *Pclo*$^{gt/gt}$ cerebella

Because both PCH3 patients and *Pclo*$^{gt/gt}$ rats seem to share a developmental phenotype, we sought to visualise neurones in the adult brain in order to compare them to *Pclo*$^{wt/wt}$ neurones. Taking an exploratory approach, we utilised the Golgi technique to investigate cell properties such as branching and layering in *Pclo*$^{gt/gt}$ and *Pclo*$^{wt/wt}$ brains.

Initial examination revealed that there are no overt differences between *Pclo*$^{gt/gt}$ and *Pclo*$^{wt/wt}$ in terms of layer formation and dendritic branching in the hippocampus, cortex and the cerebellum (Figures 15-17). A closer inspection and Sholl analysis of principle cells of the hippocampus after Neurolucida reconstruction also revealed no changes in dendrite arborisation. Here, *Pclo*$^{gt/gt}$ and *Pclo*$^{wt/wt}$ brains both displayed effective layer formation and dendritic branching. This is not surprising as Piccolo is a presynaptic active zone protein; therefore, we focused our research on the presynapse and networks of the cerebellum.

7.4 Piccolo loss of function alters cerebellar networks and synapse structure

As Piccolo is expressed at the presynaptic active zone, we were most interested to investigate how Piccolo LOF might affect different synapse subtypes in the cerebellum and whether this had an effect on cerebellar circuitry.

We first looked for gross deficiencies in synapse distribution and the alignment of pre- and postsynaptic markers. Piccolo is strongly expressed throughout the ML of the cerebellum [23]; however, we observed no overt differences between *Pclo*$^{wt/wt}$ and *Pclo*$^{gt/gt}$ other than the aforementioned thinning of the ML in *Pclo*$^{gt/gt}$ (Figure 13). It seems that PFs reach the ML and PCs and/or ML interneurones express postsynaptic density protein such as neuroligins. In the GCL, however, MF boutons were severely reduced in size in *Pclo*$^{gt/gt}$ (Figure 18). Inhibitory synapses in the ML and GCL did not seem to be affected in such a dramatic fashion (Figure 19).

To investigate these features in more detail, we examined the two excitatory afferents to the cerebellum: CFs projecting from the inferior olive onto the proximal dendrites of PCs and MFs which arrive from the brain stem, spinal cord and the pontine nucleus to form glomerular rosettes with GCs and transmit signals to the distal branches of PCs via PFs of GCs.

7.4.1 Hyperinnervation of Purkinje cells by climbing fibres in *Pclo*$^{gt/gt}$ cerebella

In the ML of *Pclo*$^{gt/gt}$ cerebella, CF morphology and arrangement appear to be normal, though a higher innervation of PC dendrites by CFs can be observed (Figure 20). It should be noted that PCs in the *Pclo*$^{gt/gt}$ ML are more closely packed together, however, there are important alternative hypotheses to consider. The hyperinnervation of CFs could be due to homeostatic changes to the network, such as

heterosynaptic competition with PFs for PC dendrite territory [69, 83]. During early development, PCs are innervated by multiple CFs that synapse around PC somata and form perinuclear nests [71, 188]. In the early phase of synapse elimination, functional differentiation causes homosynaptic competition between somatic synapses to become the one "winner" CF [69]. Said CFs then translocate up the PC dendritic tree to form a one CF to one PC connection ratio, whilst the remaining "loser" synapses are pruned away. Subsequently, during the late phase of CF elimination, refinement of CF to PC synapses is achieved via heterosynaptic competition between CFs and granule cell PFs for PC dendrite territory and requires proper function of PF to PC synaptic activity in order to drive pruning of weaker CFs that cannot compete with PFs [11, 71, 188]. Interestingly, mutant mice missing PF receptor components Gluδ2 or mGluR1 show similar CF innervation abnormalities as we see in *Pclo*$^{gt/gt}$ cerebella [72, 83, 84] and furthermore, blocking NMDA receptors which are abundantly expressed on MF terminals also leads to defects in the elimination of CFs [93], demonstrating the need for activity of precerebellar neurones via MFs and therefore PFs to maintain heterosynaptic competition between CFs and PFs.

Taken together, we hypothesise that Piccolo LOF could lead to less NT release from MF synapses, which in turn could cause a shift in heterosynaptic competition and cause hyperinnervation of CFs.

7.4.2 *Pclo*$^{gt/gt}$ cerebella have smaller and less mature mossy fibres

As discussed, our study revealed that pontine nuclei were dramatically decreased in size in *Pclo*$^{gt/gt}$ animals (Figure 12). In primates the pons provides over 50 % of MFs [178] and the smaller size of the pons suggests a net reduction in MF input into the cerebellum that appears to correspond to a reduced number of GCs (Figure 13). The number of MF glomeruli per area of the GCL is the same for *Pclo*$^{wt/wt}$ and *Pclo*$^{gt/gt}$. However, the size of individual MF boutons is dramatically reduced in *Pclo*$^{gt/gt}$ (Figures 18, 21 and 22). At the ultrastructural level, EM studies revealed that MF glomeruli are smaller and less complex; furthermore, the number of AZs per μm of bouton perimeter and the density of SVs within each remain the same, indicating that each bouton has less AZs and SVs in total (Figures 24 and 25). Furthermore, $GABA_A$ α6 subunit expression is reduced (Figure 23) [116] in the *Pclo*$^{gt/gt}$ GCL.

Electron micrographs also demonstrate what could be disturbed synaptic integrity in *Pclo*$^{gt/gt}$ MF boutons with more CCVs being present (Figure 25), suggesting that the loss of Piccolo may also affect SV recycling. These observations concur with recent findings by Ackermann et al. [2], which revealed that Piccolo LOF had a dramatic effect on the recycling of SV proteins through a block in the formation of early endosomes from endocytic vesicles, due to defects in the activation of Rab5 via a Piccolo-dependent synaptic loss of Pra1. Although beyond the current study, it is likely that this endocytic defect in the recycling of SV proteins could also contribute to altered size and function of MF synapses, especially given their high frequency transmission and therefore need for high SV turnover [22]. Synapses with high SV turnover, such as the Calyx of Held and endbulb of Held in the

auditory system, are also affected by Piccolo LOF [21, 50]. In the visual system, however, a splice variant of Piccolo, Piccolino, is responsible for the assembly and maturation of plate-shaped rod photoreceptor ribbon synapses [139, 140, 193], a specialised sensory synapse that docks and primes hundreds of SVs in preparation for the fast, tonic release required over long periods of time in response to varying intensities of light. This synapse requires robust and dynamic SV release machinery [114, 173]. These studies highlight a role for Piccolo and its splice variants at synapses with a high demand for SV recycling, amplifying defects observed in hippocampal synapses by Ackermann et al. [2].

By several measures mentioned above, it would appear that the MF glomeruli are also less mature. Key regulators of MF maturation are members of the Wnt family, a group of target-derived factors that accelerate neuronal maturation or induce synapse formation [152, 181]. Interestingly, mouse cerebellar MFs lacking Wnt-7a show a similar reduction in MF size and complexity as observed in *Pclo*$^{gt/gt}$ (Figure 24) [63]. It is important to note that in the case of Wnt-7a loss, MF synapse size catches up to wildtype size by age P15, which points to a lag in maturation and does not seem to be the case in *Pclo*$^{gt/gt}$. In Wnt-7a mutant animals, there are a number of other Wnt ligands remaining, for example Wnt-7b, which could rescue the deficit in Wnt-7a and therefore the phenotype. We hypothesise that a component of the Wnt signalling cascade downstream of Wnt-7a binding to the frizzled receptor could be impaired in *Pclo*$^{gt/gt}$.

Double knockout of Dv1, a downstream target of Wnt [151], and Wnt-7a also shows a reduction in MF cluster size, which is more persistent than Wnt-7a KO alone, indicating that presynaptic Dvl1 is a necessary step in the Wnt signalling cascade and underscoring the importance of these proteins for MF-GC synapse formation [4]. Like Dvl, Piccolo is located at the AZ of the presynaptic terminal and regulates F-Actin assembly and synaptic transmission through its interaction with Daam1 and Profilin [179]. Daam1 is a formin and a known regulator/interaction partner of Dvl [54]. It is thus possible that, in the absence of Piccolo, proper Wnt signalling is disrupted, altering the maturation of MF-GC synapses. Indeed, analysis of *Pclo*$^{gt/gt}$ transcripts by Medrano and colleagues [116] reveals that Wnt expression is reduced at 6 months of age. Moreover, Wnt-3a was found to increase Piccolo RNA and protein levels in mouse hippocampal neurones [113], supporting a relationship between Piccolo and Wnt ligands (see chapter 7.6). Thus, there appears to be at least two possible mechanisms that could contribute to smaller MF boutons in *Pclo*$^{gt/gt}$ rats: defects in SV recycling and Wnt signalling. Clearly further studies are needed to explore these options.

Another target-derived factor, FGF-22, has been implicated in the formation and differentiation of MF boutons; it is expressed by GCs during synapse formation and its receptor (FGFR) is expressed on MF growth cones [175]. FGF-22 also induces varicosities of synaptic vesicle proteins and blockade of the receptor ablates these varicosities as well as the number and size of MF glomeruli [175]. As FGF-22 was shown to be one of many organisers of MF synaptic maturation and

differentiation, it is plausible that this mechanism could also be impaired in *Pclo*$^{gt/gt}$ rats. Whilst there are no reported links between FGF-22 and Piccolo, the signalling cascade of another growth factor receptor, the epidermal growth factor receptor (EGFR), is promoted by Piccolo [201]. Both receptors are transmembrane receptor tyrosine kinases that promote cell survival, proliferation and differentiation and stimulate a similar intracellular signalling cascade following ligand-activated dimerization [154]. It would therefore be interesting to investigate FGF-22 and its role in synaptic differentiation in *Pclo*$^{gt/gt}$ rats.

The MF synapse in the cerebellum is the hardest hit by the loss of functional Piccolo. The reason for this specificity remains unclear, but we can speculate that defects in MF maturation, mediated by Wnt signalling cascades, and/or defects in SV turnover, which is elevated in the MF synapse compared to principle cells of the hippocampus or the cortex, could be causative for the MF phenotype.

7.4.3 Changes in $GABA_A$ α6 subunit expression at *Pclo*$^{gt/gt}$ mossy fibres

GCs receive inhibitory modulation from Golgi cells [44] and it is well appreciated that $GABA_A$ receptors at the MF synapse contain α6 subunits [130], which are first expressed during development after migration from the EGL to the IGL as GCs become innervated by MFs and Golgi cells [117]. Intriguingly, *Pclo*$^{gt/gt}$ rats display a reduced expression of the $GABA_A$α6 subunit at MFs (Figure 23). This is in line with findings from Medrano et al. [116], who performed RNAseq on *Pclo*$^{gt/gt}$ rats and found a severe reduction in $GABA_A$α6 subunit gene expression. At present, it is unclear why levels of these subunits are reduced. One possibility is that it reflects a homeostatic change within cerebellar circuitry. This concept is supported by electrophysiological data showing that the input resistance of GCs is higher as is mEPSC frequency and EPSC amplitudes (Figure 26, see chapter 7.5). This condition might arise to compensate for the smaller MF terminals reaching the GCL, which could also have weaker output properties. Indeed, in the absence of AMPA receptor activation, $GABA_A$α6 expression is reduced via an attenuation of brain-derived neurotrophic factor (BDNF) [133, 171], which is necessary to promote the formation of GABAergic synapses onto GCs [27]. MF boutons have also been shown to reduce functional NMDA receptors in GCs depleted of GABAergic inhibition [187], demonstrating the plasticity of the MF-GC synapse. Though a role of Piccolo in the secretion of BDNF has not been investigated, the expression of Bassoon, which shares significant functional redundancy with Piccolo, is linked to presynaptic levels of BDNF [77]. In this regard, the remaining Bassoon protein could suppress BDNF secretion in MF terminals, altering maturation of the glomeruli and $GABA_A$α6 expression. Knockout models of $GABA_A$α6 [80] do not display PCH3 phenotypes or alterations in the anatomy of the cerebellum. Therefore, $GABA_A$α6 downregulation can be attributed to Piccolo loss, but not causal for the PCH3 phenotypes.

The reduction in excitation from *Pclo*$^{gt/gt}$ MFs seems to affect the cerebellar network, causing the downregulation of $GABA_A\alpha6$ as an attempt to restore the excitation/inhibition balance at these synapses. Taken together, these data suggest the entire cerebellar circuit is immature, favouring CF over MF innervation of PCs and a downregulation of $GABA_A\alpha6$ subunits.

7.5 Piccolo loss of function changes properties of synaptic transmission

Histological and EM studies revealed remarkable changes in cerebellar cortex size and synapse structure, with indications of defects in the SV cycle. We were therefore interested in exploring the biophysical properties of these synapses.

Whole-cell patch clamp recordings were made form cerebellar granule cells, whilst MF axons were stimulated extracellularly. Intrinsic properties of GCs as well as synaptic transmission were investigated. We found that GCs from *Pclo*$^{gt/gt}$ cerebellar slices displayed an increase in input resistance, paired with an increase in evoked EPSC amplitude and an increase in spontaneous EPSC frequency compared to slices from *Pclo*$^{wt/wt}$ rats (Figure 26).

Electrophysiological recordings revealed that GCs in *Pclo*$^{gt/gt}$ cerebella are more excitable, demonstrated by an increased input resistance, which could therefore be responsible for the increased evoked EPSC. A decrease in open ion channels can also lead to an increased input resistance. Although we investigated the main $GABA_A$ receptor subunit present at the MF, we did not investigate other receptors such as AMPA and NMDA receptors, which are all present and could be changed in *Pclo*$^{gt/gt}$ rats [36]. Whilst it is surprising that these smaller, immature MF synapses are generating an increased response in GCs, we can look to mechanisms of homeostatic plasticity to explain this phenomenon. Biological systems exist within a narrow range of physiological parameters that must be tightly controlled, such as core body temperature or blood pressure. Homeostasis of neurones is essential to avoid epileptic activity or complete silencing of a network, and each cell is required to maintain excitability within a certain range [19]. In the GCL, for example, weak MF inputs lead to an increase GC intrinsic excitability [10] in order to boost the signal and maintain excitability of the GC. This is likely to be the case in *Pclo*$^{gt/gt}$ rats, as MFs contacting GCs contain less SVs which could lead to reduced excitatory input.

As mentioned above, the $GABA_A\alpha6$ subunit is reduced in the *Pclo*$^{gt/gt}$ GCL, indicating a homeostatic downregulation of inhibitory modulation by Golgi cells. Similarly, the *stargazer* mutant, in which MFs are electrically silent due to deficiencies in AMPA receptor trafficking, also have lower levels of $GABA_A\alpha6$ subunits as a mechanism to attempt to boost excitatory signals from MFs [133]. In principle this tactic could augment glutamatergic signalling, as blocking $GABA_A\alpha6$ subunits with Furosemide doubles the frequency of GC APs in response to the same MF stimulation as untreated cerebellar slices [65]. Intriguingly, *stargazer* mutants also suffer from absence seizures [133], as do

Pclo$^{gt/gt}$ rats and PCH3 patients, indicating a common behavioural outcome of impaired MF transmission.

Homeostatic compensation also seems to be working on the presynaptic side at *Pclo*$^{gt/gt}$ MF synapses, as mEPSC frequency is increased. Similarly, when activity is suppressed in a single cultured hippocampal neurone via overexpression of an inward-rectifier potassium channel, mEPSC frequency but not amplitude of that neurone is increased [20], indicating an upregulation of spontaneous SV release in response to impaired excitatory transmission.

At a younger age, P15, double knockout of Wnt-7a and Dvl1 causes a reduction in mEPSC frequency but not amplitude [4]. Though this data opposes recordings from *Pclo*$^{gt/gt}$ cerebella, it is plausible that, from P15 to 3 months, the system has compensated for the reduction in mEPSCs by increasing release and input resistance. It would be interesting to see if Wnt-7a/Dvl1 double mutants do change their mEPSC frequency with age and if other parameters, such as input resistance and EPSC amplitude are comparable to our findings.

It would also be interesting to investigate the MF-GC synapse at higher frequencies of transmission, as the MF synapse can fire frequencies of up to 1600 Hz *in vitro* [36]. Furthermore, those synapses reported in the literature to be affected by loss of the Piccolo protein, the Calyx of Held and the endbulb of Held, fire at frequencies of 300 and 450 Hz respectively [132, 195] and are diminished during periods of sustained SV release [21, 50]. It could be predicted that, due to defects in SV recycling found by Ackermann et al. [2], higher frequencies of transmission at the MF synapse are greatly impaired and the increase in excitability observed in our recordings at 1 Hz would be neutralised or even suppressed by a deficit in high frequency transmission.

Taken together these data show that the loss of Piccolo causes changes in synaptic transmission at the MF-GC synapse; these are predicted to trigger a homeostatic increase in excitability due to a reduction in NT released from smaller MFs. The MF synapse is remarkably plastic and previous work has demonstrated its ability to adapt in the face of changing circumstances. An interesting future experiment could be to investigate whether this phenotype is truly a homeostatic compensation by conditional knockout of the Piccolo gene after cerebellar development is complete, followed by acute and long-term investigation of receptor expression and electrophysiological properties at both low and high frequency stimulation.

7.6 Mechanisms of synapse maturation: Wnt signalling In *Pclo*$^{gt/gt}$

The role of Wnt ligands in MF maturation has been discussed above (see chapter 7.4.2). We were therefore interested to explore whether Wnt signalling within *Pclo*$^{gt/gt}$ growth cones was impaired in a simplified *in vitro* culture model. Here, we cultured pontine explants from *Pclo*$^{wt/wt}$ and *Pclo*$^{gt/gt}$ pups and treated them with Wnt-7a. There were no differences in growth cone size or complexity in

untreated media; however, the addition of Wnt-7a increased the size and complexity of *Pclo*$^{wt/wt}$ growth cones but not *Pclo*$^{gt/gt}$ (Figure 29), indicating that Piccolo is required to mediate Wnt-7a signalling in these growth cones.

Piccolo is strongly expressed in the developing growth cone [200] and interacts with components of the Wnt signalling cascade Daam1, CtBPs and Trio [87, 170, 179]. The Wnt signalling cascade is complex and numerous factors are involved; in the PCP pathway, Piccolo could play a role via its interaction with Daam1 [179], which is essential to bring Rho, a regulator of the cytoskeleton, to the Wnt-activated frizzled receptor and Dvl [59]. Piccolo could also affect remodelling of the Actin cytoskeleton via its association with F-Actin [179, 182]. Ciani et al. [30] suggested that Wnt-activated spreading and stabilisation of microtubules in the event of MF remodelling [63] is mediated by the canonical Wnt pathway via a transcription-independent pathway. This pathway requires the inhibition of GSK-3β and can be mimicked by lithium or valproate which both inhibit GSK-3β [62, 63, 108]. Recent work by Martinez et al. [113] found that Wnt-3a treatment of hippocampal neurones increased levels of pre- and postsynaptic proteins including Piccolo. The authors also performed *in silico* analysis of a number of pre- and postsynaptic proteins and found putative β-catenin-activated transcription factor binding sites in the promoter regions of the *Pclo* gene. As Wnts are involved in synapse formation, maturation and vesicle cycling [4, 26, 63, 145], it is perhaps not surprising that Wnts can induce an increase in transcription and expression of these proteins. Importantly, this study provides evidence for an interaction between Piccolo and members of the Wnt signalling cascade, as well as a putative interaction between Wnt-induced transcription factors and the *Pclo* gene.

Whilst by no means is the above experiment evidence for a direct interaction between Piccolo and Wnt signalling cascades, these data hint to the involvement of Piccolo in Wnt-7a-induced axonal remodelling. Future studies are needed to resolve this mechanism further and to dissect the intricate components of the Wnt signalling cascades that might be affected by Piccolo LOF. It would be interesting to explore this model system further, in particular to manipulate specific domains of the Piccolo protein such as those binding domains for proteins implicated in the Wnt signalling cascade.

7.7 Piccolo loss of function manifests in disturbed motor control

Disruption of the Piccolo gene leads to a large number and a wide range of phenotypes, of which some have been investigated during this thesis and discussed above. Because our experiments focused mainly of the cerebellum and pontocerebellar circuitry and PCH3 patients suffer from impaired motor performance, we investigated the loss of Piccolo function on performance at tasks related to movement and motor control.

Therefore, we tested the motor abilities of *Pclo*$^{gt/gt}$, *Pclo*$^{wt/gt}$ and *Pclo*$^{wt/wt}$ rats. Here, we found that, at tasks such as the rotarod, isometric pull task and ladder walk test, *Pclo*$^{gt/gt}$ rats were severely

impaired compared to *Pclo*$^{wt/wt}$ and *Pclo*$^{wt/gt}$ controls (Figure 27), despite comparable performance during grip strength test. These data indicate that reduced performance in these tests is due to a failure in motor coordination rather than muscle strength. *Pclo*$^{gt/gt}$ rats also displayed less rearing behaviours in the open field test, perhaps because this behaviour requires more motor coordination in order to balance. Interestingly, *Pclo*$^{gt/gt}$ rats were more active than *Pclo*$^{wt/wt}$ and *Pclo*$^{wt/gt}$ and travelled a greater distance in a home cage setup.

The entire circuitry system of the cerebellum, parts of which have been investigated in this thesis, culminates in inhibitory axons from PCs to the deep cerebellar nuclei. Thus the nature of this system is to generate a temporal pattern of inhibition in order to modify excitatory activation of muscle fibres and fine tune movement. As a result, disorders of the cerebellum manifest in a loss of motor coordination and ataxic movement [57].

Failure at tests such as ladder walk and rotarod are classic readouts of loss of motor coordination (Figure 27) [16, 34]. As Piccolo is also expressed at the neuromuscular junction [91], we wanted to check whether this failure was due to impaired muscle strength. Performance on the grip strength task and the increase in activity in the home cage in OptiMan setup confirm capability of movement and indicate that the failure at such tasks is due to a coordination of motor commands rather than movement itself.

Of note, our study has shown that the MF synapse is the most affected afferent in *Pclo*$^{gt/gt}$ cerebella. Similarly, mutant mice harbouring a mutation in the *stargazin* gene, *stargazer* and *wobbler* are perturbed by decreased AMPA receptors and therefore impaired excitatory transmission at this synapse, accompanied by a compensatory decrease in $GABA_A\alpha6$ subunit. These mice also display ataxic behaviour and absence seizures [28, 68], as do patients with PCH3.

Another excitatory receptor at the MF synapse is the NMDA receptor; ablation of both NR2A and NR2C subunits, but not either one alone, caused a reduction in EPSCs and a similar reduction in performance in rortarod task to *Pclo*$^{gt/gt}$, demonstrating necessity of excitatory transmission at MFs in motor coordination [92].

Another striking phenotype of the *Pclo*$^{gt/gt}$ rat is the overall loss of GCs. There are many mutant models of GC loss with different causal mutations. Not surprisingly, mutants such as *weaver, lurcher* and *staggerer*, who suffer from a dramatic loss in GCs, also display ataxic phenotypes and failure at motor coordination tasks [25]. GC number could be another contributor to impaired motor coordination in *Pclo*$^{gt/gt}$.

Interestingly, *Pclo*$^{gt/gt}$ rats were more active than *Pclo*$^{wt/wt}$ and *Pclo*$^{wt/gt}$; whilst this cannot be directly explained by classic cases of cerebellar lesions or synapse dysfunction, it is worth considering the other roles of Piccolo in light of these data. The implication of Piccolo in a number of psychiatric

disorders [29, 169] and findings by Medrano et al [116] that *Pclo*$^{gt/gt}$ rats display aggressive behaviour and a number of changes in depression-related genes may contribute to increased movement around the home cage setup. The hypothalamic-pituitary-adrenal (HPA) axis is responsible for homeostasis of stress response and dysregulation of this response has been reported in patients with major depressive disorder and an SNP in the *PCLO* gene [157, 169]. High expression of Piccolo in the endocrine system and specifically the pituitary gland [174] implies a role for Piccolo in the endocrine system, which could affect stress response behaviour and therefore movement of *Pclo*$^{gt/gt}$ rats.

A fundamental question raised by the anatomical, morphological and functional changes within the cerebellum of rats lacking Piccolo is whether these changes affect the functionality of the cerebellum. In behavioural tests, we observed that *Pclo*$^{gt/gt}$ rats performed worse than both *Pclo*$^{wt/wt}$ and *Pclo*$^{wt/gt}$ littermates at motor coordination tasks, highlighting the recessive nature of the behavioural impairments. Medrano et al. [116] also observed epileptic seizures, increased aggression and suppression of mating/copulation behaviours and thus reproduction in *Pclo*$^{gt/gt}$ rats.

7.8 Bassoon, a homolog of Piccolo: comparative studies

Considering that Piccolo is the largest known protein at the CAZ [139], the phenotype observed, particularly in relation to synaptic transmission, is relatively mild [2, 104, 124, 182]. It is likely that, in the *Pclo*$^{gt/gt}$ model, its homologous binding partner, Bassoon, may compensate for a number of its functions. Indeed, when both proteins are inactivated in hippocampal synapses, SV pools and synaptic junctions are severely affected, leading to disintegration of the presynapse [183]. It is therefore important to consider the role of Bassoon in the *Pclo*$^{gt/gt}$ rat.

Piccolo and Bassoon both share binding domains for the E3 ubiquitin ligase Siah1, reported by Waites et al. [183] to be responsible for the proteasomal and endo-lysosomal degradation and therefore loss of synaptic integrity observed in double knockdown studies. Interestingly, the knockout of Bassoon alone leads to an increase in autophagic markers due to a loss of suppression of pro-autophagic Atg5 [131]. Though the present study has focused on the role of Piccolo in the development of the brain in *Pclo*$^{gt/gt}$ rats and PCH3 patients, it is important to consider whether degradation via the ubiquitin-proteasome system or via presynaptic autophagy could play a role in the loss of synaptic integrity observed in Piccolo and/or Bassoon LOF studies; future work could investigate this further.

The physiology of fast-transmitting central synapses also seems to be affected by Bassoon LOF, as MG-GC and endbulb of Held synapses also demonstrate an increase in synaptic depression at high frequency transmission but are unaffected at lower frequencies [64, 158], similar to that observed by Ackermann et al. [2] at hippocampal *Pclo*$^{gt/gt}$ synapses. This enhanced depression demonstrated that Bassoon is involved in the reloading of SVs at release sites. Loss of Bassoon at the endbulb of Held

also triggered homeostatic increase in excitability of postsynaptic bushy cells and an upregulation of Piccolo [158], demonstrating the plasticity of these synapses and the compensatory nature of these critical scaffolding proteins. These studies demonstrate the important role of presynaptic scaffolding proteins in the SV cycle [73].

Intriguingly, whilst a striking phenotype of both PCH3 patients and the *Pclo*$^{gt/gt}$ rat is a lack of growth - from smaller body stature to a drastic loss of specific brain areas - knockout of Bassoon, which shares 10 homology domains [58] with the Piccolo protein, leads to cortical and hippocampal enlargement and a lack of dentate gyrus maturation and therefore enhanced spatial and contextual fear response memory performance as well as seizures, in part due to an increase in BDNF levels [7, 77]. It is possible that these two proteins stabilise each other in the normal growth and development of the brain.

7.9 *Pclo*$^{gt/gt}$ as a model for Pontocerebellar Hypoplasia Type 3

The generation of *Pclo*$^{gt/gt}$ rats [116] and the link between Piccolo and PCH3 [5] sparked the opportunity to investigate phenotypes of PCH3 at the synaptic level and to study mechanisms that could be involved in disease pathology that simply is not possible in human patients. Interestingly, an earlier mouse model that lacks primarily the largest Piccolo isoforms is also smaller than wildtype counterparts, but no epileptic activity or changes in brain anatomy was reported [124], implying that the isoforms responsible for the PCH3 phenotype may still have been present in that Piccolo KO mouse. The *Pclo*$^{gt/gt}$ rat therefore is a more appropriate model to investigate PCH3 but it should be remembered that the complexity of genetic manipulation of the Piccolo gene highlights the importance of utilising mutations more closely resembling the SNP from PCH3 patients in future studies.

Taken together, our data support the concept that Piccolo loss of function in patients with PCH3 could contribute to many of the observed phenotypes, including changes in the volume of brain structures and behavioural abnormalities such as impaired motor control and epileptic seizures [127, 137]. With regard to reduced cerebellar function, our studies highlight a prominent role for MF boutons which are not only smaller in size but with altered synaptic properties. Mechanistic studies, which probe how Piccolo loss contributes to these changes, should provide insights into both the role of Piccolo during cerebellar development and the aetiology of PCH3.

8. References

1 Ackermann F, Gregory, J.A., Brodin, L. (2012) Key Events in Synaptic Vesicle Endocytosis. In: Brian Ceresa (ed) *Molecular Regulation of Endocytosis* IntechOpen, Rijeka, Croatia.

2 Ackermann F, Schink KO, Bruns C, Izsvak Z, Hamra FK, Rosenmund C, Garner CC (2019) Critical role for Piccolo in synaptic vesicle retrieval. Elife 8 e46629

3 Ackermann F, Waites CL, Garner CC (2015) Presynaptic active zones in invertebrates and vertebrates. Embo Rep 16: 923-938

4 Ahmad-Annuar A, Ciani L, Simeonidis I, Herreros J, Fredj NB, Rosso SB, Hall A, Brickley S, Salinas PC (2006) Signaling across the synapse: a role for Wnt and Dishevelled in presynaptic assembly and neurotransmitter release. J Cell Biol 174: 127-139

5 Ahmed MY, Chioza BA, Rajab A, Schmitz-Abe K, Al-Khayat A, Al-Turki S, Baple EL, Patton MA, Al-Memar AY, Hurles MEet al (2015) Loss of PCLO function underlies pontocerebellar hypoplasia type III. Neurology 84: 1745-1750

6 Aigner L, Caroni P (1995) Absence of persistent spreading, branching, and adhesion in GAP-43-depleted growth cones. J Cell Biol 128: 647-660

7 Annamneedi A, Caliskan G, Muller S, Montag D, Budinger E, Angenstein F, Fejtova A, Tischmeyer W, Gundelfinger ED, Stork O (2018) Ablation of the presynaptic organizer Bassoon in excitatory neurons retards dentate gyrus maturation and enhances learning performance. Brain Structure & Function 223: 3423-3445

8 Appelhof B, Barth, P. G., Baas, F. (2019) Classification of Pontocerebellar Hypoplasia: Where does it End? EMJ Neurology 7: 52-61

9 Apps R, Garwicz M (2005) Anatomical and physiological foundations of cerebellar information processing. Nat Rev Neurosci 6: 297-311

10 Armano S, Rossi P, Taglietti V, D'Angelo E (2000) Long-term potentiation of intrinsic excitability at the Mossy fiber-granule cell synapse of rat cerebellum. Journal of Neuroscience 20: 5208-5216

11 Bailly Y, Rabacchi S, Sherrard RM, Rodeau JL, Demais V, Lohof AM, Mariani J (2018) Elimination of all redundant climbing fiber synapses requires granule cells in the postnatal cerebellum. Sci Rep-Uk 8:10017

12 Barnes AP, Polleux F (2009) Establishment of axon-dendrite polarity in developing neurons. Annu Rev Neurosci 32: 347-381

13 Bermingham NA, Hassan BA, Wang VY, Fernandez M, Banfi S, Bellen HJ, Fritzsch B, Zoghbi HY (2001) Proprioceptor pathway development is dependent on MATH1. Neuron 30: 411-422

14 Billings G, Piasini E, Lorincz A, Nusser Z, Silver RA (2014) Network Structure within the Cerebellar Input Layer Enables Lossless Sparse Encoding. Neuron 83: 960-974

15 Brickley SG, Cull-Candy SG, Farrant M (1996) Development of a tonic form of synaptic inhibition in rat cerebellar granule cells resulting from persistent activation of GABAA receptors. J Physiol 497 (Pt 3): 753-759.

16 Brooks SP, Trueman RC, Dunnett SB (2012) Assessment of Motor Coordination and Balance in Mice Using the Rotarod, Elevated Bridge, and Footprint Tests. Curr Protoc Mouse Biol 2: 37-53

17 Brown AM, Arancillo M, Lin T, Catt DR, Zhou J, Lackey EP, Stay TL, Zuo ZY, White JJ, Sillitoe RV (2019) Molecular layer interneurons shape the spike activity of cerebellar Purkinje cells. Sci Rep-Uk 9: 1742

18 Bruckner JJ, Gratz SJ, Slind JK, Geske RR, Cummings AM, Galindo SE, Donohue LK, O'Connor-Giles KM (2012) Fife, a Drosophila Piccolo-RIM Homolog, Promotes Active Zone Organization and Neurotransmitter Release. Journal of Neuroscience 32: 17048-17058

19 Burrone J, Murthy VN (2003) Synaptic gain control and homeostasis. Current Opinion in Neurobiology 13: 560-567

20 Burrone J, O'Byrne M, Murthy VN (2002) Multiple forms of synaptic plasticity triggered by selective suppression of activity in individual neurons. Nature 420: 414-418

21 Butola T, Wichmann C, Moser T (2017) Piccolo Promotes Vesicle Replenishment at a Fast Central Auditory Synapse. Front Synaptic Neurosci 9: 14

22 Byczkowicz N, Ritzau-Jost A, Delvendahl I, Hallermann S (2018) How to maintain active zone integrity during high-frequency transmission. Neurosci Res 127: 61-69

23 Cases-Langhoff C, Voss B, Garner AM, Appeltauer U, Takei K, Kindler S, Veh RW, De Camilli P, Gundelfinger ED, Garner CC (1996) Piccolo, a novel 420 kDa protein associated with the presynaptic cytomatrix. Eur J Cell Biol 69: 214-223

24 Cen X, Nitta A, Ibi D, Zhao Y, Niwa M, Taguchi K, Hamada M, Ito Y, Ito Y, Wang Let al (2008) Identification of Piccolo as a regulator of behavioral plasticity and dopamine transporter internalization. Mol Psychiatr 13: 451-463

25 Cendelin J (2014) From mice to men: lessons from mutant ataxic mice. Cerebellum Ataxias 1: 4

26 Cerpa W, Godoy JA, Alfaro I, Farlas GG, Metcalfe MJ, Fuentealba R, Bonansco C, Inestrosa NC (2008) Wnt-7a modulates the synaptic vesicle cycle and synaptic transmission in hippocampal neurons. J Biol Chem 283: 5918-5927

27 Chen AI, Zang K, Masliah E, Reichardt LF (2016) Glutamatergic axon-derived BDNF controls GABAergic synaptic differentiation in the cerebellum. Sci Rep 6: 20201

28 Chen L, Bao SW, Qiao XX, Thompson RF (1999) Impaired cerebellar synapse maturation in waggler, a mutant mouse with a disrupted neuronal calcium channel gamma subunit. P Natl Acad Sci USA 96: 12132-12137

29 Choi KH, Higgs BW, Wendland JR, Song J, McMahon FJ, Webster MJ (2011) Gene Expression and Genetic Variation Data Implicate PCLO in Bipolar Disorder. Biol Psychiat 69: 353-359

30 Ciani L, Krylova O, Smalley MJ, Dale TC, Salinas PC (2004) A divergent canonical WNT-signaling pathway regulates microtubule dynamics: Dishevelled signals locally to stabilize microtubules. Journal of Cell Biology 164: 243-253

31 Ciani L, Salinas PC (2005) WNTs in the vertebrate nervous system: from patterning to neuronal connectivity. Nat Rev Neurosci 6: 351-362

32 Clayton EL, Evans GJO, Cousin MA (2008) Bulk synaptic vesicle endocytosis is rapidly triggered during strong stimulation. Journal of Neuroscience 28: 6627-6632

33 Corrales JMD, Rocco GL, Blaess S, Guo QX, Joyner AL (2004) Spatial pattern of sonic hedgehog signaling through Gli genes during cerebellum development. Development 131: 5581-5590

34 Curzon P, Zhang M, Radek RJ, Fox GB (2009) The Behavioral Assessment of Sensorimotor Processes in the Mouse: Acoustic Startle, Sensory Gating, Locomotor Activity, Rotarod, and Beam Walking. In: Buccafusco JJ (ed) *Methods of Behavior Analysis in Neuroscience*, CRC Press, Florida, USA

35 De Zeeuw CI, Ten Brinke MM (2015) Motor Learning and the Cerebellum. Cold Spring Harb Perspect Biol 7: a021683

36 Delvendahl I, Hallermann S (2016) The Cerebellar Mossy Fiber Synapse as a Model for High-Frequency Transmission in the Mammalian CNS. Trends in Neurosciences 39: 722-737

37 Delvendahl I, Straub I, Hallermann S (2015) Dendritic patch-clamp recordings from cerebellar granule cells demonstrate electrotonic compactness. Frontiers in Cellular Neuroscience 9: 93

38 Delvendahl I, Vyleta NP, von Gersdorff H, Hallermann S (2016) Fast, Temperature-Sensitive and Clathrin-Independent Endocytosis at Central Synapses. Neuron 90: 492-498

39 Dick O, Hack I, Altrock WD, Garner CC, Gundelfinger ED, Brandstatter JH (2001) Localization of the presynaptic cytomatrix protein Piccolo at ribbon and conventional synapses in the rat retina: comparison with Bassoon. J Comp Neurol 439: 224-234

40 Dieudonne S, Dumoulin A (2000) Serotonin-driven long-range inhibitory connections in the cerebellar cortex. Journal of Neuroscience 20: 1837-1848

41 Doussau F, Augustine GJ (2000) The actin cytoskeleton and neurotransmitter release: an overview. Biochimie 82: 353-363

42 Durmaz B, Wollnik B, Cogulu O, Li Y, Tekgul H, Hazan F, Ozkinay F (2009) Pontocerebellar hypoplasia type III (CLAM): Extended phenotype and novel molecular findings. J Neurol 256: 416-419

43 Eccles JC, Llinas R, Sasaki K (1966) The excitatory synaptic action of climbing fibres on the Purkinje cells of the cerebellum. J Physiol 182: 268-296

44 Eccles JC, Llinás R, Sasaki K (1966) The mossy fibre-granule cell relay of the cerebellum and its inhibitory control by Golgi cells. Experimental Brain Research 1: 82-101

45 Eshra A, Hirrlinger P, Hallermann S (2019) Enriched Environment Shortens the Duration of Action Potentials in Cerebellar Granule Cells. Front Cell Neurosci 13: 289

46 Falck J, Bruns., C., Hoffmann-Conaway, S., Straub, I., Plautz, E., Orlando, M., Munawar, H., Rivalan, M., Winter, Y., Izsvák, Z., Schmitz, D., Hallermann, S., Garner, C.C., Ackermann, F. (in press) Loss of Piccolo function in rats induces cerebellar network dysfunction and Pontocerebellar Hypoplasia type 3-like phenotypes The Journal of Neuroscience

47 Fenster SD, Chung WJ, Zhai R, Cases-Langhoff C, Voss B, Garner AM, Kaempf U, Kindler S, Gundelfinger ED, Garner CC (2000) Piccolo, a presynaptic zinc finger protein structurally related to bassoon. Neuron 25: 203-214

48 Fenster SD, Garner CC (2002) Gene structure and genetic localization of the PCLO gene encoding the presynaptic active zone protein Piccolo. Int J Dev Neurosci 20: 161-171

49 Fenster SD, Kessels MM, Qualmann B, Chung WJ, Nash J, Gundelfinger ED, Garner CC (2003) Interactions between Piccolo and the actin/dynamin-binding protein Abp1 link vesicle endocytosis to presynaptic active zones. J Biol Chem 278: 20268-20277

50 Fernandez-Alfonso T, Ryan TA (2006) The efficiency of the synaptic vesicle cycle at central nervous system synapses. Trends Cell Biol 16: 413-420

51 Forster E, Zhao ST, Frotscher M (2006) Laminating the hippocampus. Nature Reviews Neuroscience 7: 259-U212

52 Frank T, Rutherford MA, Strenzke N, Neef A, Pangrsic T, Khimich D, Fejtova A, Gundelfinger ED, Liberman MC, Harke Bet al (2010) Bassoon and the synaptic ribbon organize Ca(2)+ channels and vesicles to add release sites and promote refilling. Neuron 68: 724-738

53 Gabbiani F, Cox, SJ (2017) Chapter 13 - Synaptic Transmission and Quantal Release. In: Gabbiani, F, Cox, SJ (eds) *Mathematics for Neuroscientists* Elsevier, Amsterdam, Netherlands

54 Gao C, Chen YG (2010) Dishevelled: The hub of Wnt signaling. Cell Signal 22: 717-727

55 Garcia AL, Udeh A, Kalahasty K, Hackam AS (2018) A growing field: the regulation of axonal regeneration by Wnt signaling. Neural Regen Res 13: 43-52

56 Gordon MD, Nusse R (2006) Wnt signaling: multiple pathways, multiple receptors, and multiple transcription factors. J Biol Chem 281: 22429-22433

57 Grusser-Cornehls U, Baurle J (2001) Mutant mice as a model for cerebellar ataxia. Prog Neurobiol 63: 489-540

58 Gundelfinger ED, Reissner C, Garner CC (2016) Role of Bassoon and Piccolo in Assembly and Molecular Organization of the Active Zone. Front Synaptic Neurosci 7: 19

59 Habas R, Kato Y, He X (2001) Wnt/Frizzled activation of Rho regulates vertebrate gastrulation and requires a novel formin homology protein Daam1. Cell 107: 843-854

60 Haines DE, Mihailoff, G. A., Bloedel, J. R. (2015) The Cerebellum https://clinicalgate.com/the-cerebellum/. Accessed 2020

61 Hajos F, Patel AJ, Balazs R (1973) Effect of thyroid deficiency on the synaptic organization of the rat cerebellar cortex. Brain Res 50: 387-401

62 Hall AC, Brennan A, Goold RG, Cleverley K, Lucas FR, Gordon-Weeks PR, Salinas PC (2002) Valproate regulates GSK-3-mediated axonal remodeling and synapsin I clustering in developing neurons. Mol Cell Neurosci 20: 257-270

63 Hall AC, Lucas FR, Salinas PC (2000) Axonal remodeling and synaptic differentiation in the cerebellum is regulated by WNT-7a signaling. Cell 100: 525-535

64 Hallermann S, Fejtova A, Schmidt H, Weyhersmuller A, Silver RA, Gundelfinger ED, Eilers J (2010) Bassoon Speeds Vesicle Reloading at a Central Excitatory Synapse. Neuron 68: 710-723

65 Hamann M, Rossi DJ, Attwell D (2002) Tonic and spillover inhibition of granule cells control information flow through cerebellar cortex. Neuron 33: 625-633

66 Hamori J, Somogyi J (1983) Differentiation of cerebellar mossy fiber synapses in the rat: a quantitative electron microscope study. J Comp Neurol 220: 365-377

67 Harvey RJ, Napper RMA (1988) Quantitative Study of Granule and Purkinje-Cells in the Cerebellar Cortex of the Rat. Journal of Comparative Neurology 274: 151-157

68 Hashimoto K, Fukaya M, Qiao X, Sakimura K, Watanabe M, Kano M (1999) Impairment of AMPA receptor function in cerebellar granule cells of ataxic mutant mouse stargazer. J Neurosci 19: 6027-6036

69 Hashimoto K, Ichikawa R, Kitamura K, Watanabe M, Kano M (2009) Translocation of a "winner" climbing fiber to the Purkinje cell dendrite and subsequent elimination of "losers" from the soma in developing cerebellum. Neuron 63: 106-118

70 Hashimoto K, Kano M (1998) Presynaptic origin of paired-pulse depression at climbing fibre-Purkinje cell synapses in the rat cerebellum. J Physiol 506 (Pt 2): 391-405

71 Hashimoto K, Kano M (2013) Synapse elimination in the developing cerebellum. Cell Mol Life Sci 70: 4667-4680

72 Hashimoto K, Miyata M, Watanabe M, Kano M (2001) Roles of phospholipase C beta 4 in synapse elimination and plasticity in developing and mature cerebellum. Molecular Neurobiology 23: 69-82

73 Haucke V, Neher E, Sigrist SJ (2011) Protein scaffolds in the coupling of synaptic exocytosis and endocytosis. Nat Rev Neurosci 12: 127-138

74 Hayashi K, Furuya A, Sakamaki Y, Akagi T, Shinoda Y, Sadakata T, Hashikawa T, Shimizu K, Minami H, Sano Yet al (2017) The brain-specific RasGEF very-KIND is required for normal dendritic growth in cerebellar granule cells and proper motor coordination. Plos One 12(3): e0173175

75 Hennig MH (2013) Theoretical models of synaptic short term plasticity. Front Comput Neurosc 7: 45

76 Heuser JE, Reese TS (1973) Evidence for recycling of synaptic vesicle membrane during transmitter release at the frog neuromuscular junction. J Cell Biol 57: 315-344

77 Heyden A, Ionescu MCS, Romorini S, Kracht B, Ghiglieri V, Calabresi P, Seidenbecher C, Angenstein F, Gundelfinger ED (2011) Hippocampal enlargement in Bassoon-mutant mice is associated with enhanced neurogenesis, reduced apoptosis, and abnormal BDNF levels. Cell Tissue Res 346: 11-26

78 Hioki H, Fujiyama F, Taki K, Tomioka R, Furuta T, Tamamaki N, Kaneko T (2003) Differential distribution of vesicular glutamate transporters in the rat cerebellar cortex. Neuroscience 117: 1-6

79 Hisano S, Sawada K, Kawano M, Kanemoto M, Xiong G, Mogi K, Sakata-Haga H, Takeda J, Fukui Y, Nogami H (2002) Expression of inorganic phosphate/vesicular glutamate transporters (BNPI/VGLUT1 and DNPI/VGLUT2) in the cerebellum and precerebellar nuclei of the rat. Brain Res Mol Brain Res 107: 23-31

80 Homanics GE, Ferguson C, Quinlan JJ, Daggett J, Snyder K, Lagenaur C, Mi Z-P, Wang X-H, Grayson DR, Firestone LL (1997) Gene Knockout of the α6 Subunit of the γ-Aminobutyric

Acid Type A Receptor: Lack of Effect on Responses to Ethanol, Pentobarbital, and General Anesthetics. Molecular Pharmacology 51: 588-596

81 Hong SE, Shugart YY, Huang DT, Shahwan SA, Grant PE, Hourihane JOB, Martin NDT, Walsh CA (2000) Autosomal recessive lissencephaly with cerebellar hypoplasia is associated with human RELN mutations. Nat Genet 26: 93-96

82 Hubler D, Rankovic M, Richter K, Lazarevic V, Altrock WD, Fischer KD, Gundelfinger ED, Fejtova A (2012) Differential spatial expression and subcellular localization of CtBP family members in rodent brain. PLoS One 7: e39710

83 Ichikawa R, Hashimoto K, Miyazaki T, Uchigashima M, Yamasaki M, Aiba A, Kano M, Watanabe M (2016) Territories of heterologous inputs onto Purkinje cell dendrites are segregated by mGluR1-dependent parallel fiber synapse elimination. Proc Natl Acad Sci U S A 113: 2282-2287

84 Ichise T, Kano M, Hashimoto K, Yanagihara D, Nakao K, Shigemoto R, Katsuki M, Aiba A (2000) mGLuR1 in cerebellar Purkinje cells essential for long-term depression, synapse elimination, and motor coordination. Science 288: 1832-1835

85 Isope P, Barbour B (2002) Properties of unitary granule cell-->Purkinje cell synapses in adult rat cerebellar slices. J Neurosci 22: 9668-9678

86 Ito M (2008) Opinion - Control of mental activities by internal models in the cerebellum. Nature Reviews Neuroscience 9: 304-313

87 Ivanova D, Dirks A, Montenegro-Venegas C, Schone C, Altrock WD, Marini C, Frischknecht R, Schanze D, Zenker M, Gundelfinger EDet al (2015) Synaptic activity controls localization and function of CtBP1 via binding to Bassoon and Piccolo. EMBO J 34: 1056-1077

88 Ivics Z, Li MA, Mates L, Boeke JD, Nagy A, Bradley A, Izsvak Z (2009) Transposon-mediated genome manipulation in vertebrates (vol 6, pg 415, 2009). Nat Methods 6: 546-546

89 Izsvak Z, Frohlich J, Grabundzija I, Shirley JR, Powell HM, Chapman KM, Ivics Z, Hamra FK (2010) Generating knockout rats by transposon mutagenesis in spermatogonial stem cells. Nat Methods 7: 443-445

90 Jakab RL, Hamori J (1988) Quantitative Morphology and Synaptology of Cerebellar Glomeruli in the Rat. Anat Embryol 179: 81-88

91 Juranek J, Mukherjee K, Rickmann M, Martens H, Calka J, Sudhof TC, Jahn R (2006) Differential expression of active zone proteins in neuromuscular junctions suggests functional diversification. Eur J Neurosci 24: 3043-3052

92 Kadotani H, Hirano T, Masugi M, Nakamura K, Nakao K, Katsuki M, Nakanishi S (1996) Motor discoordination results from combined gene disruption of the NMDA receptor NR2A and NR2C subunits, but not from single disruption of the NR2A or NR2C subunit. J Neurosci 16: 7859-7867

93 Kakizawa S, Yamasaki M, Watanabe M, Kano M (2000) Critical period for activity-dependent synapse elimination in developing cerebellum. Journal of Neuroscience 20: 4954-4961

94 Kalinovsky A, Boukhtouche F, Blazeski R, Bornmann C, Suzuki N, Mason CA, Scheiffele P (2011) Development of Axon-Target Specificity of Ponto-Cerebellar Afferents. Plos Biol 9:e1001013

95 Ke MC, Guo CC, Raymond JL (2009) Elimination of climbing fiber instructive signals during motor learning. Nat Neurosci 12: 1171-U1123

96 Khimich D, Nouvian R, Pujol R, Tom Dieck S, Egner A, Gundelfinger ED, Moser T (2005) Hair cell synaptic ribbons are essential for synchronous auditory signalling. Nature 434: 889-894

97 Kittel RJ, Hallermann S, Thomsen S, Wichmann C, Sigrist SJ, Heckmann M (2006) Active zone assembly and synaptic release. Biochem Soc Trans 34: 939-941

98 Klausberger T, Somogyi P (2008) Neuronal diversity and temporal dynamics: the unity of hippocampal circuit operations. Science 321: 53-57

99 Koibuchi N, Ikeda, Y (2013) Hormones and Cerebellar Development. In: Manto M, Schmahmann JD, Rossi F, Gruol L, Koibuchi N (eds) *Handbook of the Cerebellum and Cerebellar Disorders*, Springer, Dordrecht, Netherlands

100 Konarski JZ, McIntyre RS, Grupp LA, Kennedy SH (2005) Is the cerebellum relevant in the circuitry of neuropsychiatric disorders? J Psychiatr Neurosci 30: 178-186

101 Kononenko NL, Haucke V (2015) Molecular Mechanisms of Presynaptic Membrane Retrieval and Synaptic Vesicle Reformation. Neuron 85: 484-496

102 Kratochwil CF, Maheshwari U, Rijli FM (2017) The Long Journey of Pontine Nuclei Neurons: From Rhombic Lip to Cortico-Ponto-Cerebellar Circuitry. Front Neural Circuits 11: 33

103 Kuwako K, Nishimoto Y, Kawase S, Okano HJ, Okano H (2014) Cadherin-7 Regulates Mossy Fiber Connectivity in the Cerebellum. Cell Rep 9: 311-323

104 Leal-Ortiz S, Waites CL, Terry-Lorenzo R, Zamorano P, Gundelfinger ED, Garner CC (2008) Piccolo modulation of Synapsin1a dynamics regulates synaptic vesicle exocytosis. J Cell Biol 181: 831-846

105 Lee HJ, Suk JE, Bae EJ, Lee JH, Paik SR, Lee SJ (2008) Assembly-dependent endocytosis and clearance of extracellular alpha-synuclein. Int J Biochem Cell Biol 40: 1835-1849

106 Leto K, Arancillo M, Becker EB, Buffo A, Chiang C, Ding B, Dobyns WB, Dusart I, Haldipur P, Hatten MEet al (2016) Consensus Paper: Cerebellar Development. Cerebellum 15: 789-828

107 Lisberger SGT, WT (2000) The Cerebellum. In: Kandel, E. Schwartz, JH, & Jessell, TM (eds), *Principles of Neuroscience*, McGraw-Hill, New York, USA

108 Lucas FR, Salinas PC (1997) WNT-7a induces axonal remodeling and increases synapsin I levels in cerebellar neurons. Dev Biol 192: 31-44

109 Lucido AL, Suarez Sanchez F, Thostrup P, Kwiatkowski AV, Leal-Ortiz S, Gopalakrishnan G, Liazoghli D, Belkaid W, Lennox RB, Grutter Pet al (2009) Rapid assembly of functional presynaptic boutons triggered by adhesive contacts. J Neurosci 29: 12449-12466

110 Maas C, Torres VI, Altrock WD, Leal-Ortiz S, Wagh D, Terry-Lorenzo RT, Fejtova A, Gundelfinger ED, Ziv NE, Garner CC (2012) Formation of Golgi-derived active zone precursor vesicles. J Neurosci 32: 11095-11108

111 Maex R, De Schutter E (1998) Synchronization of golgi and granule cell firing in a detailed network model of the cerebellar granule cell layer. J Neurophysiol 80: 2521-2537

112 Manto M, Bower JM, Conforto AB, Delgado-Garcia JM, da Guarda SN, Gerwig M, Habas C, Hagura N, Ivry RB, Marien Pet al (2012) Consensus paper: roles of the cerebellum in motor control--the diversity of ideas on cerebellar involvement in movement. Cerebellum 11: 457-487

113 Martinez M, Torres VI, Vio CP, Inestrosa NC (2019) Canonical Wnt Signaling Modulates the Expression of Pre- and Postsynaptic Components in Different Temporal Patterns. Mol Neurobiol: 57: 1389-1404

114 Matthews G, Fuchs P (2010) The diverse roles of ribbon synapses in sensory neurotransmission. Nat Rev Neurosci 11: 812-822

115 Mayhew TM, Gundersen HJ (1996) If you assume, you can make an ass out of u and me': a decade of the disector for stereological counting of particles in 3D space. J Anat 188 (Pt 1): 1-15

116 Medrano GA, Singh M, Plautz EJ, Good LB, Chapman KM, Chaudhary J, Jaichander P, Powell HM, Pudasaini A, Shelton JMet al (2019) Mutant screen reveals depression-associated *Piccolo's* control over brain-gonad cross talk and reproductive behavior. bioRxiv: 405985

117 Mellor JR, Merlo D, Jones A, Wisden W, Randall AD (1998) Mouse cerebellar granule cell differentiation: Electrical activity regulates the GABA(A) receptor alpha 6 subunit gene. Journal of Neuroscience 18: 2822-2833

118 Mercer A, Thomson AM (2017) Cornu Ammonis Regions-Antecedents of Cortical Layers? Frontiers in Neuroanatomy 11:83

119 Metz GA, Whishaw IQ (2009) The ladder rung walking task: a scoring system and its practical application. J Vis Exp: 12 (28) 1204

120 Miall RC (2013) Cerebellum: Anatomy and Function. In: Pfaff, D (ed), *Neuroscience in the 21st Century*, Springer, New York, USA

121 Miyazaki T, Fukaya M, Shimizu H, Watanabe M (2003) Subtype switching of vesicular glutamate transporters at parallel fibre-Purkinje cell synapses in developing mouse cerebellum. Eur J Neurosci 17: 2563-2572

122 Monje M, Mitra SS, Freret ME, Raveh TB, Kim J, Masek M, Attema JL, Li G, Haddix T, Edwards MSBet al (2011) Hedgehog-responsive candidate cell of origin for diffuse intrinsic pontine glioma. P Natl Acad Sci USA 108: 4453-4458

123 Mugnaini E, Sekerkova G, Martina M (2011) The unipolar brush cell: A remarkable neuron finally receiving deserved attention. Brain Res Rev 66: 220-245

124 Mukherjee K, Yang X, Gerber SH, Kwon HB, Ho A, Castillo PE, Liu X, Sudhof TC (2010) Piccolo and bassoon maintain synaptic vesicle clustering without directly participating in vesicle exocytosis. Proc Natl Acad Sci U S A 107: 6504-6509

125 Muller TM, Gierke K, Joachimsthaler A, Sticht H, Izsvak Z, Hamra FK, Fejtova A, Ackermann F, Garner CC, Kremers Jet al (2019) A Multiple Piccolino-RIBEYE Interaction Supports Plate-Shaped Synaptic Ribbons in Retinal Neurons. J Neurosci 39: 2606-2619

126 Najac M, Raman IM (2017) Synaptic excitation by climbing fibre collaterals in the cerebellar nuclei of juvenile and adult mice. J Physiol-London 595: 6703-6718

127 Namavar Y, Barth PG, Kasher PR, van Ruissen F, Brockmann K, Bernert G, Writzl K, Ventura K, Cheng EY, Ferriero DMet al (2011) Clinical, neuroradiological and genetic findings in pontocerebellar hypoplasia. Brain 134: 143-156

128 Neniskyte U, Gross CT (2017) Errant gardeners: glial-cell-dependent synaptic pruning and neurodevelopmental disorders. Nature Reviews Neuroscience 18: 658-670

129 Nusser Z, Sieghart W, Somogyi P (1998) Segregation of different GABAA receptors to synaptic and extrasynaptic membranes of cerebellar granule cells. J Neurosci 18: 1693-1703

130 Nusser Z, Sieghart W, Stephenson F, Somogyi P (1996) The alpha 6 subunit of the GABAA receptor is concentrated in both inhibitory and excitatory synapses on cerebellar granule cells. The Journal of Neuroscience 16: 103-114

131 Okerlund ND, Schneider K, Leal-Ortiz S, Montenegro-Venegas C, Kim SA, Garner LC, Waites CL, Gundelfinger ED, Reimer RJ, Garner CC (2017) Bassoon Controls Presynaptic Autophagy through Atg5. Neuron 93: 897-913 e897

132 Parthier D, Kuner T, Korber C (2018) The presynaptic scaffolding protein Piccolo organizes the readily releasable pool at the calyx of Held. J Physiol-London 596: 1485-1499

133 Payne HL, Connelly WM, Ives JH, Lehner R, Furtmuller B, Sieghart W, Tiwari P, Lucocq JM, Lees G, Thompson CL (2007) GABA(A) alpha 6-containing receptors are selectively compromised in cerebellar granule cells of the ataxic mouse, stargazer. J Biol Chem 282: 29130-29143

134 Pei YX, Brun SN, Markant SL, Lento W, Gibson P, Taketo MM, Giovannini M, Gilbertson RJ, Wechsler-Reya RJ (2012) WNT signaling increases proliferation and impairs differentiation of stem cells in the developing cerebellum. Development 139: 1724-1733

135 Pieribone VA, Shupliakov O, Brodin L, Hilfiker-Rothenfluh S, Czernik AJ, Greengard P (1995) Distinct pools of synaptic vesicles in neurotransmitter release. Nature 375: 493-497

136 Rabacchi SA, Solowska JM, Kruk B, Luo YL, Raper JA, Baird DH (1999) Collapsin-1 /semaphorin-III/D is regulated developmentally in Purkinje cells and collapses pontocerebellar mossy fiber neuronal growth cones. Journal of Neuroscience 19: 4437-4448

137 Rajab A, Mochida GH, Hill A, Ganesh V, Bodell A, Riaz A, Grant PE, Shugart YY, Walsh CA (2003) A novel form of pontocerebellar hypoplasia maps to chromosome 7q11-21. Neurology 60: 1664-1667

138 Rancz EA, Ishikawa T, Duguid I, Chadderton P, Mahon S, Hausser M (2007) High-fidelity transmission of sensory information by single cerebellar mossy fibre boutons. Nature 450: 1245-1248

139 Regus-Leidig H, Fuchs M, Lohner M, Leist SR, Leal-Ortiz S, Chiodo VA, Hauswirth WW, Garner CC, Brandstatter JH (2014) In vivo knockdown of Piccolino disrupts presynaptic ribbon morphology in mouse photoreceptor synapses. Front Cell Neurosci 8: 259

140 Regus-Leidig H, Ott C, Lohner M, Atorf J, Fuchs M, Sedmak T, Kremers J, Fejtova A, Gundelfinger ED, Brandstatter JH (2013) Identification and immunocytochemical characterization of Piccolino, a novel Piccolo splice variant selectively expressed at sensory ribbon synapses of the eye and ear. PLoS One 8: e70373

141 Regus-Leidig H, tom Dieck S, Specht D, Meyer L, Brandstatter JH (2009) Early steps in the assembly of photoreceptor ribbon synapses in the mouse retina: the involvement of precursor spheres. J Comp Neurol 512: 814-824

142 Rizzoli SO, Betz WJ (2005) Synaptic vesicle pools. Nat Rev Neurosci 6: 57-69

143 Robinson FR, Phillips, JO & Weiss, AH (2005) Chapter 7 - Animal Oculomotor Data Illuminate Cerebellum-Related Eye Movement Disorders. In: LeDoux, M (ed), *Animal Models of Movement Disorders*, Elsevier, Amsterdam, Netherlands

144 Rosenmund C, Rettig J, Brose N (2003) Molecular mechanisms of active zone function. Curr Opin Neurobiol 13: 509-519

145 Rosso SB, Inestrosa NC (2013) WNT signaling in neuronal maturation and synaptogenesis. Frontiers in Cellular Neuroscience 7: 103

146 Rothman JS, Silver RA (2018) NeuroMatic: An Integrated Open-Source Software Toolkit for Acquisition, Analysis and Simulation of Electrophysiological Data. Front Neuroinform 12: 14

147 Rudnik-Schoneborn S, Barth PG, Zerres K (2014) Pontocerebellar hypoplasia. Am J Med Genet C Semin Med Genet 166C: 173-183

148 Ruigrok TJH, Sillitoe, R, Voogd, J (2015) Chapter 9 - Cerebellum and Cerebellar Connections. In: Paxinos, G (ed), *The Rat Nervous System*, Elsevier, Amsterdam, Netherlands

149 Sakaba T (2006) Roles of the fast-releasing and the slowly releasing vesicles in synaptic transmission at the calyx of held. Journal of Neuroscience 26: 5863-5871

150 Salinas PC (2005) Signaling at the vertebrate synapse: New roles for embryonic morphogens? J Neurobiol 64: 435-445

151 Salinas PC, Zou YM (2008) Wnt signaling in neural circuit assembly. Annual Review of Neuroscience 31: 339-358

152 Scheiffele P (2003) Cell-cell signaling during synapse formation in the CNS. Annual Review of Neuroscience 26: 485-508

153 Schindelin J, Arganda-Carreras I, Frise E, Kaynig V, Longair M, Pietzsch T, Preibisch S, Rueden C, Saalfeld S, Schmid Bet al (2012) Fiji: an open-source platform for biological-image analysis. Nat Methods 9: 676-682

154 Schlessinger J (2004) Common and distinct elements in cellular signaling via EGF and FGF receptors. Science 306: 1506-1507

155 Schmahmann JD (1991) An emerging concept. The cerebellar contribution to higher function. Arch Neurol 48: 1178-1187

156 Schneider Gasser EM, Straub CJ, Panzanelli P, Weinmann O, Sassoe-Pognetto M, Fritschy JM (2006) Immunofluorescence in brain sections: simultaneous detection of presynaptic and postsynaptic proteins in identified neurons. Nat Protoc 1: 1887-1897

157 Schuhmacher A, Mossner R, Hofels S, Pfeiffer U, Guttenthaler V, Wagner M, Schwab SG, Maier W, Zobel A (2011) PCLO rs2522833 modulates HPA system response to antidepressant treatment in major depressive disorder. Int J Neuropsychoph 14: 237-245

158 Schulz AM, Jing ZZ, Caro JMS, Wetzel F, Dresbach T, Strenzke N, Wichmann C, Moser T (2014) Bassoon-disruption slows vesicle replenishment and induces homeostatic plasticity at a CNS synapse. Embo Journal 33: 512-527

159 Schweighofer N, Doya K, Kuroda S (2004) Cerebellar aminergic neuromodulation: towards a functional understanding. Brain Res Rev 44: 103-116

160 Shapira M, Zhai RG, Dresbach T, Bresler T, Torres VI, Gundelfinger ED, Ziv NE, Garner CC (2003) Unitary assembly of presynaptic active zones from Piccolo-Bassoon transport vesicles. Neuron 38: 237-252

161 Sherrington CS (1897) The Central Nervous System. In: Foster, M (ed) *A Textbook of Physiology*, Macmilllan, London, UK

162 Shinoda Y, Sugiuchi Y, Futami T, Izawa R (1992) Axon Collaterals of Mossy Fibers from the Pontine Nucleus in the Cerebellar Dentate Nucleus. Journal of Neurophysiology 67: 547-560

163 Shinohara M, Zhu Y, Murakami F (2013) Four-dimensional analysis of nucleogenesis of the pontine nucleus in the hindbrain. Journal of Comparative Neurology 521: 3340-3357

164 Sillitoe R, Fu, Y, Watson, C. (2012) Chapter 11 - Cerebellum. In: Watson C, Paxinos G, Puelles, L (eds), *The Mouse Nervous System*, Elevier, Amsterdam, UK

165 Solecki DJ, Liu XL, Tomoda T, Fang Y, Hatten ME (2001) Activated Notch2 signaling inhibits differentiation of cerebellar granule neuron precursors by maintaining proliferation. Neuron 31: 557-568

166 Strick PL, Dum RP, Fiez JA (2009) Cerebellum and nonmotor function. Annu Rev Neurosci 32: 413-434

167 Sudhof TC (2012) The presynaptic active zone. Neuron 75: 11-25

168 Sudhof TC, Rizo J (2011) Synaptic Vesicle Exocytosis. Csh Perspect Biol 3: a005637

169 Sullivan PF, de Geus EJC, Willemsen G, James MR, Smit JH, Zandbelt T, Arolt V, Baune BT, Blackwood D, Cichon Set al (2009) Genome-wide association for major depressive disorder: a possible role for the presynaptic protein piccolo. Mol Psychiatr 14: 359-375

170 Terry-Lorenzo RT, Torres VI, Wagh D, Galaz J, Swanson SK, Florens L, Washburn MP, Waites CL, Gundelfinger ED, Reimer RJet al (2016) Trio, a Rho Family GEF, Interacts with the Presynaptic Active Zone Proteins Piccolo and Bassoon. PLoS One 11: e0167535

171 Thompson CL, Tehrani MHJ, Barnes EM, Stephenson FA (1998) Decreased expression of GABA(A) receptor alpha 6 and beta 3 subunits in stargazer mutant mice: a possible role for brain-derived neurotrophic factor in the regulation of cerebellar GABA(A) receptor expression? Mol Brain Res 60: 282-290

172 Tissir F, Goffinet AM (2003) Reelin and brain development. Nat Rev Neurosci 4: 496-505

173 tom Dieck S, Brandstatter JH (2006) Ribbon synapses of the retina. Cell Tissue Res 326: 339-346

174 Uhlen M, Fagerberg L, Hallstrom BM, Lindskog C, Oksvold P, Mardinoglu A, Sivertsson A, Kampf C, Sjostedt E, Asplund Aet al (2015) Proteomics. Tissue-based map of the human proteome. Science 347: 1260419

175 Umemori H, Linhoff MW, Ornitz DM, Sanes JR (2004) FGF22 and its close relatives are presynaptic organizing molecules in the mammalian brain. Cell 118: 257-270

176 van Dijk T, Baas F, Barth PG, Poll-The BT (2018) What's new in pontocerebellar hypoplasia? An update on genes and subtypes. Orphanet J Rare Dis 13: 92

177 Voogd J, Ruigrok TJH (2004) The organization of the corticonuclear and olivocerebellar climbing fiber projections to the rat cerebellar vermis: The congruence of projection zones and the zebrin pattern. Journal of Neurocytology 33: 5-21

178 Voogd JR, TJH (2012) Chapter 15 - Cerebellum and Precerebellar Nuclei. In: Mai, J and Paxinos, G (eds), *The Human Nervous System*, Elsevier, Amsterdam, Netherlands

179 Wagh D, Terry-Lorenzo R, Waites CL, Leal-Ortiz SA, Maas C, Reimer RJ, Garner CC (2015) Piccolo Directs Activity Dependent F-Actin Assembly from Presynaptic Active Zones via Daam1. PLoS One 10: e0120093

180 Wagh DA, Rasse TM, Asan E, Hofbauer A, Schwenkert I, Durrbeck H, Buchner S, Dabauvalle MC, Schmidt M, Qin Get al (2006) Bruchpilot, a protein with homology to ELKS/CAST, is required for structural integrity and function of synaptic active zones in Drosophila. Neuron 49: 833-844

181 Waites CL, Craig AM, Garner CC (2005) Mechanisms of vertebrate synaptogenesis. Annual Review of Neuroscience 28: 251-274

182 Waites CL, Leal-Ortiz SA, Andlauer TF, Sigrist SJ, Garner CC (2011) Piccolo regulates the dynamic assembly of presynaptic F-actin. J Neurosci 31: 14250-14263

183 Waites CL, Leal-Ortiz SA, Okerlund N, Dalke H, Fejtova A, Altrock WD, Gundelfinger ED, Garner CC (2013) Bassoon and Piccolo maintain synapse integrity by regulating protein ubiquitination and degradation. EMBO J 32: 954-969

184 Wang F, Xu Q, Wang W, Takano T, Nedergaard M (2012) Bergmann glia modulate cerebellar Purkinje cell bistability via Ca2+-dependent K+ uptake. Proc Natl Acad Sci U S A 109: 7911-7916

185 Wang VY, Rose MF, Zoghbi HY (2005) Math1 expression redefines the rhombic lip derivatives and reveals novel lineages within the brainstem and cerebellum. Neuron 48: 31-43

186 Wang XL, Kibschull M, Laue MM, Lichte B, Petrasch-Parwez E, Kilimann MW (1999) Aczonin, a 550-kD putative scaffolding protein of presynaptic active zones, shares homology regions with rim and bassoon and binds profilin. Journal of Cell Biology 147: 151-162

187 Watanabe D, Inokawa H, Hashimoto K, Suzuki N, Kano M, Shigemoto R, Hirano T, Toyama K, Kaneko S, Yokoi Met al (1998) Ablation of cerebellar Golgi cells disrupts synaptic integration involving GABA inhibition and NMDA receptor activation in motor coordination. Cell 95: 17-27

188 Watanabe M, Kano M (2011) Climbing fiber synapse elimination in cerebellar Purkinje cells. Eur J Neurosci 34: 1697-1710

189 Watanabe S (2015) Slow or fast? A tale of synaptic vesicle recycling. Science 350: 46-47

190 Watanabe S, Boucrot E (2017) Fast and ultrafast endocytosis. Curr Opin Cell Biol 47: 64-71

191 Watanabe S, Rost BR, Camacho-Perez M, Davis MW, Sohl-Kielczynski B, Rosenmund C, Jorgensen EM (2013) Ultrafast endocytosis at mouse hippocampal synapses. Nature 504: 242-247

192 Wechsler-Reya RJ, Scott MP (1999) Control of neuronal precursor proliferation in the cerebellum by sonic hedgehog. Neuron 22: 103-114

193 Wichmann C, Moser T (2015) Relating structure and function of inner hair cell ribbon synapses. Cell Tissue Res 361: 95-114

194 Wojcik SM, Brose N (2007) Regulation of membrane fusion in synaptic excitation-secretion coupling: Speed and accuracy matter. Neuron 55: 11-24

195 Xie RL, Manis PB (2017) Synaptic transmission at the endbulb of Held deteriorates during age-related hearing loss. J Physiol-London 595: 919-934

196 Xu HW, Yang Y, Tang XT, Zhao MN, Liang FC, Xu P, Hou BK, Xing Y, Bao XH, Fan XT (2013) Bergmann Glia Function in Granule Cell Migration During Cerebellum Development. Molecular Neurobiology 47: 833-844

197 Xu-Friedman MA, Regehr WG (2003) Ultrastructural contributions to desensitization at cerebellar mossy fiber to granule cell synapses. Journal of Neuroscience 23: 2182-2192

198 Zaqout S, Kaindl AM (2016) Golgi-Cox Staining Step by Step. Frontiers in Neuroanatomy 10:38

199 Zhai R, Olias G, Chung WJ, Lester RA, tom Dieck S, Langnaese K, Kreutz MR, Kindler S, Gundelfinger ED, Garner CC (2000) Temporal appearance of the presynaptic cytomatrix protein bassoon during synaptogenesis. Mol Cell Neurosci 15: 417-428

200 Zhai RG, Vardinon-Friedman H, Cases-Langhoff C, Becker B, Gundelfinger ED, Ziv NE, Garner CC (2001) Assembling the presynaptic active zone: a characterization of an active one precursor vesicle. Neuron 29: 131-143

201 Zhang W, Hong R, Xue L, Ou Y, Liu X, Zhao Z, Xiao W, Dong D, Dong L, Fu Met al (2017) Piccolo mediates EGFR signaling and acts as a prognostic biomarker in esophageal squamous cell carcinoma. Oncogene 36: 3890-3902

9. Abbreviations

Abp1 = Actin-binding protein 1

ACSF = artificial cerebrospinal fluid

AMP = adenosine monophosphate

AMPA = α-amino-3-hydroxy-5-methyl-4-isoxazolepropionic acid

ANOVA = analysis of variance

AP = action potential

Atg = autophagy-related protein

AZ = active zone

BCA = bicinchoninic acid assay

BDA = biotinylated dextran amine

BDNF = brain-derived neurotrophic factor

BMP4 = bone morphogenetic protein 4

BSA = bovine serum albumin

C2A/C2B = C-terminal C2 domain A/B

Ca^{2+} = Calcium

CamKII = Ca^{2+}/Calmodulin-dependent protein kinase II

CAST = Calpastatin

CAZ = cytoskeletal matrix assembled at active zones

CC = coiled-coil domain

CF = climbing fibre

CLAM = cerebellar atrophy with progressive microcephaly

CME = Clathrin-mediated endocytosis

CTb = cholera toxin b-subunit

CtBP = C-terminal binding protein

D-APV = µM D-(2R)-amino-5-phosphonovaleric acid

Daam1 = Disheveled-associated activator of morphogenesis 1

DAB = 3,3′-Diaminobenzidine

DAPI = 4′,6-diamidino-2-phenylindole

ddH2O = double distilled water

DIV = days in vitro

DNA = deoxyribonucleic acid

DSD = disorder of sexual development

Dvl = Dishevelled

EDTA = ethylenediaminetetraacetic acid

EGFR = epidermal growth factor receptor

EGL = external granule cell layer

ELKS2 = Glutamic acid (E), Leucine (L), Lysine (K) and Serine (S)

EM= electron microscopy

EPSC = excitatory postsynaptic current

EPSCs = excitatory postsynaptic currents

ERC = ELKS/RAB6-Interacting/CAST Family Member 2

EtOH = Ethanol

F-Actin = filamentous-actin

FGF = fibroblast growth factor

FGFR = FGF receptor

GABA = gamma aminobutyric acid

$GABA_AR$ = $GABA_A$ receptor

GC = granule cell

GSK3β = Glycogen synthase kinase 3β

GTP = Guanosine triphosphate

HPA = hypothalamic-pituitary-adrenal

HRP = horseradish peroxidase

ICC = immunocytochemistry

IGL = internal granule cell layer

IMP = inosine monophosphate

IP = intraperitoneal

JNK = c-Jun N-terminal kinase

KIND = Kinase non-catalytic c-lobe domain

KO = knockout

LOF = loss of function

mEPSC = mini EPSC

MF = mossy fibre

ML = molecular layer

MRI = magnetic resonance imaging

NA = numerical aperture

NBA = neurobasal medium

NGS = normal goat serum

Nlg3 = Neuroligin 3

NMDAR = N-methyl-D-aspartate receptor

Norm. = normalised

NSCs = neural stem cells

NT = neurotransmitter

ON = overnight

OptiMan = operator independent motor analysis

P = postnatal day

PB = phosphate buffer

PBH = Piccolo/Bassoon homology domain

PBS = phosphate buffered saline

PBST = PBS with 0.1 % Tween-20

PC = Purkinje cell

PCH = Pontocerebellar Hypoplasia

PCL = Purkinje cell layer

PCP = planar cell polarity pathway

PCR = polymerase chain reaction

PDZ = PDZ domain

PF = parallel fibre

PFA = paraformaldehyde

PKC = protein kinase C

PLL = poly-l-Lysine

PM = plasma membrane

PN = pontine neurone

PRA1 = prenylated Rab acceptor protein 1

PSD = postsynaptic density

PTV = Piccolo-Bassoon transport vesicle

PyC = pyramidal cell

RasGEF = Guanine nucleotide exchange factor for Ras-like small GTPases

RFID = radio-frequency identification

RIM = Rab3-interacting molecule

RIM-BP = RIM-binding proteins

RNA = ribonucleic acid

RNAseq = RNA sequencing

RRP = readily releasable pool

RT = room temperature

SDS-PAGE = sodium dodecyl sulfate–polyacrylamide gel electrophoresis

SEM = standard error of the mean

Shh = Sonic hedgehog

shRNA = short hairpin RNA

SM = Sec1/Munc18-like

SMA = spinal muscular dystrophy

SNARE = soluble NSF (N-ethylmaleimide-sensitive factor) attachment protein (SNAP) receptor

SNP = single nucleotide polymorphism

SO = *stratum oriens*

SP = *stratum pyramidale*

SR = *stratum radiatum*

STD = short term depression

SV = synaptic vesicle

TBST = tris-buffered saline

tRNA = transfer ribonucleic acid

TTX = tetrodotoxin

VGAT = vesicular inhibitory amino acid transporter

VGCC = voltage-gated calcium channels

VGluT1 = vesicular glutamate transporter 1

VGluT2 = vesicular glutamate transporter 2

WB = western blot

WM = white matter tract

Wnt = wingless-related integration site

WT = wildtype

ZF = zinc finger

10. Units

= number

% = percent

°C = degrees Celsius

a.u. = arbitrary units

cm = centimetres

g = grams

Hz = hertz

kDa = kiloDalton

kHz = kiloHertz

m = metre

mg = milligram

min = minutes

ml = millilitre

mM = millimolar

mm = millimetre

mOsm = milliosmole

ms = millisecond

mV = millivolt

mΩ = megaohm

nm = nanometre

pA = picoamp

pF = picofarad

R_{in} = input resistance

rpm = revolutions per minute

s = seconds

V = volts

µl = microlitre

μm = micrometre

μs = microsecond

T_w = weighted time constant

11. Contributions

- **Figure 10:** *Pclo*$^{gt/gt}$ rats were created by F. K. Hamra at the University of Texas, USA. Christine Bruns, Deutsches Zentrum für Neurodegenerative Erkrankungen (DZNE), performed western blot analysis.

- **Figure 12:** Immunoperoxidase and Nissl staining followed by cortical and pontine measurements were performed by Christine Bruns, DZNE.

- **Figure 24:** Electron microscopy and analysis of images was performed by Dr. Marta Orlando at the Charité Medical University, Berlin.

- **Figure 26:** Electrophysiology and analysis was performed by Isabelle Straub, Carl-Ludwig Institute for Physiology, Leipzig.

- **Figure 27:** Behavioural experiments (Figure 27 A-D) were performed by Erik Plautz at the University of Texas, USA; experiment in the OptiMan setup (Figure 27 E-F) were performed by Humaira Munawar, Humboldt University of Berlin, Berlin.

12. Publications

Falck, J., Bruns., C., Hoffmann-Conaway, S., Straub, I., Plautz, E., Orlando, M., Munawar, H., Rivalan, M., Winter, Y., Izsvák, Z., Schmitz, D., Hallermann, S., Garner, C.C., Ackermann, F. (in press). Loss of Piccolo function in rats induces cerebellar network dysfunction and Pontocerebellar Hypoplasia type 3-like phenotypes. The Journal of Neuroscience.

13. Acknowledgments

First and foremost, I would like to thank Craig for inviting me to join his lab, and for his supervision and encouragement throughout my studies. With his help, I have had the freedom to learn and have been encouraged to grow as a scientist, more than I could have imagined. I have been incredibly lucky to have such great role model and genuinely kind person to have guided me through this process.

I am truly grateful to Professor Robin Hiesinger for taking the time to read this thesis.

I would like to thank the members of the Garner lab for welcoming me into their team and for their endless help in the scientific and bureaucratic endeavours that come with moving to a new country and with trying to master new techniques.

I would like to give special thanks to Frauke, for her guidance and support, without which I certainly would not have made it this far. I am also grateful to Sheila for all of her help with writing the manuscript, with perfecting this thesis, and to Christine who helped me to tackle new techniques and worked alongside me on the Piccolo project. I would also like to thank Ewa from the bottom of my heart for her support and friendship during my time both in and out of the lab.

I am truly grateful to the people whom I have been lucky enough to collaborate with: Marta, Isabelle, Erik, Humaira, Kent and Stephan, without whom this story would not be complete.

I must give my gratitude to Professor Alex Thomson, for taking a chance on me and offering me my first scientific position, I would not have been able to take on this incredible endeavour without her confidence in me.

Finally, I would like to thank my wonderful family and incredible friends for their support and love, for encouraging me to keep going when it's been tough and for being a joyful distraction when needed. I would like to dedicate this thesis to my wonderful grandmothers, Alice and Rose, for being such inspirational women and for their love and support.